Faculdade de Engenharia
Instituto de Ciências Biomédicas Abel Salazar
Universidade do Porto

Modified-chitosan based nanoparticles for the delivery of Rac1 siRNA in neuronal ischemia

Sara Soares de Sousa

Master Thesis
Integrated Masters in Bioengineering
Branch of Molecular Biotechnology

Supervisor: Dr. Sofia Duque Santos
Co-supervisor: Dr. Ana Paula Pêgo

October 2016

Abstract

Stroke or a cerebrovascular accident leading to brain ischemia is one of the main causes of mortality and disability worldwide with currently only one approved treatment, tissue plasminogen activator (tPA), applied solely to a small percentage of stroke patients. Although this treatment is effective in opening the occluded cerebral vessels, there is no approved treatment to antagonize the injurious processes that occur and persist in the brain after ischemia. Thus, neuroprotective agents have generated much interest. Interfering with Rac1 Rho GTPase expression/activation in ischemic models has showed to restrict cell death. Such observations raised the hypothesis that Rac1 downregulation could be studied for neuroprotection.

Small interfering RNA (siRNA) sequences have been widely investigated as gene therapeutics owing to their potential to silence a gene of interest, being therefore an appropriate strategy to evaluate the function of Rac1 after an ischemic insult. Nevertheless, a suitable carrier is needed to transport and protect siRNA sequences enabling their efficient cellular delivery. Chitosan is a cationic polymer broadly used for siRNA delivery. This polymer is known for its biodegradability, biocompatibility and reduced toxicity. Additionally, chitosan mucoadhesive and mucosa permeation abilities are key features appropriate for intranasal administrations in order to reach the brain. The use of trimethyl chitosan (TMC), a chitosan derivative with improved solubility at physiological pH, constitutes an advantage for particles stability, namely in physiological conditions, which is highly desirable for the development of translational therapies.

The aim of the present work was to study TMC particles performance and to evaluate the therapeutic potential of Rac1 loss of function in a neurotoxic context. For that, TMC nanoparticles were characterized and used for Rac1 siRNA delivery to neurons *in vitro*. Furthermore, nanoparticles ability to reach the mice brain through nasal administration was also investigated.

TMC particles revealed sizes below 200 nm for the higher amine-to-phosphate (N/P) ratios tested (ratios 4, 8 and 12). These nanoparticles showed a narrow size distribution with low polydispersity index (PDI) values (<0.3), a positive, although low, zeta potential (8-10mV), a high stability and the capability to efficiently protect Rac1 siRNA from RNase degradation. Additionally, these complexes did not show cellular toxicity. TMC nanoparticles were found intracellularly for the N/P ratios 4 and 8. Nevertheless, the complexes did not lead to a decreased

gene expression, contrary to what was verified for the transfection agent lipofectamine. Transfection of Rac1 siRNA with lipofectamine was able to rescue the cell death phenotype elicited by the addition of a cytotoxic stimulus, which highlights the potential of Rac1 downregulation for neuroprotection.

The transport of nanoparticles to the brain through the intranasal route was evaluated, and presence of complexes in the olfactory bulbs (OB), cortex and meninges was shown, although only in a limited amount. PEGylation of TMC was used, which improved the transport to brain. Nevertheless, the amount of particles reaching the brain tissue was still not acceptable for our strategy of siRNA delivery.

Taken together, the results obtained here suggest TMC as a prospective candidate for efficient siRNA delivery in neuronal cells as well as *in vivo* transport from nose to brain, although different features should be optimized in order to achieve the desired goals. Additionally, Rac1 downregulation as a potential therapeutic target for neuroprotection, in oxidative stress conditions characteristic of brain ischemia, was highlighted.

Acknowledgements

A todos os que possibilitaram a realização deste trabalho, um imenso obrigada.

À Sofia Santos, por todo o apoio e orientação ao longo deste projeto. Pelos ensinamentos e pelas sugestões construtivas. Pelas discussões que foram determinantes não só para a concretização do projeto como para a minha evolução. Ainda, um obrigado especial pela colaboração em toda a parte experimental com animais, que teria sido impossível sem a sua ajuda. Finalmente, queria mostrar o meu agradecimento pelo sorriso e espirito positivo diários que me motivaram sempre

À professora Ana Paula Pêgo por me ter dado a oportunidade de trabalhar neste grupo, no qual tanto cresci, quer pessoal quer profissionalmente.

A todos os elementos da equipa nBTT, pela simpatia com que me receberam e por se terem sempre prontificado a ajudar-me quando solicitei. Foi um privilégio ter trabalhado num ambiente como o que vocês me proporcionaram. Um obrigado especial à Carla Gomes por me ter fornecido os polímeros que usei ao longo do projeto.

À Joana Silva, à Joana Loureiro, à Rita Pereira, à Eva Carvalho, as minhas companheiras de mestrado. Ter-vos comigo tornou todas as longas horas passadas no laboratório muito mais leves. Obrigada pelas conversas, pelas gargalhadas, pelo apoio. Tive uma sorte enorme por vos ter tido como colegas de laboratório.

À Joana, à Ana, à Mariana, à Filipa, à Paula, à Isabel e à Raquel, as minhas amigas de sempre. Obrigada pelas vossas palavras sempre sábias e por me continuarem a mostrar que com amigos tudo se torna mais fácil. O vosso apoio foi, sem dúvida, muito importante.

À minha família, por me acarinharem e fazerem sentir especial em cada etapa.

Ao Zé, por me teres acompanhado como ninguém durante este percurso. Pelo apoio, a paciência, o companheirismo. Por acreditares em mim e me transmitires todas as forças do mundo.

Ao meu irmão, por me teres motivado a persistir e a nunca deixar de procurar o que me faz feliz.

Aos meus pais, pelo apoio incondicional, por acreditarem sempre em mim e me incentivarem a dar o meu melhor. Por me ampararem a cada queda e celebrarem com um orgulho enorme cada vitória minha.

The research described in this thesis was financed by:

- Project "BaiTS - Biodegradable dendrimers for Targeted neuroprotective therapies in Stroke", Ref. PTDC/CTM-NAN/3547/2014, FEDER through Programa Operacional Competitividade e Internacionalização - COMPETE 2020 and FCT - Fundação para a Ciência e a Tecnologia in the framework of the project POCI-01-0145-FEDER-016639

- Project "nanoTerapias Neuroprotetoras avançadas para o tratamento de acidentes vasculares cerebrais" (nº FIS-FIS-2015-01_CCV_20150630-88), through Fundo para a Investigação em Saúde (INFARMED).

- Project NORTE-01-0145-FEDER-000008 , supported by Norte Portugal Regional Operational Programme (NORTE 2020), under the PORTUGAL 2020 Partnership Agreement, through the European Regional Development Fund (ERDF)

- Fundo Europeu de Desenvolvimento Regional funds through the COMPETE 2020 - Operacional Programme for Competitiveness and Internationalisation (POCI), Portugal 2020, and by Portuguese funds through FCT - Fundação para a Ciência e a Tecnologia/ Ministério da Ciência, Tecnologia e Ensino Superior in the framework of the project "Institute for Research and Innovation in Health Sciences" (POCI-01-0145-FEDER-007274)

Table of Contents

Abstract ... i
Acknowledgements ... iii
Table of Contents ... vi
List of Figures ... ix
List of tables ... xv
List of Abbreviations ... xvi
Chapter 1 ... 1
Introduction ... 1
1.1. Brain Ischemia and Rho GTPases ... 1
1.1.1. Brain ischemia ... 1
1.1.1.1. Neuroprotection ... 3
1.1.2. Mammalian Rho GTPases ... 3
1.1.2.1. Rho GTPases in the nervous system ... 5
1.1.2.1.1. Neuronal development ... 5
1.1.2.1.2. Synapse plasticity ... 5
1.1.2.1.3. Neuronal survival ... 6
1.1.3. Rho GTPases in brain ischemia ... 6
1.1.3.1. The role of Rac1 GTPase in brain ischemia ... 8
1.2. Use of RNAi as a therapeutic strategy ... 11
1.3. Chitosan-based nanoparticles for the delivery of siRNA ... 13
1.3.1. Chitosan potential and important considerations for siRNA delivery systems ... 13
1.3.2. Intranasal route for successful non-viral nucleic acids delivery to the brain ... 16
Chapter 2 ... 20
Aim of the Project ... 20
Chapter 3 ... 22
Experimental Methods ... 22
3.1. HT22 cell culture ... 22
3.1.1. HT22 cell cytotoxic treatment ... 22
3.2. Cell viability assays ... 22
3.2.1. Resazurin assay ... 23
3.2.2. MTT assay ... 23
3.2.3. Propidium iodide and Hoechst 33342 staining ... 24

3.2.4. Calcein and Propidium Iodide staining ... 24

3.3. Rac1 immunofluorescent staining ... 24

3.4. F-actin fluorescent staining ... 25

3.5. Protein extraction and western blot ... 25

3.6. TMC-siDNA/siRNA polyplexes synthesis and characterization ... 26

3.6.1. Synthesis ... 28

3.6.2. Dynamic and Electrophoretic Light Scattering ... 29

3.6.3. Gel Retardation Assay ... 30

3.6.4. RNAse protection assay ... 30

3.7. Transfections ... 31

3.8. Polyplexes association and internalization analysis ... 31

3.8.1. Flow cytometry studies ... 32

3.8.2. Imaging studies ... 32

3.9. RNA extraction and Real Time quantitative Reverse Transcriptase-Polymerase Chain Reaction ... 32

3.10. In vivo studies ... 33

3.10.1. Nanoparticles preparation ... 34

3.10.2. Nanoparticles administration ... 35

3.10.3. Tissue processing and analysis ... 36

3.10.4. Tissue homogenates ... 36

3.11. Statistical Analysis ... 37

Chapter 4 ... 38

Results and Discussion ... 38

4.1. Rac1 expression in the HT22 cell line in a neurotoxic context ... 38

4.1.1. HT22 response to a neurotoxic stimulus ... 38

4.1.2. HT22 Rac1 expression after a neurotoxic stimulus ... 40

4.2. TMC polyplexes characterization ... 44

4.2.1. TMC-siDNA complexes ... 44

4.2.1.1. Size, polydispersity index and zeta potential ... 44

4.2.1.2. Stability ... 47

4.2.2. TMC-siRNA complexes ... 48

4.2.2.1. Size, polydispersity index and zeta potential ... 48

4.2.2.2. Stability and protection from RNase degradation ... 49

4.3. TMC polyplexes *in vitro* cell association and internalization ... 51

4.3.1. TMC-siDNA complexes ... 51

4.3.2. TMC-siRNA complexes 55
4.4. TMC polyplexes *in vitro* cell cytotoxicity 58
4.5. Rac1 knockdown in HT22 cell line 60
4.5.1. Rac1 expression following transfection 60
4.5.2. Rac1 knockdown effect in a neurotoxic context 62
4.6. TMC polyplexes *in vivo* administration 65
Chapter 5 74
Concluding Remarks and Future Perspectives 74
References 76
Supplementary information 82

List of Figures

Figure 1 Overview of the pathological processes involved in ischemic injury. Ischemic core and penumbra are represented as well as the main events occurring in the ischemic cascade and how they evolve over time. Adapted from [5]. 2

Figure 2 Schematic representation of the Rho GTPases regulation. GEFs mediate Rho GTPases activation through GDP exchange for GTP while GAPs have the opposing function. GDIs maintain Rho GTPases in the cytoplasm in an inactive state. Adapted from [17]. 4

Figure 3 Overview of the different pathways through which Rac1 may contribute the neuronal death after neuronal ischemia. (A) Rac1 is needed for Nox assembly and activation, which increases ROS production and therefore contributes to ischemic-induced oxidative stress that worsens ischemic injury. (B) POSH-Rac1-MLK3 complex activates the pro-apoptotic JNK signalling. (C) Rac1 promotes dendritic spine growth increasing neuronal vulnerability to ischemia. 10

Figure 4 Cellular mechanism of RNAi mediated by siRNA. After transfection, siRNA is incorporated into RISC, which maintains one RNA strand (antisense or guide strand). The siRNA guide included in the active RISC (RISC*) recognizes the target sequence, which is then degraded by Ago2. Intracellular ribonucleases further degrade the mRNA fragments due to the lack of a 50-cap and a poly(A) tail. Adapted and modified from [73]. 12

Figure 5 Intracelullar barriers for nanoparticle-mediated siRNA delivery. After cell internalization, nanoparticles must escape endosomal degradation and dissociate its cargo on the cellular cytoplasm, where it can be incorporated in the RISC and exert its silencing function. ECM= extracellular matrix. Adapted and modified from [73] 14

Figure 6 Chitosan and TMC chemical structures. (A) Subunit of chitosan displaying β-(1-4)-linked D-glucosamine (deacetylated unit) and N-acetyl-D-glucosamine (for R=$COCH_3$, acetylated unit). (B) Modified glucosamine-units of trimethylated chitosan. Adapted from [77]. 15

Figure 7 Schematic representation of brain-to-nose pathways and approximate average distances from the olfactory and respiratory epithelium to CNS targets. Adapted and modified from [91]. 16

Figure 8 Particles transport across the olfactory epithelium to the brain. Axonal processes of OSNs converge into bundles (fila olfactoria), surrounded by ensheathing cells and fibroblasts, that are projected to the OB. Potential pathways for particles delivery following intranasal administration are represented in red. Some substances may be transported by an intracellular pathway, while others may cross the olfactory epithelial barrier by paracellular or transcellular transport, reaching the lamina propria, where different extracellular pathways for distribution are possible: 1) absorption into olfactory blood vessels; 2) absorption into olfactory lymphatic vessels; 3) extracellular diffusion within extracellular spaces surrounding nerve bundles. Conceivable pathways for distribution of substances from the perineural space into the OB or into the CSF are shown. Adapted and modified from [91]. 17

Figure 9 Polyplexes synthesis. (A) Schematic representation of the complexes formation. (B) Scheme of the experimental procedure to synthetize the polyplexes: I) TMC and sequences are heated; II) sequences are added to the TMC solution under vortex; III) the resulting mix is agitated; IV) mixes are, ultimately, incubated at RT. 29

Figure 10 Scheme of the different experimental steps to assess polyplexes capacity to protect RNA sequences from RNase degradation. Complexes and free siRNA were incubated with RNase for different time periods, after which the enzyme was inactivated with EDTA. Both free siRNA sequences and complexes were then treated with SDS, which allowed sequences dissociation from the complex, and samples were loaded onto a polyacrylamide gel. 31

Figure 11 *In vivo* studies. (A) Scheme of the nanoparticles synthesis process for *in vivo* administration. Particles were synthetized in normal and “high concentration” conditions and concentrated through ultracentrifugation or lyophilisation. (B) Schematic representation of the animal experimental procedures. Nanoparticles were intranasally administered to anesthetized mice and antagonist was administered. 4h after mice were sacrificed and organs were collected for histological analysis. 34

Figure 12 Effect of glutamate toxicity on HT22 cells. (A) Cell viability, through resazurin assay, following exposure to different glutamate concentrations for 6 and 24h. Results are normalized to the viability of control (non-treated) cells. (n=2 for 6h and n=3 for 24h) ***p<0.001, relative to control (B) Phase contrast images of cells after 24h treatment with different glutamate concentrations. Control=untreated cells. Scale bar is 60μm. 39

Figure 13 HT22 cells viability, through MTT assay, following a 4h neurotoxic stimulus. (A) Cells treated with different glutamate concentrations (n=4). (B) Cells treated with different H2O2 concentrations (n=4). Results are normalized to the cell viability of the control (non-treated) cells. *p<0.05 **p<0.01 ***p<0.001 (relative to the control). 40

Figure 14 Rac1 expression in HT22 cells after 4h treatment with different concentrations of glutamate or H_2O_2. (A) Fold increase in Rac1 expression levels, relative to control untreated cells, after treatment with glutamate (normalized to β-actin). Representative bands from 3 independent experiments (n=3) *p<0.05, relative to control. (B) Fold increase in Rac1 expression levels, relative to control untreated cells, after treatment with H_2O_2 (normalized to β-actin). Representative bands from 3 independent experiments (n=3). *p<0.05, relative to control. (C) Rac1 immunostaining following glutamate treatment. (D) Rac1 immunostaining following H_2O_2 treatment. Control= untreated cells. Rac1 represented in green. Nuclei counterstained with DAPI (blue). White arrows denote Rac1 accumulations. Scale bar is 20µm. 41

Figure 15 Rac1 expression in differentiated HT22 cells 4h after treatment with different concentrations of glutamate. Control= untreated cells. Rac1 represented in green. Nuclei counterstained with DAPI (blue). White arrows denote cytoplasmic Rac1 accumulations. Yellow arrows point nuclear Rac1 accumulations. Scale bar is 20µm. 43

Figure 16 Size and PDI of TMC-siDNA polyplexes. (A) TMC-siDNA complexes size as a function of N/P ratio before and after lyophilisation (n=4 before lyophilisation, n=2 after lyophilisation). (B) TMC-siDNA complexes PDI as a function of N/P ratio before and after lyophilisation (n=4 before lyophilisation, n=2 after lyophilisation). (C) TMC-siDNA “high concentration” complexes size for N/P 4 and 8 before and after lyophilisation (n=2). (D) TMC-siDNA “high concentration” PDI for N/P 4 and 8 before and after lyophilisation (n=2). (E) TMC-PEG-siDNA complexes size for N/P 4 and 8 with 25 and 75% of thiol groups modified with PEG (n=2). (F) TMC-PEG-siDNA complexes size for N/P 4 and 8 with 25 and 75% of thiol groups modified with PEG (n=2). * p<0.05, unpaired t-test was employed. 46

Figure 17 siDNA gel retardation assay. (A) TMC-siDNA complexes at different N/P ratios at 0d and 1d after complexation. Black arrow indicates a smear band showing the existence of delayed siDNA release. (B) TMC-siDNA “high concentration” complexes, 1d after complexation. L=ladder; TMC: TMC was loaded in an amount equal to N/P 8 formulation. 48

Figure 18 Size and PDI of TMC-siRNA polyplexes (n=3). 49

Figure 19 siRNA gel retardation assay with complexes formed at different N/P ratios, 0 and 1d after complexation. Black arrows indicate a smear band showing the existence of delayed siDNA release. Yellow arrow indicates the existence of siRNA sequences in the well. L=ladder; TMC: TMC was loaded in an equal amount to N/P 8 formulation. 50

Figure 20 RNase protection assay. Gel retardation was performed for free siRNA and for TMC-siRNA complexes prepared at N/P 8, after incubation with RNase A for different time periods. Relative quantity of siRNA is compared to the 0h incubation, for polyplexes + RNase condition. L=ladder.. 50

Figure 21 Association of TMC-siDNA complexes to HT22 cells 24h after incubation with 100 and 200nM siDNA$_{cy5}$. (A) Histograms of cy5 fluorescence intensities. Cells with no treatment (control), treated with only TMC (TMC) and/or treated with N/P 4 TMC complexes with unlabelled sequences (N/P 4 unlabelled siDNA) were used as control. RFU=relative fluorescence units. Lipo= lipofectamine. (B) Fluorescence microscopy images of TMC-siDNA$_{cy5}$ polyplexes interaction with cells. Nuclei is stained in blue (DAPI) and siDNAcy5 represented in red. Scale bar is 20µm. 53

Figure 22 Confocal microscopy images of HT22 cells, 24h after transfection with TMC-siDNA$_{cy5}$ (N/P 4 and 8, 200nM siDNA$_{xy5}$). Rectangular highlighted areas are shown at a higher magnification. Nuclei is stained in blue (DAPI) and siDNA$_{cy5}$ represented in red. 54

Figure 23 TMC$_{ROX}$-siDNA (N/P 8) cellular uptake after incubation for 4 and 24h (200nM siDNA). Left picture was taken on a fluorescence microscope and picture on the right was taken on a confocal microscope. Cells cytoskeleton is coloured in green with phalloidin to help on the visualization of nanoparticles interaction with cells. Nuclei is stained in blue with Hoechst. TMC$_{ROX}$ is represented in red. White arrows indicate TMC$_{ROX}$ colocalization with the nucleus and perinuclear regions. 55

Figure 24 Association of TMC-siRNA complexes to HT22 cells 24h after incubation with 200nM siRNA$_{FAM}$. (A) Percentage of complexes cellular association (n=3). *p<0.05 **p<0.01 (B) Hystograms of FAM fluorescence intensities. Cells with no treatment were used as control. RFU=relative fluorescence units (C) Fluorescence microscopy images of TMC-siRNA$_{FAM}$ polyplexes interaction with cells. Nuclei is stained in blue (Hoechst) and siRNA$_{FAM}$ represented in green. Scale bar is 20µm. Lipo= lipofectamine. 56

Figure 25 TMC$_{ROX}$-siRNA (N/P 4 and 8) cellular uptake 24h after incubation with 200nM Rac1 siRNA. Cells cytoskeleton is coloured in green with phalloidin. Nuclei is stained in blue with

Hoechst. TMC_{ROX} is represented in red. White arrows indicate complexes colocalization with the nucleus. Yellow arrow highlight complexes accumulations.. 57

Figure 26 Cytotoxicity of TMC-siDNA complexes (A) Cell viability was measured through resazurin assay. Cells were incubated with TMC-$siDNA_{cy5}$ (at different N/P ratios) or lipofectamine for 24h (200nM siDNA concentration). Results are normalized to the cell viability of control (non-treated) cells (n=3). (B) Calcein/Propidium iodide staining. Representative fluorescence microscopy images of HT22 cells, 24h following incubation with TMC-$siDNA_{cy5}$ complexes or Lipofectamine (200nM $siDNA_{cy5}$). Calcein is represented in green. PI stained nuclei are in red. Cy5 is represented in cyan. White arrows highlight nuclei stained with PI. TMC: cells were incubated with an amount equal to N/P 8 formulation. Scale bar is 40µm. 59

Figure 27 Rac1 mRNA expression on cells transfected with Rac1 or negative control siRNAs, 24h post-transfection (200nM siRNA). Transfection performed with TMC polyplexes (N/P 4 and N/P 8) and with lipofectamine (lipo). The values of Rac1 expression were quantified with real-time PCR and normalized to the housekeeping gene, cyclophilin (n=3). *p<0.05, ns=non-significant. 61

Figure 28 PI and Hoechst staining of cells transfected with Rac1 or negative control siRNAs (200nM), following treatment with H_2O_2. Non-treated cells used as control (-H_2O_2). (A) Representative images of the different conditions. (B) PI fluorescence intensity quantification. Values are normalized to Hoechst fluorescence intensity. Data from single experiment. 6 pictures taken with the 20x objective were analysed per condition. * p<0.05, unpaired t-test was employed. A.U.=arbitrary units. Scale bar is 100µm... 63

Figure 29 Fluorescence microscopy images of different brain regions (OB, cortex and meninges) and kidney, 4h after TMC_{ROX} complexes administration. Particles localization is highlighted (white arrows) Nuclei in blue (DAPI). TMC_{ROX} in red. OB= olfactory bulbs; FD=freeze-drying; UF=ultrafiltration; GL=glomerular layer; EPL=external plexiform layer; MCL=mitral cell layer. Scale bar for OB, Cortex and Meninges is 40µm. Scale bar for Kidney is 150µm. 66

Figure 30 Fluorescence microscopy images of mice organs 4h after TMC-PEG-$siDNA_{cy5}$ complexes intranasal administration, with two different percentages of TMC_{SH} PEGylation. (A) Different regions of the brain (OB, cortex and meninges) were analysed. White arrows highlight particles localization (B) Nasal mucosa, trachea, esophagus and kindey were also evaluated. Nuclei in blue (DAPI). $siDNA_{cy5}$ is represented in red. OB= olfactory bulbs; ONL=olfactory nerve layer;

GL=glomerular layer. Scale bar for OB, cortex and meninges is 40µm. Scale bar for nostrils, trachea and kidney is 150µm. Scaler bar for esophagus is 300µm. 69

Figure 31 Fluorescence microscopy images of mice organs 4h after fluospheres simultaneous intranasal and intravenous administration. (A) Different regions of the brain (OB, cortex and meninges) were analysed. OB= olfactory bulbs (B) Particles linear track in the brain cortex. White surrounding line highlights the path followed by fluospheres. (C) Kidney accumulation of fluospheres. Nuclei in blue (DAPI). Fluospheres are represented in red. 71

Figure 32 Fluospheres distribution in different tissues 1 and 4h after intranasal administration (0.2mg). OB= olfactory bulbs 72

Figure S 1 siDNA sense (S) and anti-sense (AS) sequences were annealed at different AS/S molar ratios. DNA was stained with SYBRGold and gel visualized in in a GelDoc XR imaging system. Results showed the conditions in which there are no free sequences and thus, that allows for a maximized annealing efficiency. 82

Figure S 2 Representative experion analysis of RNA samples from transfected cells showing high RNA recovery levels and good integrity indexes for all the samples. 18S and 28S rRNAs are indicated. RQI = RNA quality indicator, algorithm that allows the standardization and quantification of RNA integrity with 10 meaning fully intact RNA and 1 meaning fully degraded RNA. NT= non-transfected. 83

Figure S 3 Phase contrast images of differentiated HT22 cells after four days of culture, with or without culture medium change. 84

Figure S 4 siRNA electrophoresis. Brackets indicating sequences degradation. bp=base pairs . 84

Figure S 5 Fluorescence microscopy image of the nasal mucosa of mice 4h after TMC_{ROX} complexes intranasal administration. Nuclei in blue (DAPI). TMC_{ROX} in red. 85

List of tables

Table 1 Zeta Potential of TMC-siDNA polyplexes (n=2). 47

Table 2 Zeta Potential of TMC-siRNA polyplexes (n=3). 49

Table 3 Percentage of cells with cy5 fluorescence, 24h after incubation with TMC or lipofectamine complexes (n=1 for 100nM, n=2 for 200nM). 52

Table S 1 Sequences of siDNA and Rac1 siRNA. 82

Table S 2 Primer sequences used in qPCR. T_m=melting temperature. bp=base pairs 83

List of Abbreviations

Ago2: Argonaut 2
ASOs: Antisense oligonucleotides
BBB: Brain blood barrier
CBR: Cibacron Brilliant Red
Cdc42: Cell division control protein 42 homolog
CGN: Cerebellar granule neurons
CSF: Cerebrospinal fluid
CT: Comparative treshold
Cy5: Cyanine 5
DA: Degree of acetylation
DD: Degree of deacetylation
DLS: Dynamic Light Scattering
DQ: Degree of quaternization
ECM: Extracellular matrix
EPL: External plexiform layer
FAM: 5'-Carboxyfluorescein
FD: Freeze-drying
GAPs: GTPase activating proteins
GDIs: Guanine nucleotide dissociation inhibitors
GEFs: Guanine nucleotide exchange factors
GL: Glomerular layer
GPC: Gel permeation chromatography
G proteins: Guanine nucleotide-binding proteins
HIF: hypoxia inducible factor
IGF-1: Insulin-like growth factor-1
i.p.: Intraperitoneal
I/R: Ischemia/reperfusion
JNK: c-Jun N-terminal kinase
LTP: Long-term potentiation
MAPK: Mitogen-activated protein kinase
MCA: Middle cerebral artery
MCAO: Middle cerebral artery occlusion
MCL: Mitral cell layer
MLK3: Mixed-lineage protein kinase 3
MMPs: Matrix metalloproteinases
MTT: 3-(4,5-dimethyl-2-thiazolyl)-2,5 diphenyl tetrazolium bromide
NLS: Nuclear localization signal
NMDA: N-methyl-D-aspartate
NMR: Nuclear magnetic ressonance
Nox: NADPH oxidase
N/P: Amine-to-phosphate ratio
OB: Olfactory bulbs
OCT: Optimum cutting temperature
OGD: Oxygen-glucose deprivation
ONL: Olfactory nerve layer
OSNs: Olfactory sensory neurons
PCR: Polymerase Chain Reaction
PDI: Polydispersity Index
PDL: Poly-D-lysine
pDNA: plasmid DNA
PEG: Polyethylene glycol
PEI: Poly(ethylene imine)
PI: Propidium iodide
PIDs: Peri-infarct depolarizations
PI3K: phosphoinositide 3-kinase
POSH: Plenty of SH3s
qPCR: Quantitative Polymerase Chain Reaction
Rac1: Ras-related C3 botulinum toxin substrate 1
RhoA: Ras homolog gene family, member A
RhoB: Ras homolog gene family, member B
RISCs: RNA induced silencing complexes
RNAi: RNA interference
ROCK: Rho-associated protein kinase
ROS: Reactive oxygen species
ROX: 6-Carboxy-X-rhodamine N-succinimidyl ester
shNRA: Small hairpin RNA
siDNA: “Small interfering” DNA
siRNA: Small interfering RNA
TMC: Trimethyl chitosan
tPA: Tissue plasminogen activator
UF: Ultrafiltration

Chapter 1

Introduction

1.1. Brain Ischemia and Rho GTPases

1.1.1. Brain ischemia

Brain ischemia is the more prevalent type of stroke, a neurological condition that constitutes one of the leading causes of death and disability worldwide [1-5]. This pathology occurs after a reduction in blood flow, caused by occlusion of one or more cerebral blood vessels, to a level that is enough to compromise normal cellular function and that induces neurological deficits that persist beyond 24h or are interrupted by death [4,6,7]. Stroke can be either ischemic or hemorrhagic with ischemic stroke accounting for approximately 87% of all stroke cases [8]. Ischemic stroke can involve permanent or transient occlusion of the cerebral arteries, with the latter having reperfusion due to treatment with tPA or to natural reperfusion [2]. Brain tissue is highly sensitive to ischemia [6] and, specifically neurons, have a very high metabolic demand [9] which makes them even more vulnerable to ischemic conditions. Furthermore, the pattern of pathological damage varies depending on the degree and duration of the impaired blood flow and on the infarction site [3-5].

Blood supply interruption, in ischemia, leads to oxygen-glucose deprivation (OGD), which elicits multiple processes that culminate on cell death, such as excitotoxicity and ionic imbalance, peri-infarct depolarizations (PIDs), oxidative stress and inflammation (Figure 1) [1,5].

Impaired energy prevents neurons maintenance of the transmembrane ion gradients causing neurons membrane depolarization and increase of the intracellular calcium (Ca^{2+}) levels [2,5,6]. Increased intracellular Ca^{2+} levels activate many Ca^{2+} dependent proteases, lipases and DNAses [9], which ultimately elicit cell death. Furthermore, membrane depolarization leads to excessive neurotransmitter release, and specifically to the increased release of glutamate. Outside the cells, glutamate will activate N-methyl-D-aspartate (NMDA) receptors and other glutamate receptors, which further increases the Ca^{2+} influx leading to excitotoxicity [1].

PIDs are spontaneous waves of depolarization that occur in the penumbra (area that surrounds the ischemic core of the infarct) following focal stroke and are associated with increased ischemic injury. These depolarizations may be caused by the release of potassium and excitatory amino acids from the ischemic core (area most severely affected by the blood flow reduction) [1,7].

Oxidative stress is induced mainly during reperfusion, in which pro-oxidant enzymes and mitochondria utilize the oxygen as a substrate and produce an excessive amount of reactive oxygen species (ROS). ROS directly damage cells causing secondary mitochondrial dysfunction, lipid peroxidation, matrix metalloproteinases (MMPs) activation and DNA oxidation. [6,10]. Nevertheless, this phenomenon is also verified upon oxygen depletion in the brain cells, previous to reperfusion [11].

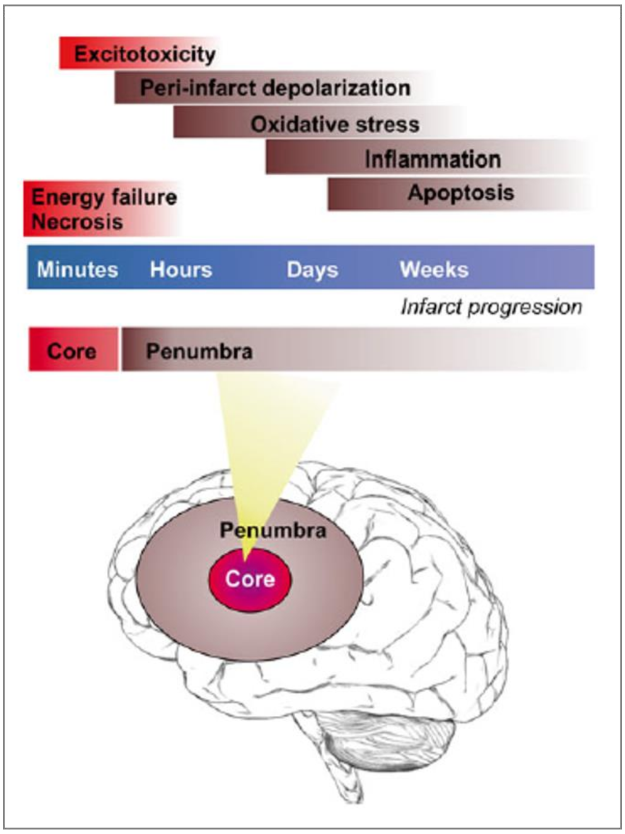

Figure 1 Overview of the pathological processes involved in ischemic injury. Ischemic core and penumbra are represented as well as the main events occurring in the ischemic cascade and how they evolve over time. Adapted from [5].

Inflammation has a crucial role on stroke related brain damage. After stroke, leucocytes are recruited to the injury site and activated, exacerbating the local tissue injury by release of pro-inflammatory cytokines, proteases and ROS [1]. These molecules also alter blood brain barrier (BBB) permeability, leading to brain edema [7]. Particularly MMPs that are secreted by, for example, leucocytes are important mediators of ischemic stroke pathology contributing to the breakdown of BBB [4]. Microglia is also activated after ischemic stroke worsening the inflammatory phenomena [6]. Nonetheless, inflammatory cells have also been reported to have beneficial effects on later stages of ischemic stroke [1,7].

Cell death after ischemia occurs by apoptosis and necrosis [1,5]. Apoptosis is a major mediator of brain injury in the penumbra. The penumbra is a non-functional hypoperfused area that still shows some structural integrity having only a mild injury and preserving ATP [1,7,12]. Necrosis, usually called pannecrosis, occurs on the ischemic core [1,5,7]. In the core of ischemia, neuronal death occurs within minutes as a result of energy depletion. However, in the penumbra, neurons stressed by ischemia and secondary events are lost later than neurons in the ischemic core, providing a chance for therapeutic interference that may be applied hours or days after stroke [1,5,7,12] (Figure 1). Thus, neuroprotective strategies aim to preserve this brain tissue, attempting to improve overall outcomes after an ischemic episode [7,12-14].

1.1.1.1. Neuroprotection

Neuroprotection refers to any strategy, directly targeting the brain parenchyma, aiming to antagonize the injurious processes that occur and persist in the brain after ischemia [2,13,14]. Several studies on neuroprotective agents have been successfully carried out in animal models, reaching clinical trials. Examples of these therapeutic agents are Ca^{2+} channel blockers (*e.g.* nimodipine), glutamate antagonists acting through NMDA receptor antagonism (*e.g.* GV150526 and magnesium sulphate), anti-oxidants (e.g. ebselen and edaravone), phospholipidic precursors (*e.g.* citicoline) and hemodiluting agents (*e.g.* dextran 40) [2,3,13,14]. However, despite years of investigation, translating experimental work into effective drug therapies has been extremely difficult [2,13]. The dual role of some ischemic mediators, inappropriate selection of patients and clinical outcome measures, incorrect time-window treatment estimation for the trials, inability to achieve efficacious drug-doses or plasma levels and heterogeneity of stroke in humans are some of the issues pointed for the disappointing results on clinical trials [7,12,14]. In preclinical studies, animal model related factors and standardization and validity of functional/behavioural testing are two further important factors that have to be well analysed for a successful translation [4,14,15].

It is important to have in mind that there is only one approved drug for ischemic stroke treatment (tPA) and that it acts as a thrombolytic agent, inducing reperfusion [3,5,7]. Even though replenishment of blood flow and subsequent delivery of oxygen and nutrients is crucial, tPA is still a restricted method to limit neuronal death [14]. Moreover, a very low percentage of patients with ischemic stroke receive tPA treatment because of its short time window for administration (4.5h) and associated risks of subsequent haemorrhage [2,5,7,14]. Thus, inducing neuroprotection might be a promising alternative or combinatorial approach with tPA to limit the expansion of infarcted tissue and to preserve neuronal functions [13].

1.1.2. Mammalian Rho GTPases

About one percent of the human genome encodes proteins that either regulate or are regulated by direct interaction with members of the Rho family of small GTPases [16]. Rho GTPases are guanine nucleotide-binding proteins (G proteins) [17] that belong to the Ras superfamily of GTPases [16]. The distinct family of Rho GTPases comprise 20 signalling molecules. These members are distributed in 8 subfamilies based on their sequence similarities [18]. Ras homolog gene family, member A (RhoA), Ras-related C3 botulinum toxin substrate 1 (Rac1) and cell division control protein 42 homolog (Cdc42) are the three best-characterized members of Rho GTPase family and each one is included in a different subfamily [18,19]. Typical Rho GTPases switch between an active GTP-bound state and an inactive GDP-bound state. This activity is tightly regulated by guanine nucleotide exchange factors (GEFs) that catalyse exchange of GDP for GTP to activate the Rho GTPase [20]; GTPase-activating proteins (GAPs) that stimulate the intrinsic GTPase activity to inactivate the Rho GTPase [21]; and guanine nucleotide dissociation inhibitors (GDIs), that extract Rho GTPases from cell membranes to prevent their inappropriate activation and to protect them from misfolding and degradation (Figure 2) [17].

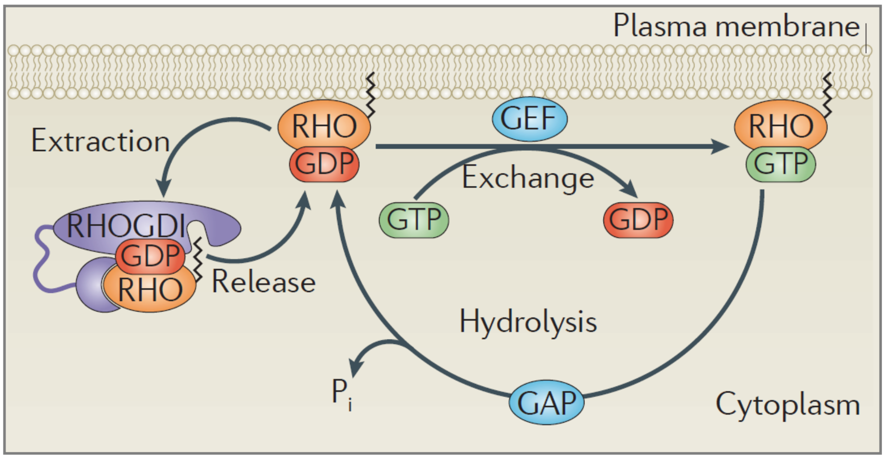

Figure 2 Schematic representation of the Rho GTPases regulation. GEFs mediate Rho GTPases activation through GDP exchange for GTP while GAPs have the opposing function. GDIs maintain Rho GTPases in the cytoplasm in an inactive state. Adapted from [17].

Concerning their function, RhoA induces formation of actin stress fibers and focal adhesions, Rac stimulates protrusion of lamellipodia and membrane ruffles, and Cdc42 promotes extension of filopodia [18]. Within Rac isoforms, Rac1 is ubiquitously expressed, Rac2 is expressed in hematopoietic system and Rac3 is found in all cells but mostly in the brain [22]. Though best documented for their function on actin cytoskeleton regulation [18], Rho GTPases participate in a vast variety of other functions in all cell types. They have important roles in the regulation of cell polarity, gene expression, cell cycle progression, microtubule dynamics, vesicular transport pathways, cell migration, cell differentiation and enzymatic activities such as NADPH oxidase (Nox) function [16,18]. This last relevant feature is exclusive of Rac GTPases, which being a component of the Nox complex have the capacity to induce its activation [18]. This enzyme produces reactive oxygen species (ROS) not only in phagocytic cells but also in nonphagocytic cells, such as neurons [23]. Regarding other Rac1 functions, both gene expression and cell cycle progression are associated with its ability to translocate to nucleus [24]. Having a nuclear localization signal (NLS), Rac1 can cycle between inside and outside the nucleus promoting cell cycle progression [25]. In nucleus, it can also interact with transcription factors interfering with gene expression [24].

1.1.2.1. Rho GTPases in the nervous system

In the nervous system, Rho GTPases and their downstream effectors play major roles in neuronal development, synapse plasticity and neuronal survival [26]. Importantly, all of these roles are intimately correlated to their importance in the actin cytoskeleton regulation [18,27-29].

1.1.2.1.1. Neuronal development

The importance of Rho family of GTPases is noticed in different aspects of neuronal development, including neurite outgrowth, axon pathfinding, and dendritic spine formation [29]. It is consensual that these signalling molecules act antagonistically toward each other to determine neuronal morphology. In this context, the antagonism between Rac and Rho functions is well reported, with Rac typically eliciting neurite outgrowth, axonal extension and dendritic spine morphogenesis and Rho generally opposing these effects [27,29].

Focusing on Rac1, it has been shown that this Rho GTPase affects neuritogenesis [29] and, more recently evidenced, neuronal proliferation [28]. Adhesion and differentiation are two further important events in neuronal development in which Rac1 was found to participate [22].

1.1.2.1.2. Synapse plasticity

The dynamic structure of dendritic spines is vital for synaptic activity [30,31] as >90% of excitatory synapses are formed there [32]. Analysis of the signalling pathways that underlie the effects of NMDA receptors on dentritic spine architecture highlights the crucial role of Rho GTPases in synaptic plasticity [33]. NMDA receptors activity enhances dendritic spine formation [26] and has been correlated with modulation of Rho GTPases activity [34]. The work of Tejada-Simon *et al.* demonstrated that in mature neurons, activation of the NMDA receptor increases the amount of active Rac1 and causes translocation of Rac1 from the cytosol to the membrane. This facilitates the Rac1-dependent dendritic spine formation [35] and synapse morphology during activity-dependent plasticity. Synapse plasticity is thus a consequence of the structural plasticity of dendritic spines in response to an external stimulus, such as injury [36] or induction of long-term potentiation (LTP) [30] (enduring increase in the amplitude of excitatory postsynaptic potentials considered to be a cellular model of learning and memory [31]).

Specifically in learning and memory, Rac1 was required for a learning-evoked increase in the proliferative production of new hippocampal neurons, but it was not needed to maintain the basal neurogenesis in animals housed in an unchanging environment [37]. In other study, when Rac1 was eliminated from neurons, altered dendritic spine size, reduced spine density, and impaired traditional measures of plasticity, such as hippocampal LTP were found [38].

Other stimulus that alters dendritic spine morphology are psychostimulants, as cocaine [39]. In a study made by Dietz *et al*., Rac1 signalling was found to mediate structural and behavioural plasticity in response to cocaine exposure. This finding and the others cited herein support the importance of Rho GTPases and specifically of Rac1 on synaptic plasticity.

1.1.2.1.3. Neuronal survival

Studies on spinal motor neurons have demonstrated the importance of RhoA in the survival of developing neurons and of Rac1 in the survival of embryonic neuronal primary cultures [26]. Nevertheless, in situations of degenerative insults, RhoA activation typically elicits neuronal apoptosis [28]. As for Rac1, *vitro* studies on cerebellar granule neurons (CGNs) have also shown that it contributes to neuronal survival [26]. Two known pathways over which Rac1 acts to promote neural survival are PAK through mitogen-activated protein kinases (MAPK) activation and phosphoinositide 3-kinase/Akt ((PI3K)/Akt) [28].

More recently, an *in vivo* study addressing Rac1 function on neuronal survival revealed that Rac1 mediates cell survival of retinal ganglion cells after optic nerve injury [40]. On the other hand, in another *in vivo* study, Rac1 depletion in mouse rod photoreceptors protected them against light-induced photoreceptor death [23] having no effect on retinal structure or function. In agreement with this last idea, Rac1 loss in mature hippocampal neurons did not affect neuronal survival during learning [37]. These different results may be justified, in part, by the use of different neuronal populations and also by the fact that studies were made in distinct conditions: injury, stress and learning. Therefore, Rac1 function in neuronal survival have to be carefully evaluated depending on the context that is being studied.

1.1.3. Rho GTPases in brain ischemia

Growing evidence suggests that Rho family GTPases dysregulation may induce neuronal death after brain ischemia [26,28]. Therefore, several studies have addressed the role of these molecules in ischemia. Nevertheless, targeting the RhoA/Rho-associated protein kinase (RhoA/ROCK) pathway has been the most highlighted approach for the treatment of ischemic stroke [41-43].

RhoA is activated in rat CGNs after excitotoxic stimulation with the addition of glutamate [44]. This leads to the downstream activation of p38α MAPK, a stress activated protein kinase, which ultimately induces apoptosis of CGNs. The mentioned pathway is responsible for apoptosis also in primary cortical and hippocampal neurons exposed to NMDA [44]. The same authors also observed RhoA activation in mouse cerebral cortex following occlusion of the middle cerebral artery (MCA), a much used model of focal ischemia, which is confined to a particular region of the brain [44].

In vivo, human brains from stroke patients showed an upregulation of RhoA in comparison to controls [45]. It is known that RhoA exerts its harmful functions on ischemia trough ROCK, its downstream effector [4,46]. Rikitake *et al.* showed that administration of fasudil or Y-27632, two different ROCK inhibitors, reduced cerebral infarct size and improved neurologic outcome in mice after MCA occlusion (MCAO) [42]. Indeed, there is a correspondence between the increase in ROCK activity and the severity of neurological deficit and infarct size in a rat cerebral thrombosis model [47]. In a meta-analysis performed addressing RhoA and ROCK inhibition studies on ischemic stroke until 2011, it was concluded that the efficacy of these treatments was higher in thrombotic and temporary models rather than permanent ischemia models, which do not have reperfusion. This was attributed to the proposed mechanism of action of these inhibitors by increasing vasodilation and therefore cerebral blood flow [48]. However, there is also evidence showing that RhoA/ROCK inhibitors exert neuroprotection via reduction on inflammatory responses [41] as well as by direct actions on neurons, through inhibition of the pro-apoptotic mixed-lineage protein kinase 3 - c-Jun N-terminal kinase (MLK3-JNKs) signal transduction pathway [43].

RhoB, however less well-studied, was also found to be upregulated in human brains after stroke [45]. Moreover, RhoB expression is important for caspase-3 activation in neurons, which is correlated with apoptosis [49]. This evidence suggests that this Rho GTPase may also have a detrimental role after ischemia.

Concerning Cdc42 role on brain ischemia, it was verified an upregulation of its activity after global ischemia, which lead to the activation of MLK3-JNKs pathway [50], which may also suggest this Rho GTPase as a target in brain ischemia.

Among Rho GTPases, RhoA/ROCK pathway is, at this moment, the most promising pathway to target in order to achieve neuroregeneration after ischemia. However, in the last years attention was directed toward the involvement of Rac1 in neurodegeneration [51] and emphasis has been given to the role of neuronal Rac1, on the ischemic brain response [52].

1.1.3.1. The role of Rac1 GTPase in brain ischemia

Many studies have been shown the activation of Rac1 [52-57] and also its cellular redistribution [58,59] following ischemia. Back in 2000, Ozaki *et al.*, demonstrated for the first time that Rac1 inhibition, achieved by the expression of a dominant negative Rac1 mutant, protected against ischemia/reperfusion (I/R) injury *in vivo* through suppression of ROS production [56]. Although this study was performed in the liver, subsequent studies have supported the crucial role of Rac1 GTPase activation in the induction of oxidative stress in endothelial [53,60] and neuronal [23,52,54,55] cells.

As an example, Rac1 inhibition, using atorvastatin or *C. difficile* lethal toxin B, prevented I/R-induced BBB disruption *in vivo* [53]. In this study, Nox inhibition or genetic deletion of the Nox2 isoform also prevented BBB dysfunction. This indicates that the neuroprotective effect observed for Rac1 inhibition was due to the decrease in ROS formation, since Rac1 has a known role for Nox activation [18]. In Sawada *et al.* study, deletion of Rac1 in endothelial vascular cells reduced infarct size and edema volume, while also improving neurological outcomes in a model of focal cerebral ischemia [60]. This neuroprotection was mediated by the release of neurotrophic factors and by the decrease on ROS generation and Nox activation.

In a neuronal cell line, expression of a dominant negative mutant of Rac1 strongly blocked glutamate-induced ROS generation and cell death [55]. Nevertheless, in another *in vitro* assessment of glutamate toxicity effect, in cortical neurons, dominant negative Rac and NSC23766 (specific Rac1 inhibitor) increased neuronal cell death [58]. These contradictory results may be explained, partially, by the use of different concentrations and time exposures to glutamate. Despite this, *in vivo* studies have demonstrated that Rac1 is a main contributor to oxidative stress-induced neuronal death. Haruta *et al.* showed that *in vivo* elimination of Rac1 on mouse rod photoreceptors protected them against photo-oxidative stress [23]. In an *in vivo* study addressing the role of Rac1 after brain ischemia, Raz *et al.*, verified that NSC23766 administration, prior to global cerebral ischemia induction on mice, attenuated almost completely post-ischemia oxidative stress in the hippocampus CA1 region. Oxidative stress damage markers were attenuated with Rac1 inhibition and rats treated with NSC23766 showed a significant improvement in their cognitive capabilities, achieving similar spatial memory abilities on day 8 post-reperfusion compared with non-ischemic rats [52]. A very recent study examined the effects of post-ischemia inhibition (using NSC23766) and knockdown (via antisense oligonucleotides (ASOs)) of Rac1 in a mice MCAO model [54]. At 72h after reperfusion, treated mice showed lower neurological behavior scores, *i.e.* less neurological dysfunction, and smaller infarct areas compared with the untreated controls. Furthermore, treated brain showed higher levels of important antioxidant enzymes and lower levels of an indicator of lipid peroxidation. Rac1 ASOs and NSC23766 treatment also protected against neuronal cell death *in vivo* and *in vitro* (on hippocampal neurons) and decreased ROS intracellular levels *in vitro*. Finally, these authors found that Rac1 inhibition on neuron stem-like cells promoted its differentiation, which constitutes an important finding as these cells can migrate into the ischemic region and contribute to ischemic tissue regeneration [54]. In line with this last finding, the already mentioned study of Haditsch *et al.* showed that Rac1 loss lead to neuronal progenitor cells cell-cycle exit [37].

Importantly, Rac1 has been correlated with hypoxia inducible factor (HIF) production [61-63], which is linked to the activation of neuroprotective pathways on ischemia [14]. Some studies state that Rac1 is important for HIF production induced by thrombotic factors or by hypoxia in vascular smooth muscle cells [62] and in a hepatocyte cell line, respectively [63]. However there is also a report in which Rac1 negatively regulated HIF production, under ischemic conditions, in another hepatocyte cell line [61]. Thus, the role of Rac1 on HIF production may differ amongst different cells and tissues [10]. Specifically on neuronal cells, more studies are required to clarify the importance of Rac1 on HIF production on ischemic acute phase.

It is of relevance to refer that in the above mentioned studies by Nikolova *et al.*, Haruta *et al.* and Raz *et al.*, neuroprotection was also achieved by pharmacological Nox inhibition [23,52,55], emphasizing the role of Rac1 on Nox activation. This evidence along with all the findings presented herein, strongly suggests that targeting Rac1 might be a promising approach for neuroprotection since Nox assembly becomes impaired and consequently the production of ROS is diminished (Figure 3A).

Despite the existence of a vast number of studies addressing Rac1 importance on Nox activation following hypoxia, Rac1 appears to interfere as well with other pathways likewise pivotal for neuronal death after an ischemic episode. Rac1 activation following global brain ischemia was associated to neuronal apoptotic cell death in the hippocampus CA1 region through activation of the JNK signaling pathway [57]. This study revealed a significant increase on a complex formed by POSH (plenty of SH3s), scaffold protein that activates MLK3-JNK pathway, and Rac1 following *in vivo* ischemia. In line with these findings, in another work, Zhang *et al.* showed that induction of Akt activation, which is naturally suppressed following cerebral ischemia, negatively regulates Rac1 and POSH after cerebral ischemia and this accounts for Akt pro-survival effect on the brain [64]. Thus, this study also highlighted the importance of Rac1 inactivation for neuronal survival after ischemia. This evidence suggests that activation of the

JNK pro-apoptotic pathway is one of the detrimental mechanisms controlled by Rac1 after ischemia (Figure 3B).

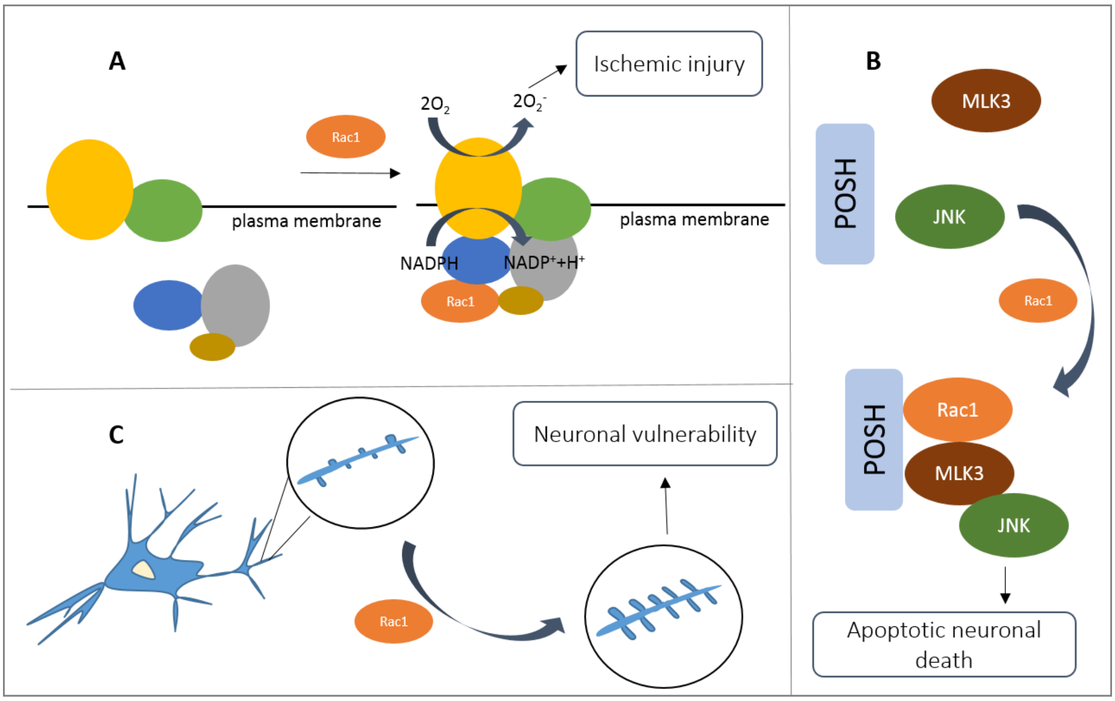

Figure 3 Overview of the different pathways through which Rac1 may contribute the neuronal death after neuronal ischemia. (A) Rac1 is needed for Nox assembly and activation, which increases ROS production and therefore contributes to ischemic-induced oxidative stress that worsens ischemic injury. (B) POSH-Rac1-MLK3 complex activates the pro-apoptotic JNK signalling. (C) Rac1 promotes dendritic spine growth increasing neuronal vulnerability to ischemia.

Hippocampal CA1 neurons have a high sensitivity to hypoxia [3]. In Bianco-Suárez *et al.* study, this high sensitivity was associated to a much reduced spine shrinkage in comparison to other neuronal cell population, in response to hypoxia. Tiam1, a Rac-specific GEF, was downregulated using small hairpin RNA (shRNA) which conduced to an increased spine shrinkage of the hippocampal neurons and to a significant decrease on apoptotic cells, following OGD [65]. Spine shrinkage may conduce to neuroprotection once it leads to a reduced excitatory synaptic input and thus reduced excitotoxicity [66]. Furthermore, cytoskeleton disruption, which includes spine collapse may be neuroprotective as it allows for cells to preserve energy (ATP) [67]. Thus, Bianco-Suárez *et al.* study proposes Tiam1/Rac1 pathway activation as a source of hippocampal susceptibility to ischemia. Although in this study, hippocampal cells did not show an increased spine growth but instead a very reduced spine shrinkage, *on in vivo* studies, spine growth was verified in hippocampal neurons after global cerebral ischemia [68]. An increase on spine length after focal ischemic stroke was also verified on cortical neurons [69]. Along these lines, it is suggested one further pathway through which Rac1 contributes to neuronal death (Figure 3C).

Further studies reinforcing Rac1 involvement in brain ischemia are related to neuroglobin, a molecule activated following hypoxia that protects neurons from death. Its neuroprotective function was explained through inhibition of Rac1-GDI dissociation, maintaining Rac1 in an inactive state [59]. This study is in line with the ideas discussed herein, supporting the importance of Rac1 activity inhibition to achieve neuroprotection after stroke.

Notwithstanding the increasing awareness for the injurious role of Rac1 in the initial stages after brain ischemia, there is also evidence suggesting an important role of Rac1 activation for neurological recovery on later stages of ischemic stroke [54,58]. For instance, Rac1 activity is important for synaptic plasticity [38] and may play a critical role on the rewiring of neuronal circuits lost to stroke [36,58]. A major concern when evaluating therapies for stroke is that the same cellular and molecular mechanisms that are detrimental in the short-term, may be vital for long-term repair [12,13]. Thus, to achieve appropriate time of therapeutic interventions it is critical to realize when, where and how damaged brain switches from injury to repair [12].

The fact that Rac1 interferes with different mechanisms of cell death, in a field in which the paradigm is the use of multifactorial drugs [2,7], along with the benefic effect of its inhibition after cerebral ischemia [54], make it an attractive target. However, further studies are needed to confirm the effect of Rac1 elimination in other brain ischemia models and address the proper time for intervention so as to realize at which point Rac1 inhibition stops being beneficial and starts being detrimental. Thereby, upcoming studies should use different approaches and ischemia models and ultimately clarify long-term consequences of Rac1 elimination.

1.2. Use of RNAi as a therapeutic strategy

RNA interference (RNAi), an evolutionary endogenous gene regulation mechanism, has been shown to be a robust, efficient and reliable tool to achieve gene silencing [70,71]. RNAi is, thus, regarded as a therapeutic strategy that, by silencing a targeted gene, causes the inhibition of protein synthesis [72]. Gene silencing mediated by RNAi involves the action of double-stranded siRNA molecules, which upon entrance in the cellular cytoplasm are incorporated into RNA-induced silencing complexes (RISCs) (Figure 4). Only one strand of the RNA (antisense) is retained in these complexes while the other is degraded by a RISC endonuclease - argonaut 2 (Ago2). The activated RISC can, then, recognize and bind to the complementary region in the target messenger RNA (mRNA), which is going to be cleaved by Ago2. Cleaved mRNA is further degraded by intracellular RNAses and siRNA-activated RISC is recycled allowing for its interaction with other mRNAs. Thus, a single RISC complex can slice numerous mRNA targets [73,74].

RNAi-based therapeutics represent a great promise for the medical field owning to their capability to specifically target any gene [70,73,75]. Furthermore, even when comparing to antisense strategies, such as ASOs, siRNA is considerably more potent in targeting mRNA cleavage [70] and shows higher intracellular stability when not incorporated in the RISC [73]. Despite its potential, siRNA therapeutic application has been hindered by its rapid intracellular and extracellular degradation (due to nucleases activity), non-specific distribution and poor cellular uptake [70,71,76]. Chemical modifications of siRNA aiming at increasing its stability have been developed. Nonetheless, delivery systems are required to achieve cellular targeting and improve cellular uptake in order to achieve effective sequences delivery [73,76]. These gene delivery systems can use viral or non-viral vectors, with the former being more efficient in transfecting cells. Though, viral systems comprise major drawbacks, as possible toxicity, immunogenicity, inflammatory potential or even insertional mutagenesis, in which there is the ectopic chromosomal integration of viral DNA. Thus, the safety concerns raised for viral delivery systems prompted the search for alternative effective non-viral systems, such as the use of nanomaterials [70,71].

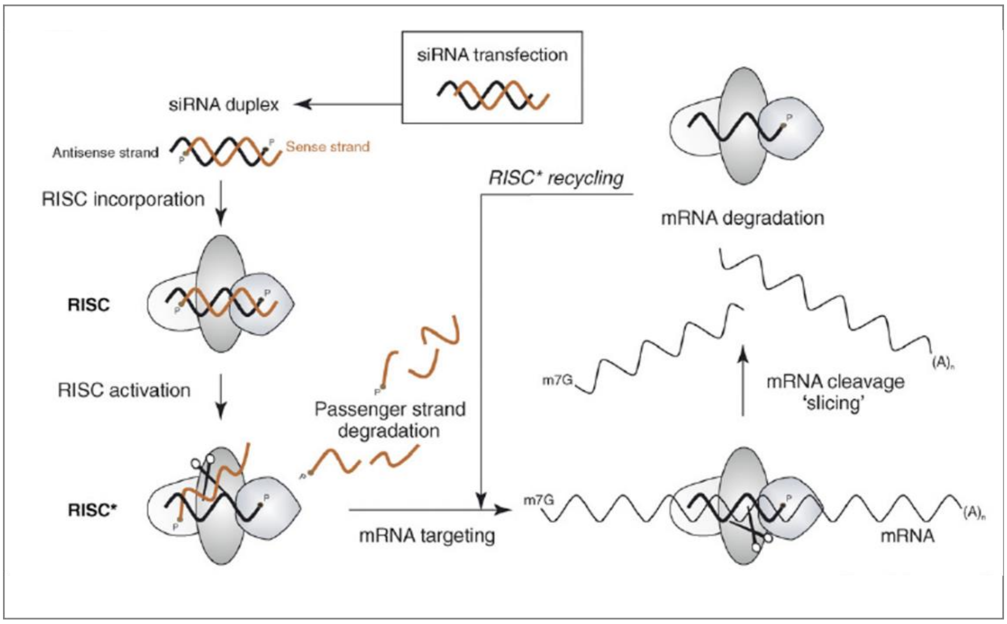
siRNA transfection
siRNA duplex
Antisense strand
Sense strand
RISC incorporation
RISC
RISC activation
RISC*
Passenger strand degradation
RISC* recycling
mRNA degradation
m7G
(A)n
mRNA cleavage 'slicing'
mRNA targeting
m7G
(A)n
mRNA

Figure 4 Cellular mechanism of RNAi mediated by siRNA. After transfection, siRNA is incorporated into RISC, which maintains one RNA strand (antisense or guide strand). The siRNA guide included in the active RISC (RISC*) recognizes the target sequence, which is then degraded by Ago2. Intracellular ribonucleases further degrade the mRNA fragments due to the lack of a 50-cap and a poly(A) tail. Adapted and modified from [73].

1.3. Chitosan-based nanoparticles for the delivery of siRNA

1.3.1. Chitosan potential and important considerations for siRNA delivery systems

Chitosan is a linear polysaccharide obtained by deacetylation of chitin, which is the structural element in the exoskeleton of crustaceans. This polymer is composed of randomly distributed N-acetyl-D-glucosamine and β-(1,4)-linked D-glucosamine (Figure 6A) [70,71,77,78]. Owing to its positive charges that allow for the electrostatic interaction with negatively charged siRNA sequences for nanoparticle formation, chitosan has been extensively explored as siRNA carrier [70,72,74,76,77,79-82]. Additional features that confer to chitosan unique properties for siRNA delivery include its biocompatibility, biodegradability, low immunogenicity and reduced cytotoxicity [71,74,83]. Comparing to cationic synthetic polymers, chitosan possesses a lower charge density, which in one hand may be responsible for a lower transfection efficiency but, in the other hand, is accountable for its lower toxicity [71,74,84]. Also, immunogenicity issues are sometimes raised for much used synthetic polymers [74]. Notoriously, there is already a commercially available DNA transfection agent based on oligomeric chitosan (Novafect from Novamatrix) [74], which emphasizes chitosan potential for nucleic acids delivery.

In order to efficiently deliver siRNA sequences to the cellular cytoplasm, chitosan-siRNA nanoparticles have to surpass several extracellular and intracellular barriers. In a biological environment, nanoparticles have to be resistant to destabilization on the extracellular fluids and escape from the host immune recognition systems [70,74]. After reaching the cells, nanoparticles uptake may be mediated by non-specific interactions with the cell membrane or through receptor-mediated endocytosis, the latter being clathrin- or caveolae-mediated [74,84,85]. Importantly, chitosan positive charges constitute an advantage for interaction with cellular membranes, while its membrane-disturbing properties may help on the cellular uptake [71]. Following internalization, particles need to escape the endosomal pathway avoiding cargo degradation in lysosomes [70,74,81,84]. Finally, complexes unpackaging must occur for sequences to exert their function [70,71,74]. Figure 5 gives an overview of the different intracellular barriers that nanoparticles have to overcome.

The ability of chitosan-siRNA complexes to efficiently transfect cells depends on different parameters, such as: 1) chitosan molecular weight (M_w), which is proportional to the chain length; 2) chitosan degree of deacetylation (DD), which represents the fraction of ionizable monomers; 3) the ratio of chitosan amines to RNA phosphates (N/P) used to form particles and, 4) the formulation method [70,74,76]. Chitosan M_w influences the size (generally higher for higher M_w), morphology and/or stability of the nanocomplexes, which has repercussions on particles biological activity [74]. Higher DD results in increased positive charge, which allows for a greater nucleic acids binding capacity. Owing to its rigid topology and short length, siRNA needs a high number of positive charges to be efficiently bound [70,74]. A study of Malmo *et al.* showed that fully de-N-acetylated chitosan exhibited more effective endosomal escape than partially de-N-acetylated chitosan because of its high charge density, highlighting the importance of chitosan DD [86]. The N/P ratio should also be optimized depending on the type of chitosan and formulation process used [74]. Importantly, higher amounts of chitosan, and thus higher N/P ratio, are correlated with higher endosomal osmotic pressure, which enables a higher endosomal release [70]. Nevertheless, these formulations may also bring significant problems including aggregation and nonspecific effects of uncomplexed chitosan [76,86]. There are two main methods for siRNA-loaded chitosan nanoparticles formulation [74]. Simple complexation was the first method described and consists of mixing siRNA with chitosan [75]. The other formulation method (ionic gelation) uses a cross-linker agent, such as sodium tripolyphosphate or sodium sulphate (Na_2SO_4), which confers a better binding capacity and loading efficiency to the NPs due to the strengthening of siRNA-chitosan interaction [70,74,77].

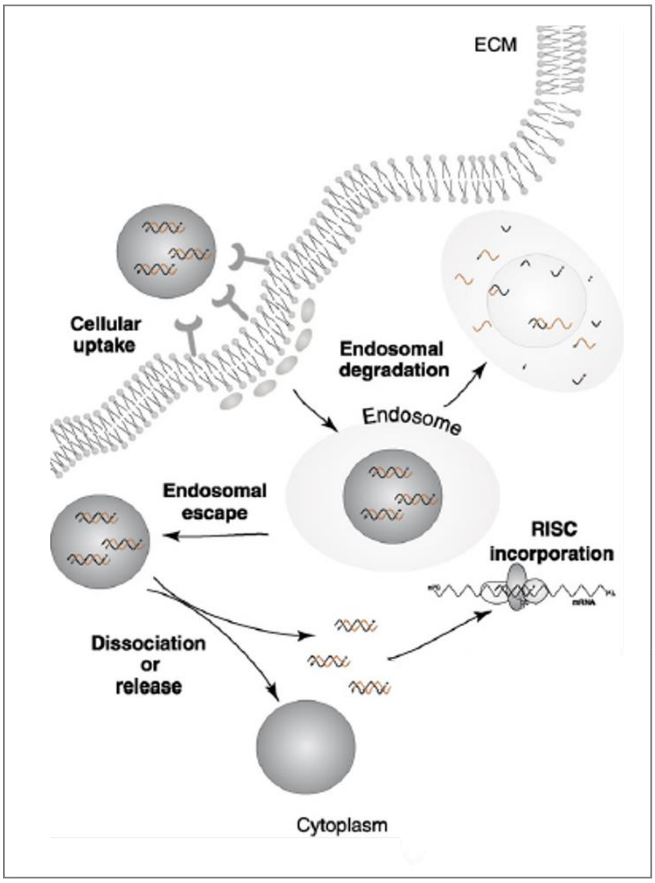

Figure 5 Intracelullar barriers for nanoparticle-mediated siRNA delivery. After cell internalization, nanoparticles must escape endosomal degradation and dissociate its cargo on the cellular cytoplasm, where it can be incorporated in the RISC and exert its silencing function. ECM= extracellular matrix. Adapted and modified from [73].

Notwithstanding its attractive features, siRNA-loaded chitosan nanoparticles can be improved in order to increase their transfection efficiency and overcome some limitations, namely: 1) the nonspecific cellular uptake, 2) poor buffering capacity and 3) the low solubility and stability in biological fluids [70,71,74]. Ligand conjugation and structural modifications are two widely used strategies to improve chitosan characteristics [70,74]. Selective uptake of nanoparticles as well as reduced accumulation in non-target tissues can be achieved by delivering siRNA specifically to the cell type of interest [74]. Conjugation of cell-specific targeting ligands on the nanoparticle surface allow for its recognition and subsequent uptake [70]. Combination of chitosan poly(ethylene imine) (PEI), an amine rich polymer, resulted in high gene silencing [81]. This is attributed to the fact the in acidic pH, the amino groups are protonated, leading to the rupture of the endosome and release of the siRNA [74]. Thus, chitosan conjugation with agents capable of promoting endosomal escape, such as amine rich polymers, may significantly increase nanoparticles transfection efficiency. Finally, chitosan nanoparticles conjugation with hydrophilic polymers, such as poly(ethylene glycol) (PEG), has been widely used attempting to improve siRNA-loaded particles stability and solubility in physiological conditions [71,80]. This poor solubility of chitosan at physiological pH (7.4), which results in lack of stability, is owed to the fact that chitosan primary amines have a pKa value of about 6.5. This constitutes a great limitation for chitosan *in vivo* administration [70,71,77,78].

TMC, a chitosan derivative formed by the quaternization of chitosan amino groups [71,77,78], has been explored to overcome chitosan low solubility (Figure 6B). Quaternization confers to TMC a permanent positive charge, which enhances both electrostatic interactions during complex formation and solubility at neutral pH [78,87]. This chitosan derivative has been found to increase *in vitro* transfection efficiencies with plasmid DNA (pDNA) [87] and with siRNA [77], comparatively to chitosan.

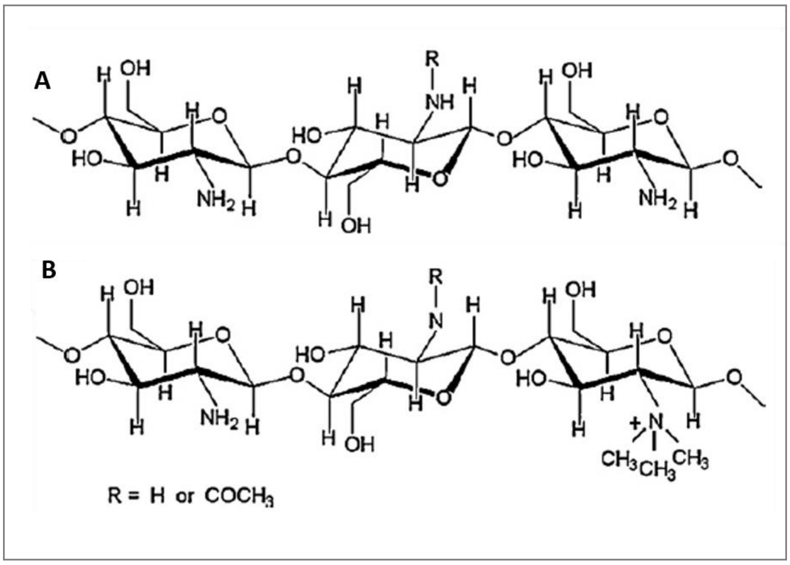

Figure 6 Chitosan and TMC chemical structures. (A) Subunit of chitosan displaying β-(1-4)-linked D-glucosamine (deacetylated unit) and N-acetyl-D-glucosamine (for R=$COCH_3$, acetylated unit). (B) Modified glucosamine-units of trimethylated chitosan. Adapted from [77].

1.3.2. Intranasal route for successful non-viral nucleic acids delivery to the brain

Drugs delivery to the central nervous system (CNS) has been a challenge in the medical field, which has prompted much effort towards the development of strategies targeting, for example, the brain. Vascular and intracranial drug delivery routes are two much studied approaches to direct therapeutic agents to the brain, however there are still serious limitations in their application [88]. Vascular route is attractive for drugs to be delivered in the whole brain as each neuron has its own brain capillary [88]. Nonetheless, BBB restricts the entry of most macromolecules in the brain, which impairs the success of targeting the brain through intravenous administration of the drug formulation. Moreover, systemic administration usually leads to loss of the therapeutics in other organs [88,89]. Local intracranial brain delivery by direct injection of the drugs bypasses the BBB and the losses in other organs. It also decreases the chances of nanoparticles destabilization. However this is an invasive strategy, not being appropriate for translation studies, and has some limitations, such as clearance into the venous and lymphatic systems before tissue penetration and reduced diffusion from the site of administration [88,89].

Intranasal drug delivery is emerging as a noninvasive route that circumvents the BBB, improving CNS penetration of the therapeutic agents. Thus, it has generated much interest for brain drug delivery [72,89,90]. After nasal application, macromolecules are in contact with the nasal epithelium, which is constituted by the olfactory and respiratory regions. Nanoparticles can gain access to the rostral part of the brain through olfactory nerves located at the olfactory region (olfactory pathway) whereas caudal parts of the brain can be reached through trigeminal nerves found at the respiratory region (trigeminal pathway) (Figure 7) [72,82,91]. Nevertheless, different transport mechanisms may be involved on the transport to the brain as described below.

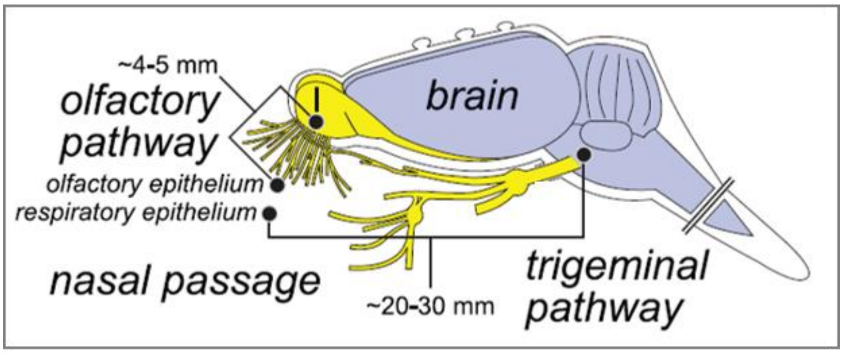

Figure 7 Schematic representation of nose-to-brain pathways and approximate average distances from the olfactory and respiratory epithelium to CNS targets. Adapted and modified from [91].

To reach the brain, particles have to cross the epithelium, pass from the nasal mucosa to entry points of the brain and, finally, be transported from these entry points to the other sites of the CNS [91]. Transport across the epithelium can occur either by intracellular or extracellular pathways [90,91]. Within the olfactory epithelium, intracellular pathways include endocytosis into olfactory sensory neurons (OSNs) with subsequent intraneuronal transport and transcytosis, across sustentacular cells, to the lamina propria (Figure 8). Extracellular or paracellular transport to the lamina propria occurs through tight junctions between cells [83,91]. Substances transported intracellularly through OSNs can gain direct access to the OB whereas particles reaching the extracellular environment of the lamina propria can have different fates, as depicted on Figure 8.

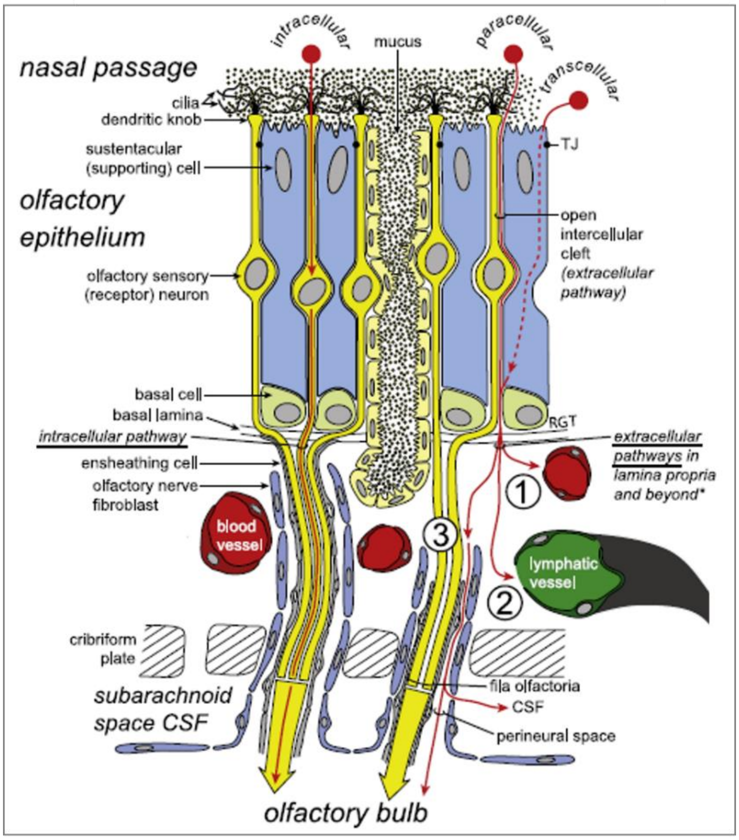
intracellular
mucus
paracellular
transcellular
nasal passage
cilia
dendritic knob
sustentacular (supporting) cell
TJ
olfactory epithelium
open intercellular cleft (extracellular pathway)
olfactory sensory (receptor) neuron
basal cell
basal lamina
RGT
intracellular pathway
extracellular pathways in lamina propria and beyond*
ensheathing cell
olfactory nerve fibroblast
①
blood vessel
③
lymphatic vessel
②
cribriform plate
subarachnoid space CSF
fila olfactoria
CSF
perineural space
olfactory bulb

Figure 8 Particles transport across the olfactory epithelium to the brain. Axonal processes of OSNs converge into bundles (fila olfactoria), surrounded by ensheathing cells and fibroblasts, that are projected to the OB. Potential pathways for particles delivery following intranasal administration are represented in red. Some substances may be transported by an intracellular pathway, while others may cross the olfactory epithelial barrier by paracellular or transcellular transport, reaching the lamina propria, where different extracellular pathways for distribution are possible: 1) absorption into olfactory blood vessels; 2) absorption into olfactory lymphatic vessels; 3) extracellular diffusion within extracellular spaces surrounding nerve bundles. Conceivable pathways for distribution of substances from the perineural space into the OB or into the CSF are shown. Adapted and modified from [91].

These include: 1) absorption into blood vessels and entry into the circulation; 2) absorption into lymphatic vessels and 3) extracellular diffusion within extracellular spaces surrounding nerve bundles, with subsequent entry in the cranial compartment [90,91]. Drugs entering the blood circulation have to cross BBB to reach the brain after diffusion from the cerebrospinal fluid (CSF), however only sufficiently hydrophilic molecules are able to exploit this mechanism. On the other hand, substances that escape local absorption into the blood stream or to the lymphatic system, may enter the CNS through perineural spaces or diffuse from perineural spaces into the CSF (and from there to the brain) [83,90,91]. Reaching the brain, particles can be distributed to different areas through intracellular and extracellular transport (*e.g*. distribution through convective transport within the cerebral perivascular spaces or local diffusion at the entry points) [91].

Lochhead and Thorne were able to predict the time required for IGF-1 (insulin-like growth factor-1) to reach the brain through intracellular or extracellular pathways, based on the knowledge of the distances between the epithelium and the OB or the caudal brainstem (denoted in Figure 7). The authors reported a duration of 0.74–2.7h and 3.7-13h for the intracellular transport, through the olfactory and trigeminal pathways, respectively. For the extracellular diffusion, the transport to the OB and brainstem was predicted to take 0.73–2.3h and 17–56 h, respectively. They also suggest an additional pathway for the extracellular transport, through convective process, such as bulk flow of fluid within perivascular spaces of blood vessels traveling with the peripheral olfactory or trigeminal systems. This transport was expected to be faster taking at most 0.33h to reach OB and 1.7h to reach the brainstem [91]. Thus, at least for frontal parts of the brain, the intranasal route can be considered relatively fast.

Focusing on chitosan as a non-viral carrier of siRNA, the stability of the nanoparticles formed with siRNA is a very important concern for its *in vivo* application. For systemic delivery, blood components can destabilize the delivery vehicle, while serum proteins, such as albumin or fibrinogen, can cause nanoparticles aggregation, which can result in embolism and increased toxicity [74]. For direct delivery at the mucosal surfaces, the highly enzymatic environment found by nanoparticles also requires a high stability and capability to protect siRNA [90]. Other main barrier for nasal delivery is the mucociliary clearance that limits the time available for drug absorption [71,90]. Chitosan possesses highly desirable mucosa adhesion and permeation properties for nasal delivery [71,83]. Thanks to its mucoadhesion ability, chitosan can reside more time on the olfactory region and this increases the chances of absorption. Additionally, acting as a permeation enhancer, chitosan opens intercellular tight junctions, thereby facilitating the paracellular transport of therapeutic agents [83]. Thus, chitosan is expected to be transported mainly through the extracellular pathways described above.

Generally, higher M_w and free amino groups (DD) promote a stronger mucosa adhesion [83]. Moreover, protonated chitosan has been shown to be important for the capacity of chitosan to open tight junctions. Particularly, TMC has been reported to enhance the permeability of the nasal epithelium due to its fixed positive charges [78,83]. The degree of quaternization of the TMC (DQ), correspondent to the proportion of deacetylated primary amine groups grafted with methyl groups, seems to influence its paracellular transport, with higher DQ conducing to an enhancement on particles permeation [76].

A recent study proved the efficacy of the delivery of siRNA through nasal route to the mice brain, using chitosan nanoparticles as a vector [72]. The authors used a PEGylated formulation of chitosan tagged with two different peptides, TAT, a cell penetration peptide and MGF, an alternatively spliced variant of IGF-1. The latter was used for its affinity to target neuronal tissues.

Attending to the advantages of chitosan, and particularly of TMC, administration through intranasal route to target the brain can be regarded as a potential strategy for the delivery of siRNA sequences to the CNS.

Chapter 2

Aim of the Project

The overall aim of the project was to study the potential of TMC nanoparticles for the delivery of Rac1 siRNA in neuronal ischemic conditions, *in vitro* and *in vivo*, and to simultaneously confirm the therapeutic effect of Rac1 silencing after cytotoxic conditions characteristic of ischemia.

To attain this aim, different goals were established:

1) Evaluation of Rac1 expression by a neuronal cell line in normal and neurotoxic conditions.
2) Synthesis and characterization of TMC nanoparticles formed with double-stranded DNA sequences (siDNA) and with Rac1 siRNA sequences.
3) *In vitro* assessment of TMC nanoparticles internalization in neuronal cells.
4) Analysis of nanoparticles cytotoxicity in a neuronal cell line.
5) *In vitro* investigation of Rac1 silencing effect in a neurotoxic context.
6) *In vivo* evaluation of nanoparticles capability to reach the mice brain after intranasal administration.

Chapter 3

Experimental Methods

3.1. HT22 cell culture

HT22 cells, a mouse hippocampal neuronal cell line (a kind gift from Dave Schubert at the Salk Institute), were grown in Dulbecco's modified Eagle's medium (DMEM) with high glucose, sodium pyruvate and glutamax supplement (Gibco, Invitrogen) supplemented with 10% (v/v) fetal bovine serum (FBS) (Sigma-Aldrich), 10 U/ml penicillin and 10 µg/ml streptomycin (Gibco, Invitrogen). Cells were passed, using 0.25% (w/v) trypsin and 0.05% (w/v) EDTA, every 2 days, with a confluency of 70-90%. To promote HT22 cell differentiation, these were cultured in Neurobasal medium supplemented with 1x N-2 supplement, 2 mM L-glutamine, 10 U/ml penicillin and 10 µg/ml streptomycin (all from Gibco, Invitrogen), for 48h. Cells were differentiated in 24-well culture plates (Corning) coated with poly-D-lysine (PDL) at a density of $1x10^5$ cells/well. PDL (Sigma-Aldrich) was used at a concentration of 10 µg/ml, in borate buffer (pH 8.2). After a 30min incubation with PDL at room temperature (RT), wells were washed twice with sterile distilled water and dried out in the laminar flow chamber.

The cells were maintained at 37^{o}C in a humidified incubator with 5% (v/v) CO_2.

3.1.1. HT22 cell cytotoxic treatment

L-Glutamic acid monosodium salt hydrate (Sigma-Aldrich) and hydrogen peroxide (H_2O_2) 35% (w/w) (Sigma-Aldrich) were used to promote cellular toxicity. Stock solutions of 1 M and 0.103 M, in distilled water, were used for glutamate and H_2O_2 treatments, respectively. The chemicals were always freshly added to the cell culture medium for 4h or 24h at different concentrations.

3.2. Cell viability assays

Different cell viability assays were employed in order to study HT22 cells response to cytotoxic stimulus and TMC polyplexes cytotoxicity.

3.2.1. Resazurin assay

Resazurin assay was used as one approach to evaluate cell metabolic activity. Viable cells reduce resazurin (a blue non-fluorescent compound) to resofurin (a pink fluorescent product). As viable cells continuously convert resazurin to resofurin, it is also used as an indirect quantitative measure of cell viability [92]. For both glutamate and H_2O_2 cytotoxicity as well as TMC biocompatibility cells were seeded at a density of $3.5x10^4$ cells/well in 24-well culture plates (Corning). 24h or 42h after cell seeding, glutamate treatment was performed, during 24h or 6h, respectively. For TMC cytotoxicity, the evaluation was done 48h after cell seeding (24h after incubation with TMC polyplexes). 2h before the experiment endpoint, 10% (v/v) resazurin (from an initial stock of 0.1 mg/ml in phosphate buffered saline (PBS), Sigma-Aldrich) was added to each well and cells were incubated at 37°C in the CO_2 incubator, after which 100 µL of the medium were transferred to a black-walled 96-well plate with clear bottom (Brand GMBH) and fluorescence was measured (λ_{exc}=530nm; λ_{em}=590nm) using a spectrophotometer microplate reader (SynergyMX, Biotek). To determine background fluorescence levels, average fluorescence value correspondent to the conditioning medium of unseeded cells was measured. Results are expressed as percentage of metabolic activity of treated cells relative to untreated cells. For cytotoxicity studies, each independent experiment was done in duplicate whereas for TMC biocompatibility no duplicates were used in the different independent experiments.

3.2.2. MTT assay

Another approach that allows for the measurement of cells metabolic activity involves the reduction of 3-(4,5-dimethyl-2-thiazolyl)-2,5-diphenyl tetrazolium bromide (MTT), a yellow, water soluble salt, into an insoluble purple formazan product [92]. Cells were seeded at a density of $4.5x10^4$ cells/well in 24-well culture plates (Corning) and exposed to glutamate or H_2O_2 24h later. Following a 4h cytotoxic treatment, the wells were washed twice with PBS and medium was changed to DMEM without phenol red, with high glucose and 25 mM HEPES (Gibco, Invitrogen) supplemented with 10% FBS (Sigma-Aldrich), 1 mM sodium pyruvate, 10 U/ml penicillin, 10 µg/ml streptomycin (all from Gibco, Invitrogen) and 10% (v/v) of MTT (from an initial stock of 5mg/ml PBS, Sigma-Aldrich). Following an incubation of 3h with MTT, supernatant was discarded and formazan crystals were solubilized with dimethyl sulfoxide (DMSO) (Sigma). The plate was, then, shaken for 5min at 200 rpm and the content of each well centrifuged, at 13000 rpm for 2min. Finally, 200 µl of the supernatants were transferred to a 96-well plate (Corning) and absorbance was measured, at 540 nm with background subtraction at 690 nm, on a spectrophotometer microplate reader (SynergyMX, Biotek). Results are expressed as percentage of metabolic activity of treated cells relative to untreated cells. Each independent experiment was done in duplicate.

3.2.3. Propidium iodide and Hoechst 33342 staining

Propidium iodide (PI) (Sigma) and Hoechst 33342 (Life Techonolgies) staining was performed to evaluate cellular death. PI enters cells with damaged membranes, allowing its binding to the nucleic acids while it is excluded from healthy cells. At the end of the toxicity and/or transfection experiments, cells were incubated with 5 µg/ml Hoechst 33342 diluted in PBS for 20min at 37°C. In the last 10min of incubation, PI was added to each well to a final concentration of 3 µM. After rising twice with PBS, cells were visualized and photographed under an Inverted Fluorescence Microscope (Zeiss Axio Vert). Images were acquired with AxioCam HRc (Zeiss) and using AxioVision SE64 Rel. 4.8 software. PI and Hoechst fluorescence intensities were quantified with Fiji software.

3.2.4. Calcein and Propidium Iodide staining

Calcein AM (Invitrogen) and PI (Sigma) were also used to evaluate viability. Calcein is a membrane-permeable dye which after entering the cell is cleaved, yielding the membrane-impermeable. Apoptotic and dead cells with compromised cell membranes do not retain calcein. Cells were incubated with 4 µM calcein diluted in PBS for 20min at 37°C and PI was added in the last 10min to a final concentration of 3 µM. After rising twice with PBS cells were visualized and photographed under the Inverted Fluorescence Microscope (Zeiss Axio Vert) with the camera and software referred above.

3.3. Rac1 immunofluorescent staining

In order to evaluate the levels and sub-cellular distribution of Rac1 after a neurotoxic stimulus, immunofluorescent staining was performed on cells cultured in PDL coated glass coverslips (13 mm diameter). The PDL coating was performed as described above. Coverslips were previously cleaned with 65% nitric acid for 24h and sterilized by autoclaving. HT22 cells were seeded in 24-well culture plates (Corning) at a density of $4.5\text{x}10^4$ cells/well or at $1\text{x}10^5$ cells/well for differentiation. 24 or 48h later, in the case of differentiated cells, cells were treated with different concentrations of glutamate or H_2O_2 for 4h, after which, cells were washed and fixed in 3.7% (w/v) paraformaldehyde (PFA, Sigma) for 10 min. After washing again, cells were permeabilized with 0.1% (v/v) triton X-100 (Sigma-Aldrich) for 5min. Following washing, cells were incubated for 1h with 5% bovine serum albumin (BSA) (Sigma-Aldrich) to minimize antibody unspecific binding. Afterwards, cells were incubated with mouse monoclonal antibody against Rac1 (1:250, abcam) diluted in 1% BSA, overnight at 4ºC. Finally, cells were washed and incubated with Alexa Fluor 488-conjugated goat anti-mouse secondary antibody (1:1000, Invitrogen) diluted in 1% BSA for 1h, in the dark. After washing, cells nuclei were stained with DAPI (1:1000, Life Technologies) for 10min and cells were washed again. Coverslips were mounted with Fluoromount^{TM} Aqueous Mounting Medium (Sigma) and observed and photographed using an Inverted Fluorescence Microscope (Zeiss Axio Vert) with the camera and software already referred. All the washings and dilutions were performed with PBS and all steps carried out at RT, unless otherwise mentioned.

3.4. F-actin fluorescent staining

Phalloidin staining was performed in order to label actin filaments. Cells were cultured on acid-treated coverslips coated with PDL, as described above. At the desired time point after transfection, cells were washed with PBS, fixed and permeabilized as for Rac1 staining. Blocking was performed for 20min with 1% BSA diluted in PBS. Cells were, then, incubated with Alexa-Fluor 488 Phalloidin (1:75, Life Technologies) in 1% BSA for 20min, in the dark. At the end of the incubation cells were washed and nuclei counterstained with 1 µg/mL Hoecht 33342 diluted in PBS, for 10min. Finally, cells were washed again and coverslips were mounted as already described. Samples were observed and photographed on both Inverted Fluorescence Microscope (Zeiss Axio Vert) and Leica TCS SP5 Confocal Microscope (Leica Microsystems, Inc.) using Z-stack mode and at a resolution of 1024x1024 pixels. Every steps were done at RT and all washes with PBS.

3.5. Protein extraction and western blot

HT22 cells were seeded at a density of 2.25x10^5 cells/well in 6-well culture plates (Corning) and treated with glutamate or H_2O_2, 24h after seeding. After a 4h treatment, cells were washed with PBS and harvested with RIPA lysis buffer (25mM Tris-Hcl pH 7.6, 150 mM NaCl, 5 mM EDTA, 1% (v/v) NP40) containing protease inhibitors cocktail (1:100, Thermo Scientific) freshly added to the lysis buffer. Samples were, then, incubated for 15min at 4ºC, after which 29G needles or sonication (Bioruptor, Diagenode) were used to help on the disruption and homogenization of cells. For sonication, 5 cycles (30 seconds on/ 30 seconds off) were used in the high position. After homogenization, samples were centrifuged for 15min at 14000 rpm (4ºC) and supernatants were kept at -20ºC until use.

Quantification of total protein was determined by bicinchoninic acid (BCA) protein assay (Pierce). Briefly, protein samples were diluted (1:5) in RIPA buffer with freshly added proteases inhibitor cocktail (1:100) and incubated with BCA working reagent for 30min at 37ºC, protected from light. After incubation, absorbance was measured at 562 nm using a spectrophotometer microplate reader (SynergyMX, Biotek) and protein concentration was calculated using a standard curve with BSA samples in a concentration ranging from 0 to 2 µg/ml. For western blot analysis, 20 µg of total protein in RIPA buffer and 1x LDS sample buffer (Novex, Invitrogen) with 2.5% β-mercaptoethanol were denatured through boiling at 95ºC for 5min. The resulting samples were subjected to denaturing 12% sodium dodecyl sulphate (SDS) polyacrylamide gel electrophoresis (Acrylamide from BioRad). A 4% SDS polyacrylamide gel was used as stacking gel and electrophoresis was performed at 80V until samples reached the 12% resolving gel, from which electrophoresis was carried out at 120V. Proteins were, then, transferred onto a nitrocellulose membrane (Novex, Invitrogen) using the iBlot 2 Dry Blotting System (Life Tecnhologies). Increasing voltages were employed for the western blot: 20V for 1min, 23V for 4min and 25V for 2min. After the transfer of the proteins, Ponceau S at 0.1 % (w/v) in 5% (w/v) acetic acid (Sigma) was used in order to visualize the transfer of protein bands. The membrane was then blocked, in 7.5% (w/v) non-fat skim milk in PBS containing 0.05% Tween 20 (VWR) (PBS-T), for 1h at RT. After blocking, membranes were incubated with primary monoclonal mouse antibodies, specific for Rac1 (1:2000, abcam) or β-actin (1:15000, Sigma-Aldrich), diluted in 2.5% milk (in PBS-T), overnight at 4ºC. On the next day, the membrane was washed 3 times for 10min in PBS-T, followed by an incubation of 1h at RT with the goat anti-mouse horse raddish peroxidase-conjugated secondary antibody (1:10000, Santa Cruz Biotechnology). After 2 washes with PBS-T and one last wash with PBS (10 min, RT), protein-antibody complex was detected with ECL detection reagent (Amersham, GE Healthcare) using the ChemiDoc™ MP System (BioRad). Quantification of the western blots was performed using the Fiji software.

3.6. TMC-siDNA/siRNA polyplexes synthesis and characterization

Trimethyl Chitosan

TMC (Kytozyme, lot VIHA0013-157) was purified and characterized by Carla Gomes (nBTT, i3S). Purification was made by filtration and dialysis, as previously described [93]. Briefly, TMC was dissolved in 5 mM HCl solution at a final concentration of 0.5 % (w/v), filtered through a sintered glass filter (pore size from 100 to 160 µm, Duncan), dialyzed for 3 days against deionized water and collected after freeze-drying at -80ºC for 72h (Labconco). Characterization was performed by gel permeation chromatography (GPC) and by proton nuclear magnetic resonance

(1H-NMR). GPC allowed to determine the polymer M_w which was 43.3 ± 5.5 kDa, with a polydispersity index (Mw/Mn) of 2.2 ± 0.8. 1H-NMR evaluated polymer degree of acetylation (DA) and TMC DQ. The % of DA was calculated according to Mourya et al. [78] and was found to be 11%. The % of DQ was calculated following the equation reported by Curti and Campana-Filho [94] and was found to be 30% .

TMC modified with 6-Carboxy-X-rhodamine N-succinimidyl ester (Santa Cruz Biotechnology) (TMC_{ROX}) and thiolated TMC (TMC_{SH}) made by Carla Gomes were also used. TMC_{ROX} was synthetized by dissolving rhodamine reagent in methanol at a final ratio of 1:1 H_2O:methanol. The ROX solution was, then, added to the TMC in a NH_2:ROX ratio of 7.4:1. The reaction was set up for 3h at RT, under continuous stirring. The resulting polymer conjugate was purified as described above. For TMC_{SH} synthesis, polymer was dissolved in 20 mM HEPES buffer at 5 mg/ml and 2-iminothiolane HCl (Sigma-Aldrich) was added to the polymer solution, in order to attain a theoretical modification of 10 % of the polymer amine groups. The pH of the solution was then adjusted to 8 and solution was incubated for 6h in an inert atmosphere (argon), at RT, under stirring. Afterwards, 100 mM DL-Dithiothreitol (Sigma-Aldrich) was added to reduce any disulfide bonds, and the solution was stirred for another hour. The resulting polymer conjugates were ultrafiltrated using a 10 kDa membrane against 5 mM HCl at 4°C. Thereafter samples were frozen at -80°C and lyophilised for 3 days. The resulting powders were stored at -20°C until further use. The percentage of polymer thiolation was quantified using Ellman's Reagent (DTNB). The amount of free thiol moieties in the polymer was determined using cysteine standards. The degree of thiolation was calculated using the estimated average M_w per glucosamine unit and was found to be 4.9 ± 0.2%.

TMC and TMC_{ROX} were dried out in a vacuum oven (Raypa) for 24h at 60°C to remove any residual water left after lyophilisation process. These polymers were dissolved in 5 mM HCl overnight under stirring at RT and then in HEPES/glucose (both from Sigma) (pH 7.4) in order to have a final buffer concentration of 20 mM HEPES/5% (w/v) glucose and a polymer concentration of 3 mg/ml. After HEPES/glucose buffer addition, the solution was incubated for additional 4h with agitation to complete the dissolution procedure. TMC_{SH} was dissolved in a similar manner, however it was not dried neither let under stirring overnight to avoid disulphide bonds formation between thiol groups. After dissolution, polymers were filtered with 0.22 µm pore sized filter unit (Millex-GP, Millipore) in the flow chamber, to guarantee polymer sterility for *in vitro* studies and polymer concentration was corrected by using Cibacron Brilliant Red (CBR) (Sigma-Aldrich). The method is based on the electrostatic interactions of the anionic CBR molecule with the cationic polymer, which originate a shift of CBR absorbance at 575 nm when in a complexed state [95]. Briefly, polymer solutions were incubated with CBR (0.75 µg/ml, pH

9) for 20min at RT under agitation (800 rpm, Thermomixer). Absorbance was then recorded at 575 nm using a spectrophotometer microplate reader (SynergyMX, Biotek). A calibration curve was made using serial dilutions of the unfiltered polymer sample, allowing the determination of filtered polymer concentration.

“Small interfering” DNA

Two complementary DNA sequences (sense and anti-sense) were designed to replace the use of the real siRNA in initial experiments which we named small interfering DNA (siDNA). These sequences did not have any known biological function (sequences shown in Table S 1). The aim of these sequences was to optimize nanoparticle formation with TMC, transfection conditions and *in vivo* administration procedures. The best ratio for siDNA single-stranded sense and anti-sense sequences annealing was determined through a 12% polyacrylamide gel electrophoresis (Figure S 1 shows a representative result of these gels) every time new sequences were prepared. Annealing was performed to final concentrations of 20 µM or 40 µM by mixing both strands in the presence of the annealing buffer (100 mM Potassium Acetate; 30 mM HEPES), followed by incubation at 94^{o}C for 5min. Annealed sequences were then let at RT for 30min before being frozen at -20^{o}C. Cy5-labeled siDNA (siDNA$_{cy5}$) was also used for fluorescence microscopy and flow cytometry studies. All siDNA sequences were ordered from Integrated DNA technologies (IDT) with HPLC purification.

Small interfering RNA

siRNA sequences were selected in order to specifically silence Rac1 mRNA (sequences on Table S 1). As control for transfection experiments, a silencer negative control (21 base pairs) siRNA without significant specificity was used. For fluorescence microscopy and flow cytometry, a FAM-labeled silencer negative control siRNA (siRNA$_{FAM}$) was used. All siRNA sequences were obtained from Ambion with HPLC purification.

3.6.1. Synthesis

Polyplexes can be formed through electrostatic interaction between the positively charged TMC polymer and the negatively charged nucleotide sequences (Figure 9A). In the present work, complexes were formed using Na_2SO_4 as a coacervation agent, which contributes to particle formation through a mechanism of ionic cross-linking while also acting as a desolvating agent that, by facilitating the removal of water molecules from polymer chains, increases intramolecular hydrophobic interactions [80,93]. Thus, TMC and siDNA/siRNA sequences were mixed in equal volumes of polymer and sequences, diluted in buffer (20 mM

HEPES, 5% (w/v) glucose, pH 7.4) supplemented with 50 mM Na_2SO_4. Polymer solutions and sequence master mixes (MM) were heated at 40°C for 5min in separate (Figure 9B I) before adding the sequence solution to the polymers, dropwise under vortex (Figure 9B II). The resulting mixture was incubated at 40°C for 10min under agitation (1000 rpm, Thermomixer) (Figure 9B III) and complexes were then allowed to stabilize, for at 30min at RT, before use (Figure 9B IV). These conditions were optimized by Marisa Assunção under the supervision of Isabel Amaral (nBTT, i3S). Complexes with different molar ratios of trimethylated amine groups (N) to siDNA/siRNA phosphate groups (P) - N/P molar ratio − were prepared. Unless otherwise stated, a final concentration of 12.5 µg/ml of siDNA/siRNA was used in polyplexes formation. For siRNA complexes synthesis, DEPC-treated water was used for buffers preparation in order to remove RNAses. For DEPC-water treatment, 0.1% DEPC was added to MiliQ water and mixed thoroughly. The mix was incubated for 2h at 37°C and then autoclaved for 15min in order to remove all traces of DEPC.

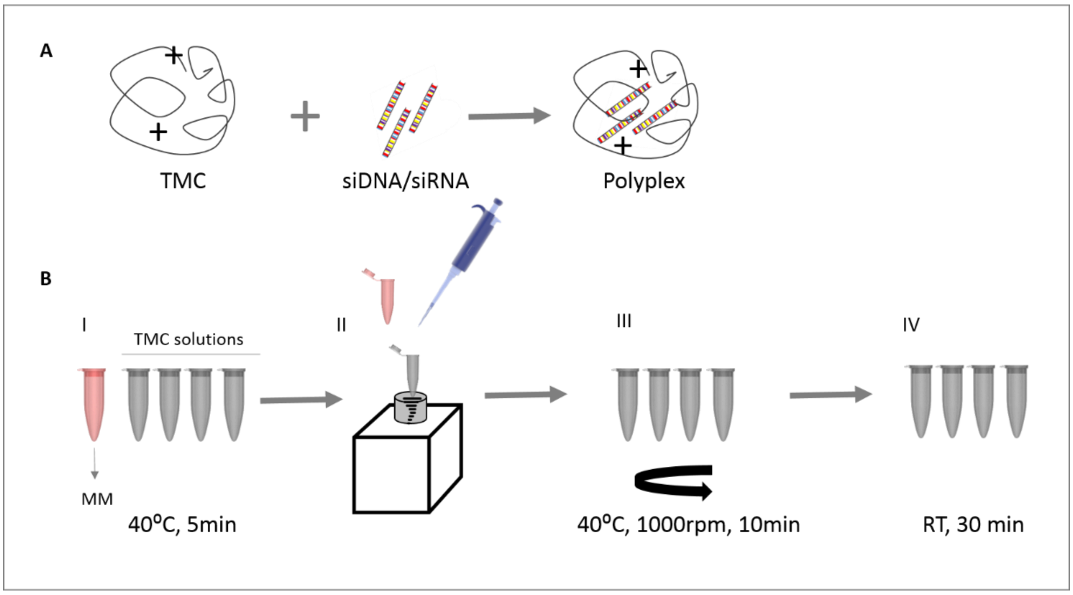

Figure 9 Polyplexes synthesis. (A) Schematic representation of the complexes formation. (B) Scheme of the experimental procedure to synthetize the polyplexes: I) TMC and sequences are heated; II) sequences are added to the TMC solution under vortex; III) the resulting mix is agitated; IV) mixes are, ultimately, incubated at RT.

3.6.2. Dynamic and Electrophoretic Light Scattering

Dynamic light Ssattering (DLS) at an angle of 173° was used for the determination of the mean hydrodynamic diameter and PDI of polyplexes while electrophoretic light scattering was used for the complexes zeta potential determination. Both were measured with Zetasizer Nano ZS equipment (Malvern). The Smoluchowski model was applied for zeta potential determination and cumulant analysis was used for mean particle size determination. Hydrodynamic diameter and PDI measurements of siDNA-TMC polyplexes were made in disposable plastic micro cuvettes (ZEN0040, Malvern) with undiluted samples whereas zeta potential measurements were performed in disposable folded capillary cells (DTS1070, Malvern) with 6-fold diluted samples. For TMC-siRNA polyplexes 6-fold diluted samples were used for all the measurements. All measurements were performed in triplicate at 25°C.

3.6.3. Gel Retardation Assay

The interaction strength and complexation efficiency of TMC-siDNA/siRNA sequences were determined by gel retardation assay using polyacrylamide gel (12%, acrylamide from BioRad). 4% polyacrylamide gel was used as stacking and electrophoresis was performed at 100V for 1h. 100 ng of siDNA or siRNA were loaded in each well, either complexed with TMC at different N/P ratios, either alone, in a total volume of 15 µl with 1x nucleic loading buffer. The gels were stained with SYBR Gold nucleic acid stain (Molecular Probes, Invitrogen), diluted in Tris/borate/EDTA (TBE) buffer (1:15000), for 10min and visualized using Gel Doc XR imager (BioRad).

The assay was performed 0 and 1d following complexes formation and particles were stored at 4ºC.

3.6.4. RNAse protection assay

Protection of TMC against siRNA degradation from ribonucleases (RNases) was assessed by a gel retardation assay after siRNA polyplexes exposure to RNase A (NZYtech). In brief, the TMC-siRNA N/P 8 was incubated with 0.53 µg of RNase A (0.53 µg per µg of siRNA) at 37^{o}C for different time periods (0, 0.5, 1, 2 and 4h). As a control, an equal amount of free siRNA was also incubated with RNase A for the same time periods. After the incubation, samples were subjected to RNase A inactivation with 0.09 M EDTA, for 5min. Samples were then mixed with 0.45% (v/v) SDS to allow sequences dissociation from TMC. Finally, samples were analysed by electrophoresis as described in the gel retardation assay (Figure 10 illustrates the assay). Obtained bands were quantified with the Fiji software.

Of note, the above described protocol is the result of an optimization of the experimental procedures and RNase and SDS concentrations required for the assay.

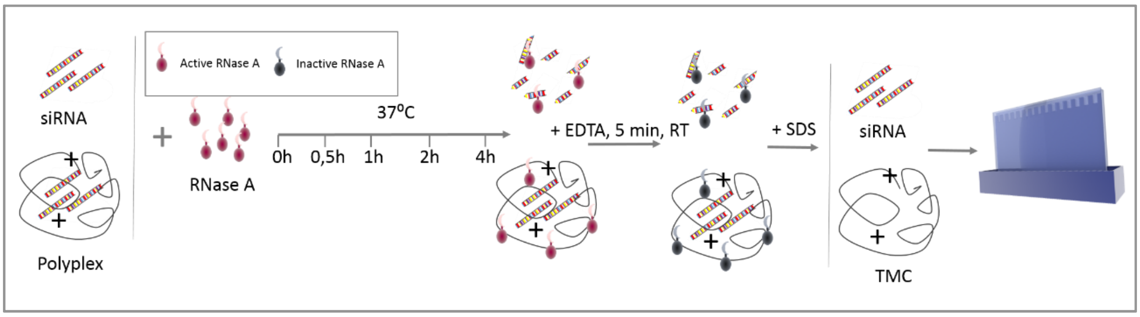

Figure 10 Scheme of the different experimental steps to assess polyplexes capacity to protect RNA sequences from RNase degradation. Complexes and free siRNA were incubated with RNase for different time periods, after which the enzyme was inactivated with EDTA. Both free siRNA sequences and complexes were then treated with SDS, which allowed sequences dissociation from the complex, and samples were loaded onto a polyacrylamide gel.

3.7. Transfections

Cells were plated at a density of $3.5\text{x}10^4$ cells/well in 24-well culture plates (Corning) 24h prior to transfection so that cells would have a confluence of about 70% at the time of transfection. For differentiated HT22 cells, culture conditions were as already referred. TMC-siDNA or TMC-siRNA polyplexes were synthetized as described above. Afterwards, TMC polyplexes were added, dropwise while gently mixing the plate, in serum-free culture conditions to a final siRNA concentration of 200nM (50 and 100nM concentration were also used for optimization studies) of siDNA/siRNA. As a positive control, lipofectamine 2000 (Invitrogen) was used following the manufacturer's protocols. Briefly, equal volumes of sequences and lipofectamine diluted in culture medium without FBS were mixed and incubated for 5min at RT. A volume of 100µl lipoplexes was then added dropwise to each well to the desirable final siDNA/siRNA concentration. A ratio of 1.5 (mass of lipofectamine to mass of siDNA/siRNA) was used in all the experiments. For the qPCR experiments a ratio of 3 was additionally tested. To the non-treated control wells, 20 mM HEPES/5% (w/v) glucose buffer was added. A final volume of 400 µl was used per well. 4h after transfection, 10% FBS (Sigma- Aldrich) was added to each well. Cells were incubated with the complexes for 24h, unless otherwise mentioned.

3.8. Polyplexes association and internalization analysis

As already stated, cy5-labeled siDNA ($\text{siDNA}_{\text{cy5}}$), FAM-labeled siRNA ($\text{siRNA}_{\text{FAM}}$) were used to study nanocomplexes cellular association and uptake. Studies with the rhodamine-labeled TMC_{ROX} were also performed with the same aim. Complexes were synthetized for these experiments as mentioned above.

3.8.1. Flow cytometry studies

After 24h of polyplexes incubation, cells were washed with PBS, collected through trypsinization and with the aid of cell scrappers and washed again with PBS. Cells were then ressuspended in PBS and filtered with 35-50 µm filter to remove any cell clump for fluorescent activating cell sorting (FACS) analysis in a BD Calibur flow cytometer (Becton Dickinson). Nontransfected cells, cells treated with uncomplexed TMC and cells transfected with TMC complexed with non-fluorescent sequences were used as negative controls. For each sample, 10000 events were counted and data was analysed using Flow Jo 10.07 software (TreeStar Inc).

3.8.2. Imaging studies

For imaging studies, cells were cultured on acid-treated coverslips coated with PDL. After a 24h or 4h (when stated) incubation with the nanocomplexes, cells were fixed with 3.7% (w/v) PFA (Sigma) as already described. After washing with PBS nuclei were counterstained with DAPI (1:1000, Life Technologies) for 10min and cells were washed again. Coverslips were then mounted with Fluoromount^{TM} Aquous Mounting Medium (Sigma) and samples were observed and photographed on both the Inverted Fluorescence Microscope (Zeiss Axio Vert) and Leica TCS SP5 Confocal Microscope (Leica Microsystems, Inc.). Confocal pictures were taken using Z-stack mode and at a resolution of 1024x1024 pixels.

3.9. RNA extraction and Real Time quantitative Reverse Transcriptase-Polymerase Chain Reaction

Real time quantitative Polymerase Chain Reaction (RT-qPCR) was used to evaluate Rac1 gene expression following transfection with TMC-siRNA nanocomplexes. Cells were plated as described on the "transfections" section (3.7) and incubated for 24h with TMC-siRNA complexes. After incubation, cells were treated with 6 mU of *Streptomyces sp.* Chitosanase (Merck Millipore) per µg of TMC for 1h at 37^{o}C. Chitosanase was diluted in DMEM glutamax (pH 6.3) and was used to overcome possible issues related to the yield and integrity of the extracted RNA [79]. Following Chitosanse treatment, 150 µL of RNA lysis buffer (Zymo Research) was added to each duplicate. The sample homogenate from each duplicate was combined and RNA purification was carried out with Quick-RNA™ MicroPrep (Zymo Research) according to manufacturer's instructions. All the centrifugation steps of the purification protocol were performed at 12000 g and RNA elution was made in 2 steps to a final elution volume of 14 µl. Briefly, 7 µl of nuclease-free water (Ambion) were directly added to the column matrix and incubated for 5min at RT before centrifugation at maximum speed. Next, this step was repeated and RNA samples were analyzed on Nanodrop ND 1000 for concentration and purity determination. Extracted RNA samples were further analysed in experion (BioRad) to evaluate RNA integrity (Figure S 2). RNA samples were stored at -20ºC until complementary DNA (cDNA) synthesis and then at -80ºC, for longer storage periods.

A total of 1.85 µg of RNA per sample was used for the synthesis of cDNA with the NZY First Strand Synthesis Kit (NZYtech). Reverse Transcriptase Polymerase Chain Reaction (RT-PCR) was performed in a Thermocycler (Core Life Sciences) using manufacturer's instructions. cDNA samples were then kept at -20ºC.

RT-qPCR was performed using 2 µl of cDNA (diluted 1:20) as a template plus the specific primer pairs (to a final concentration of 125nM) and 10 ul of iTaq™ DNA polymerase (BioRad) in a final reaction volume of 20 µl. iTaq mix used was composed of dNTPs, iTaq DNA Polymerase, qPCR buffer solution and $MgCl_2$. The cycling conditions used were the following: initial cDNA denaturation at 95ºC for 3min; 40 cycles of 1) cDNA denaturation at 95ºC for 15s, 2) annealing at 57ºC for 20s and 3) extension at 72ºC for 15s.

For housekeeping primer selection, four housekeeping genes were tested (Hypoxanthine-guanine phosphoribosyltransferase, ID: NM_013556.2; Glyceraldehyde 3-phosphate dehydrogenase, ID: NM_008084; Phosphoglycerate kinase 1; ID: NM_008828.2; Cyclophilin, ID: NM_008907.1) for primer efficiency and expression levels variance when comparing transfected with non-transfected samples. Primer efficiency of Rac1 and housekeeping primers was assessed by a linear regression of the comparative threshold (CT) values of a cDNA template serial dilution and primers were considered efficient with efficiency values of 80-105%. Having in account these parameters, cyclophilin was chosen as housekeeping gene for further studies. Thus, for data analysis, the CT cycle values of cyclophilin were used to normalize loading variations. The expression fold difference was calculated according to Eq.1.

$$\text{mRNA relative Expression} = 2^{(CThousekeeping - CTtarget)} \qquad \text{(Eq. 1)}$$

qPCR products were analysed using the iQ5 software 2.1 (BioRad). Primer sequences used are summarized on Table S 2.

3.10. In vivo studies

To study TMC nanoparticles capability to reach the brain tissue through intranasal administration, nanocomplexes distribution within the tissue and potential toxic effects on other organs, were assessed through *in vivo* studies on mice.

All animal experiments were approved by the local animal ethics committee at the Instituto de de Investigação e Inovação em Saúde (i3S) and by Portuguese official authority on animal welfare and experimentation (Direção Geral de Alimentação e Veterinária) in accordance with the National and European Union rules. The experimental protocol was carried out taking into account the Russel and Burch 3R's principle. Mice used throughout the experiments were housed at the i3S animal house under 12h light/dark cycle in specific pathogen-free conditions and with regular rodent's chow and tap water *ad libitum*.

3.10.1. Nanoparticles preparation

For *in vivo* studies, TMC-siDNA nanocomplexes preparation was performed as already described with an additional step to concentrate nanoparticles (described below) enabling the intranasal administration of a low volume of nanoparticle solution.

For each mouse, 15 µg of siDNA were intranasally administered. Two different approaches were used for complexes synthesis: 1) normal synthesis (siDNA at 12.5 µg/ml) and 2) "high concentration" synthesis (siDNA at 50 µg/ml) in 4 times less volume (Figure 11A).

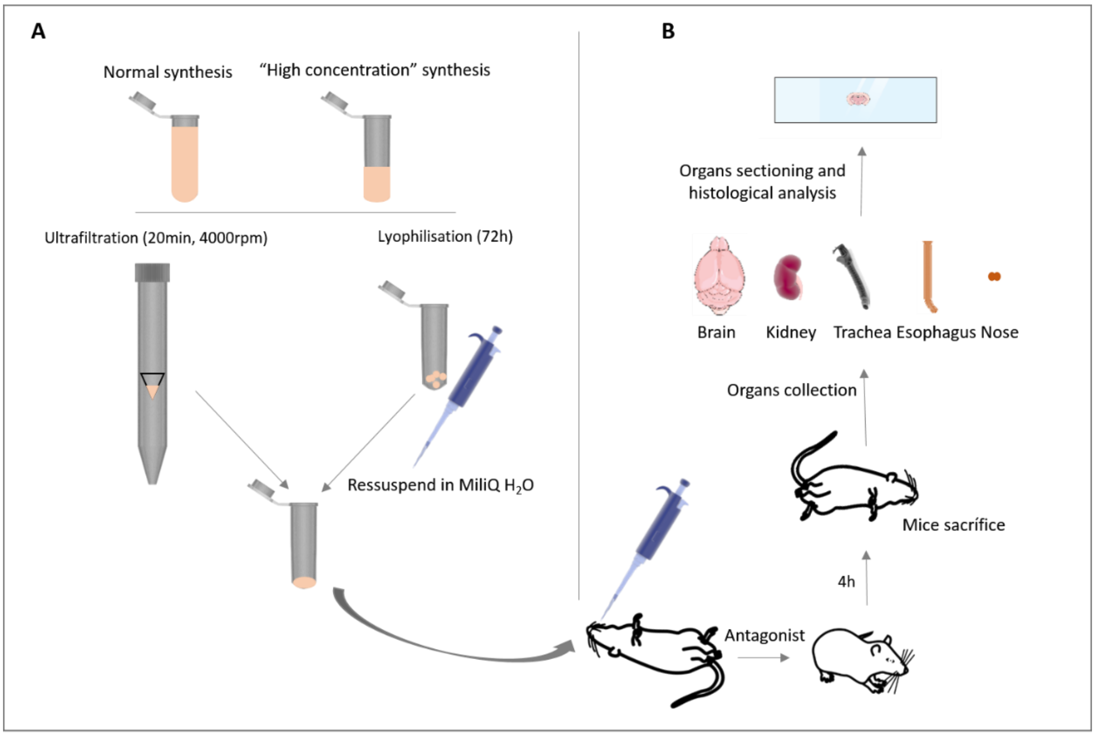
A
Normal synthesis
"High concentration" synthesis
Ultrafiltration (20min, 4000rpm)
Lyophilisation (72h)
Ressuspend in MiliQ H2O
B
Organs sectioning and histological analysis
Brain
Kidney
Trachea
Esophagus
Nose
Organs collection
Mice sacrifice
4h
Antagonist

Figure 11 *In vivo* studies. (A) Scheme of the nanoparticles synthesis process for *in vivo* administration. Particles were synthetized in normal and "high concentration" conditions and concentrated through ultrafiltration or lyophilisation. (B) Schematic representation of the animal experimental procedures. Nanoparticles were intranasally administered to anesthetized mice and antagonist was administered. 4h after mice were sacrificed and organs were collected for histological analysis.

For nanoparticles concentration two different approaches were also used: lyophilisation (freeze-drying) and ultrafiltration (Figure 11A). Lyophilisation was performed for 72h at -80ºC (Labconco), followed by nanoparticles resuspension in 40 µl miliQ water to a final siDNA concentration of approximately 375 µg/ml. Ressuspended nanoparticles were mixed with orbital shaking for 30min and administered to animals. For ultrafiltration, a 10KDa cutoff centrifugal filter concentrator (GE Healthcare) was used and centrifugation was performed for 20min at 4000 rpm. A final siDNA concentration of approximately 250 µg/ml was achieved.

Later studies were made with PEGylated-TMC nanocomplexes. For that, TMC_{SH} was used. First, TMC_{SH} was complexed with $siDNA_{cy5}$ as already described but with changes: 1) all the steps were performed at RT and thus there was no previous heating of the solutions; 2) after synthesis, nanoparticles were stabilized at RT for 10min. Afterwards, methoxypolyethylene glycol maleimide (PEG-maleimide, 5KDa, Sigma) diluted in miliQ water (2 mg/ml) was added to the nanocomplexes in different final concentrations. Briefly, 2 different PEG-maleimide final concentrations were tested in order to promote maleimide reaction with 25 or 75% of the TMC thiol moieties, which were quantified by the Ellman's assay and found to be 4.9%. After PEG-maleimide addition, nanocomplexes were incubate for 2h at 37ºC with agitation (800rpm) to allow TMC PEGylation. These studies were performed with N/P 8 nanocomplex formulation. Nevertheless, characterization studies (through DLS) were also performed with the N/P ratio 4.

3.10.2. Nanoparticles administration

C157/BL6 mice (aging between 2.5 and 6 months) were anesthetized with an intraperitoneal (i.p.) injection of 1 mg/kg Medetomidine and 75 mg/kg Ketamina. If needed, isofluorane was used by inhalation. Once the animals were completely sedated, mice were held maintaining animal head on the horizontal position and 10 µl or 15 µl of nanocomplexes solution were administered in each nostril with a pipette (P20) and thin gel loading tips (Figure 11B). Mice were then kept on their backs on a heating pad for 10min and a second dose of the the same volume of nanocomplexes was again administered in each nostril. After 10 additional minutes with mice held upwards, atipamezol (antagonist) 1 mg/kg was intraperitoneally administered (Figure 11B). As control, carboxylate-modified fluorescent microspheres (fluoespheres, ThermoFisher Scientific), with 0.2 µm diameter, were intranasally or intravascularly administered. For intranasal administration, 2.5 µl of 2% (w/v) fluospheres suspension were administered in each nostril whereas for intravascular administration 100 µl of 0.4% (w/v) fluospheres suspension diluted in 0.9% Nacl sterile saline solution were delivered using a 27G needle through mice tail vein. All *in vivo* experiments were performed by PhD Sofia Duque Santos.

4h after administration, mice were sacrificed with pentobarbital (50 mg/kg) by i.p. injection and transcardially perfused with 20ml PBS followed by 30 ml 4% paraformaldehyde in PBS. Brain, kidney and, when stated, esophagus, trachea and nose were isolated (Figure 11B) and fixed for an additional hour with 4% paraformaldehyde in PBS.

3.10.3. Tissue processing and analysis

After fixation, organs were transferred to 30% sucrose in PBS at and kept at 4ºC for 1-2 days to allow for tissue impregnation. Impregnated tissue was frozen down with optimum cutting temperature (OCT) formulation (NEG50, Richard Allan Scientific) in dry ice. Tissues were sectioned with 20 µm thickness on a Micron HM 550 cryostat (Thermo Fisher Scientific) (Figure 11B), at a cabinet temperature of -20ºC, and placed on 1% (w/v) gelatine-coated microscope glass slides (WWR International). For slides gelatine coating, gelatine was firstly dissolved in H_2O at 50ºC with stirring to a final concentration of 4% (w/v). Water and chromium potassium sulfate dodecahydrate (Sigma-Aldrich) were then added to a final concentration of 1% (w/v) gelatine and of 0.05% (w/v) chromium potassium sulfate dodecahydrate. Chromium potassium sulfate dodecahydrate is used to positively charge the slides allowing them to attract negatively charged tissue sections. After 15s stirring, the solution was filtered through Whatman no 1 filter. Slides were immersed for 1min in one box filled with freshly prepared gelatine solution and for another minute in other. Finally, slides were dried overnight at 37ºC.

Tissue slides were stored at -20ºC until analysis. Slides were thawed for 30min at RT and tissue slices surrounded with Dako Pen. Afterwards, tissue slides were immersed in PBS for 10min and nuclei were counterstained with DAPI (1:1000, Life Technologies) for 15min. Slides were, then, washed twice in PBS for 10min and mounted with Fluoromount™ Aqueous Mounting Medium (Sigma). Analysis and imaging was performed using an Inverted Fluorescence Microscope (Zeiss Axio Vert) with the previously referred camera and software.

3.10.4. Tissue homogenates

In order to quantify nanoparticles in the brain using the fluorimeter, the brain cortex, OB, esophagus, trachea, kidney and nose were collected 1 and 4h following fluospheres (Molecular Probes, Invitrogen) intranasal administration. Administration was performed as already described and mice were sacrificed through 50 mg/kg pentobarbital i.p. administration, followed by cervical distension. Tissues were weighted and homogenized in lysis buffer (1 mM EDTA, 0.05% Triton X-100, 0.1% Tween80, 2 M NaCl, and 0.1 M Tris-HCl) using a manual glass teflon dounce homogenizer. 300µl of lysis buffer were used for kidney and cortex, while 150µl of buffer was used for the remaining organs. After homogenization, samples were centrifuged at 4^{o}C for 30min at 12000 rpm. The fluorescence intensity of Red fluoresopheres in the different tissues was detected using a microplate reader (SynergyMX, Biotek). 100 µL of tissue supernatants were transferred to a black-walled 96-well plate with clear bottom (Brand GMBH) and fluorescence was measured (λexc=580nm; λem=605nm).

The amount of Red fluospheres in the selected tissues was calculated by relating fluorescence intensity to a standard curve and expressing the values obtained as the milligrams of fluospheres per gram of tissue.

3.11. Statistical Analysis

Standard deviation (SD) was used to reflect the variation of the replicate determinations. Comparison between two groups was analyzed by paired Student's t-test, unless otherwise stated, using GraphPad Prism version 6.01 for Windows, GraphPad Software, La Jolla California USA, www.graphpad.com. Differences were considered significant at $p < 0.05$.

Chapter 4

Results and Discussion

4.1. Rac1 expression in the HT22 cell line in a neurotoxic context

4.1.1. HT22 response to a neurotoxic stimulus

After a neuropathological stimuli, such as in brain ischemia, glutamate is excessively released, which leads to excitotoxicity [1,6]. Moreover, the overload of Ca^{2+} in the cellular cytoplasm, caused by glutamate receptors over-activation, leads to the generation of ROS due to the activation of enzymes and to mitochondria alterations [5,6]. Thus, glutamate is also involved in the oxidative stress characteristic of an ischemic episode.

Glutamate effect on HT22 cell viability was evaluated by the resazurin assay, after cells treatment for 6 and 24h (Figure 12A). Cells exposure to glutamate for 6h did not exert any effect on viability. On the other hand, a reduction on cellular viability with increasing concentrations of glutamate was observed for the 24h time exposure. For a concentration of 16 mM glutamate, a reduction of about 90% on the cellular viability was verified while with 8 mM a tendency for a reduction on cell viability was obtained, with values of approximately 40%. The effect of different glutamate concentrations on the induction of cell death after a 24h exposure was also verified by cellular morphology (Figure 12B). The morphological changes occurring in these cells were evident with increasing glutamate concentrations. An increase on detached and degenerated cells was verified, the latter event more evident for the 16 mM concentration. Furthermore, while in untreated (control) cells and 4mM condition cellular extensions could be seen, the increase on glutamate concentration led to the appearance of damaged and rounded cells without cellular processes. It was, thus, shown herein that HT22 cells respond to glutamate toxicity in a concentration-dependent manner following a 24h treatment. Notoriously, high levels of glutamate (mM) were required to induce oxidative stress in HT22 cells, which is in accordance with previous reports [96,97]. This toxicity is evoked by inhibition of glutathione formation, leading to a reduced ability to protect against ROS accumulation [96-98]. Although the results from 24h exposure revealed a cellular response to glutamate, as reported by others [96,97], a reduction on cellular viability was not seen for the shorter time exposure studied.

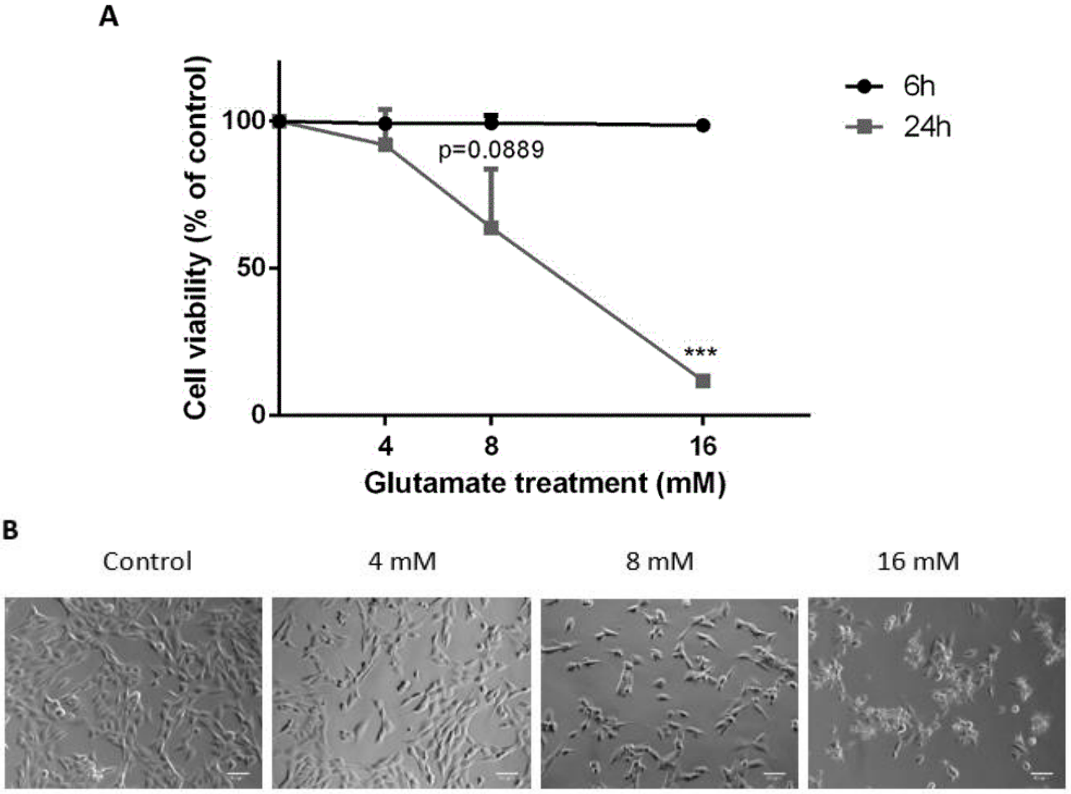

Figure 12 Effect of glutamate toxicity on HT22 cells. (A) Cell viability, through resazurin assay, following exposure to different glutamate concentrations for 6 and 24h. Results are normalized to the viability of control (non-treated) cells. (n=2 for 6h and n=3 for 24h) ***$p<0.001$, relative to control (B) Phase contrast images of cells after 24h treatment with different glutamate concentrations. Control=untreated cells. Scale bar is 60µm.

Since our following aim was to use this cytotoxic stimulus in cells previously transfected with siRNA, a short period of toxicity was desirable in order to avoid a long experimental set-up and concomitantly overconfluence. To achieve this goal a different approach was investigated, which adopted a higher concentration of glutamate and an additional condition for the toxic stimulus using H_2O_2 instead. H_2O_2 is a common mediator of neuronal oxidative stress in the ischemic brain [6,99,100] and, thus, represents a possible alternative to glutamate. Although its action mechanism is not as well studied as for glutamate, it has also been used *in vitro* to mimic stress conditions of neuropathological disorders, as brain ischemia [99,100].

To evaluate cellular viability, 4h after treatment with glutamate or H_2O_2, MTT assay was employed. No important alterations were verified for glutamate exposure, even for the highest concentration tested (Figure 13A). Although a statistical significant difference was seen for the first concentration (8 mM), the verified reduction on viability was only 4%, which is a minor decrease, not enough for our following purposes where a higher decrease was desirable. Thus, with this data it was concluded that cells treatment with glutamate for short time periods did not induce a reduction on cellular viability, even with higher concentration than what is reported on literature for HT22 cells [96,98]. Furthermore, MTT results were in accordance with what was obtained with resazurin (Figure 12A). Evaluation of HT22 cell viability after H_2O_2 treatment revealed a concentration-dependent reduction on cell viability for the higher concentrations tested (Figure 13B). Again, a significant decrease on cellular viability was verified for the least concentrated condition (50 µM). Nevertheless, the decrease observed was only 7% and therefore a very small difference to be adopted in the following experiments. For a concentration of 600 µM, a reduction of 25% in cellular viability was obtained, which suggests this condition as the most promising approach to evaluate cellular rescue after *in vitro* therapy application with Rac1 siRNA. In order to analyse this therapeutic target in our neuronal cellular line, studies on Rac1 protein expression on a neurotoxic context were next performed.

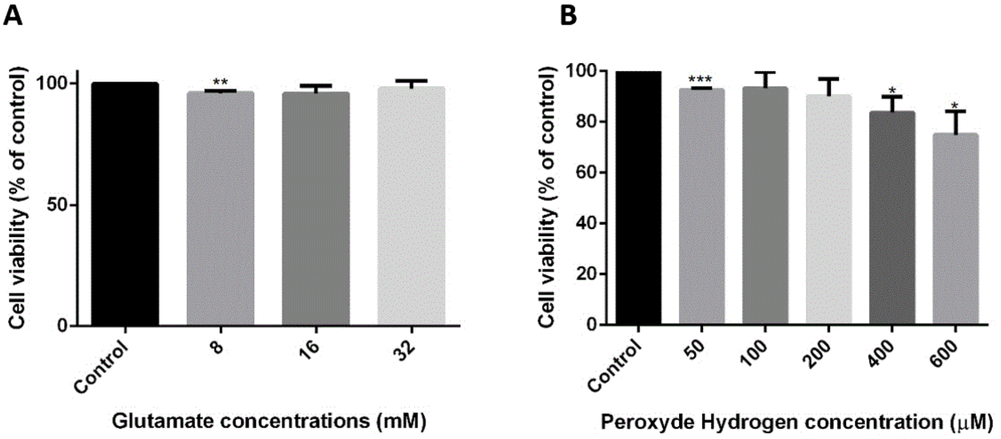

Figure 13 HT22 cells viability, through MTT assay, following a 4h neurotoxic stimulus. (A) Cells treated with different glutamate concentrations (n=4). (B) Cells treated with different H_2O_2 concentrations (n=4). Results are normalized to the cell viability of the control (non-treated) cells. *p<0.05 **p<0.01 ***p<0.001 (relative to the control).

4.1.2. HT22 Rac1 expression after a neurotoxic stimulus

Once evaluated the decrease in HT22 cellular viability after a neurotoxic stimulus, Rac1 protein expression levels were assessed in the same conditions. Cells were treated with increasing concentrations of glutamate or H_2O_2 for 4h, after which Rac1 protein expression levels were evaluated. A significant increase on Rac1 expression was seen for the higher concentrations of glutamate (Figure 14A). It was also interesting to observe that the use of a higher concentration (32 mM) was not translated in a further increase on the protein levels. Additionally, it was verified that although these glutamate concentrations did not interfere with HT22 cellular viability, they contributed to an increase on Rac1 expression meaning that these changes precede ischemic neuronal cell death. When cells were exposed to different H_2O_2 concentrations, Rac1 levels tended to augment as a function of H_2O_2 concentration (Figure 14B).

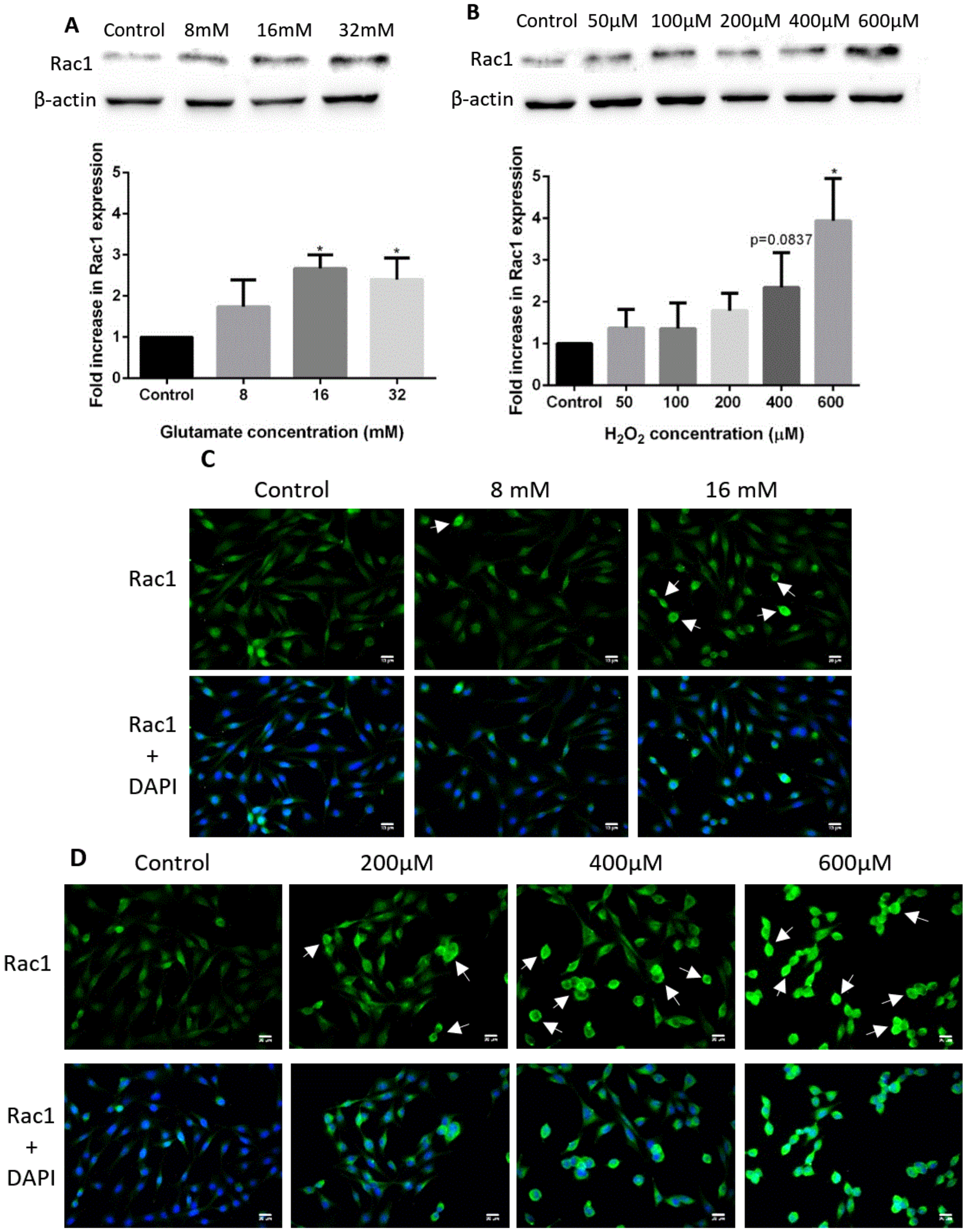

Figure 14 Rac1 expression in HT22 cells after 4h treatment with different concentrations of glutamate or H_2O_2. (A) Fold increase in Rac1 expression levels, relative to control untreated cells, after treatment with glutamate (normalized to β-actin). Representative bands from 3 independent experiments (n=3) $*p<0.05$, relative to control. (B) Fold increase in Rac1 expression levels, relative to control untreated cells, after treatment with H_2O_2 (normalized to β-actin). Representative bands from 3 independent experiments (n=3). $*p<0.05$, relative to control. (C) Rac1 immunostaining following glutamate treatment. (D) Rac1 immunostaining following H_2O_2 treatment. Control= untreated cells. Rac1 represented in green. Nuclei counterstained with DAPI (blue). White arrows denote Rac1 accumulations. Scale bar is 20µm.

Although, only 600 µM achieved a significant 4-fold increase in expression when compared to cells cultured under normal conditions.

These results indeed showed a significant increase of total Rac1 protein expression after a neurotoxic stimulus. Nonetheless, Rac1 activation was not assessed herein and thus it cannot be assured whether this increase is associated or not with an increased activation of Rac1. It is important to state that many studies addressing Rac1 increase following an ischemic neuronal injury both *in vivo* and *in vitro* report an increase of active Rac1 with the maintenance of total Rac1 values [52,54,55,57,65]. Nevertheless, some of these studies were performed *in vivo* [52,54,57] where the analysis included the response of non-neuronal cells as well. Comparing with the reported studies *in vitro* [55,65], the time points when the analysis was performed were shorter (20 min or 60 min respectively) which is enough to see alterations in activity, but possibly not enough to see the increase in total protein Rac1 levels as in our case where the analysis was performed 4h after stimulus. Moreover, previous studies from our group showed a significant Rac1 protein increase in parallel with a decrease in Rac1 activity in ischemic cortex 24h after a permanent focal brain ischemia model (unpublished data). Accordingly, another *in vivo* study reported similar data showing an increase in total Rac1 along with a decrease on active Rac1 after global brain ischemia [58].

Despite these variable results between different reports, it is proven with these findings that there is an upregulation of Rac1 expression following a stress stimulus. Thus, we hypothesize that this modified expression of Rac1 is associated to the already discussed detrimental role of this protein in ischemia.

Rac1 immunostaining was also performed to confirm western blot results and to evaluate Rac1 subcellular localization after a neurotoxic stimulus (Figure 14C and Figure 14D). Treatment with 16 mM glutamate indeed induced an increase on Rac1, however it is interesting to note that the increase is most pronounced in the more stressed cells, which show an atrophy of the dendrites and a round shape. This suggests that Rac1 increase occurs primarily on more damaged cells. Regarding Rac1 localization, it appears to occur mainly on the cellular cytoplasm. For cells treated with H_2O_2, the alterations on cells morphology is even more evident, namely for the higher concentrations, as predicted, attending to the cellular viability data (Figure 13B). Furthermore, a clear increase on Rac1 expression can be seen for the 400 and 600 µM H_2O_2 concentrations, although through western blot only the higher concentration was found to lead to significant increase on protein levels. As predicted, 600 µM H_2O_2 revealed the greater increase of Rac1 in comparison to the control cells. Rac1 accumulations after H_2O_2 toxicity can be seen at the cell periphery, seeming to occur at the cellular cytoplasm. Although the peripheral localization of this protein may suggest that Rac1 is also situated at the cell membrane, which is associated with its active form [17], a cell membrane staining would be required to confirm this.

In order to support the relevance of Rac1 expression in neuronal excitotoxic conditions, HT22 cells were differentiated in neuronal cell culture conditions. Cells differentiation allows for the acquisition of more postmitotic neuronal characteristics, such as neurite outgrowth and, importantly, expression of NMDA receptors. The presence of glutamate receptors confers excitatory properties to HT22 cells, which implies the use of lower glutamate concentrations as there is an increase on cells vulnerability to this compound [96]. Therefore, while for undifferentiated cells an oxidative stress stimulus was being used, with differentiated cells glutamate will act mainly through excitotoxicity. After differentiation for 48h, HT22 cells were treated with micromolar doses of glutamate, after which Rac1 expression was evaluated through immunostaining (Figure 15). In these cells, a protein increase could also be noticed after the toxic stimulus. Furthermore, it is interesting to note here that the protein accumulations occurred both in the cytoplasm (white arrows) and cell nucleus (yellow arrows), which may suggest additional functions of Rac1 protein in a neurotoxic situation. So, these findings further support the existence of an increased expression of Rac1 in conditions that mimic neuronal ischemia.

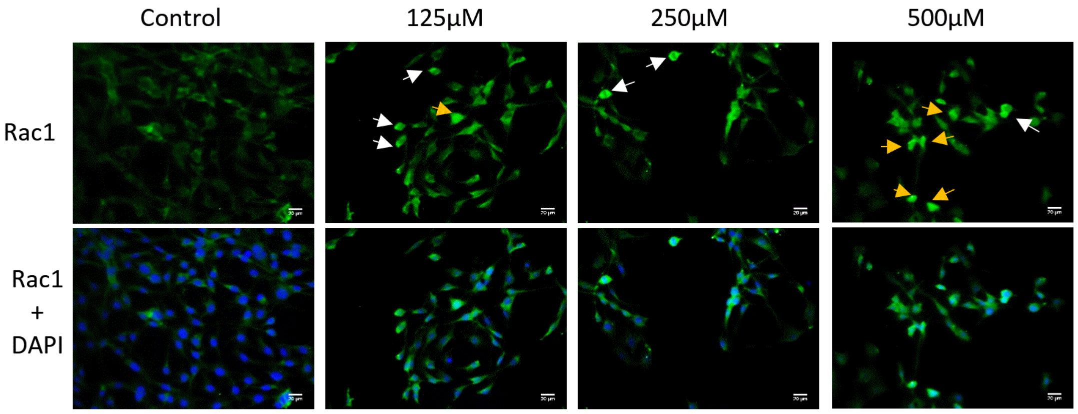

Figure 15 Rac1 expression in differentiated HT22 cells 4h after treatment with different concentrations of glutamate. Control= untreated cells. Rac1 represented in green. Nuclei counterstained with DAPI (blue). White arrows denote cytoplasmic Rac1 accumulations. Yellow arrows point nuclear Rac1 accumulations. Scale bar is 20µm.

Rac1 expression results obtained with differentiated HT22 seemed promising for further studies. Nevertheless, the maintenance of these differentiated cells in culture, for the long time periods needed to perform the different experiments, revealed to be very challenging as cells became stressed few days after differentiation and also with medium change. Although different strategies were employed to overcome this problem such as the use of different supplements to induce differentiation or the maintenance of half the culture medium when cells medium was changed, these approaches were not successful. Figure S 3 shows two images of differentiated HT22 cells (with or without culture medium change in four days of culture) in which it can be clearly seen that cells were clumped together – a typical response of stressed neurons - and dethatched. As a consequence, studies were carried only with undifferentiated HT22 cells.

The results presented here show a decrease on HT22 cellular viability and an increase on Rac1 protein expression upon a neurotoxic stimulus. After showing the potential of this cell line to address the effect of Rac1 expression in a neurotoxic condition, the next step is to find an optimal approach to modulate its expression. For this, TMC was chosen as the non-viral siRNA delivery biomaterial. Complexes formed with Rac1 siRNA sequences were prepared, characterized and their performance *in vitro* was evaluated. It is important to highlight that contrary to many of the studies cited here [52,55,58], in this work Rac1 expression is silenced genetically, without the use of pharmacological inhibitors of activity nor dominant-negative mutants. This may elucidate whether abolishing the increased expression found here is better when compared with the outcomes of only inhibiting Rac1 activity as performed by others.

4.2. TMC polyplexes characterization

4.2.1. TMC-siDNA complexes

4.2.1.1. Size, polydispersity index and zeta potential

siDNA sequences without any known biological function were used for optimization studies in order to determine the best N/P ratios to use for further studies with siRNA sequences. TMC-siDNA complexes, synthetized with 5 different N/P ratios (from 1 to 12), were investigated regarding the hydrodynamic diameter (hereinafter referred to as size) and PDI (Figure 16A and Figure 16B), through DLS. For N/P ratios higher than 1, nanoparticles showed adequate sizes for cell internalization [75,76] (ranging from 175 nm to 233 nm). Notoriously, for ratios higher than 2 nanoparticles smaller than 200 nm were always obtained. These results reveal a decrease on average nanoparticles size with increasing N/P ratios and a tendency for the stabilization of the complexes size with higher N/P ratios. This trend is likely attributed to an increased polymer content in the formulations, which leads to tighter complexes formation. With the exception of N/P 1, the size distribution of complexes was quite narrow, as shown by the PDI (ranging from 0.078 to 0.181). At a TMC/siDNA ratio of 1:1, the amount of polymer is not enough to form compact complexes as demonstrated through the polyplex size and PDI. Size and PDI values obtained are in accordance with values described in literature for TMC and chitosan complexes formed with siRNA sequences [75,77,81,82,101].

It is consensual that effective non-viral gene delivery systems should be amenable to freeze-drying process [76,80]. Furthermore, this process might be used to concentrate nanoparticles, which may be necessary, for instance, for *in vivo* administrations when there is a limit in the volume of nanoparticles to be administered. In the present study, TMC polyplexes were concentrated through freeze-drying for subsequent intranasal administration. To understand if the obtaining complexes were suitable for lyophilisation, these polyplexes were characterized before and after this process. Lyophilisation promoted an increase on both size and PDI of the complexes (Figure 16A and Figure 16B). Interestingly, the increase in size was found to be more notorious for lower N/P ratios, although all increases were significant. For PDI, N/P 1 was the only ratio in which no increase on PDI was verified. The size increase for lower N/P ratios can be attributed to the softer interactions within these complexes due to the lower polymer amount which in turn lead to an increased tendency for aggregation or structure destabilization. Chitosan aggregation occurs due to inter- and intramolecular hydrogen bonding [102]. Thus, vortex or sonication could have been strategies applied to avoid this phenomenon. Chitosan complexes aggregation after lyophilisation has already been reported by other authors [80,102]. Importantly, in the present study, aggregation occurred to a much lesser extent than in these reports.

Although nano-sized particles were again obtained after lyophilisation, the extremely small volume in which particles were reconstituted for *in vivo* studies, when compared to the initial volume, should have led to high losses and to high buffer molecules present in the reconstituted nanoparticles. Thus, aiming at diminishing the initial volume of nanoparticles to lyophilise and, consequently the density of the lyophilisation product (which contains buffer molecules), polyplexes with N/P 4 and 8 were synthetized to a final siDNA concentration of 50 µg/ml, instead of the usual concentration of 12.5 µg/ml. The size of these “high concentration” polyplexes was bigger than the previously obtained (Figure 16C, before lyophilisation) with both N/P ratios presenting sizes above 200 nm. PDI values were also slightly higher (Figure 16D), with significant differences in N/P 4. Nevertheless, contrary to what was found for particles synthetized under protocoled conditions, there were no changes on complexes size and PDI after freeze-drying. Our results indicate that increasing the concentration of particles in the suspension to be freeze-dried clearly reduced the damage caused to the nanoparticles. Another study also suggested that nanoparticles concentration has a critical effect on the success of nanoparticles freeze-drying [103]. This can be explained by the fact that only a limited number of particles in the liquid-ice interface will be damaged during the freezing process and, thus, increasing the initial nanoparticle concentration will lead to a smaller percentage of damaged nanoparticles [104].

Another strategy envisaged for the *in vivo* studies was the use of PEGylated TMC polyplexes that were also synthetized and characterized through DLS (Figure 16E and Figure 16F). TMC modified with thiol moieties was used for this synthesis and N/P ratios of 4 and 8 were studied. A percentage of 4.9% of TMC primary ammines was modified with thiol groups and the modified polymer was incubated with polyethylene glycol (PEG), containing a maleimide reactive group, in order to promote the PEGylation of 25% (TMC-PEG-25) or 75% (TMC-PEG-75) of thiol groups. There were no significant changes in sizes neither in PDI among the different PEGylation percentages. Sizes remained similar between the two N/P ratios studied, whilst PDI

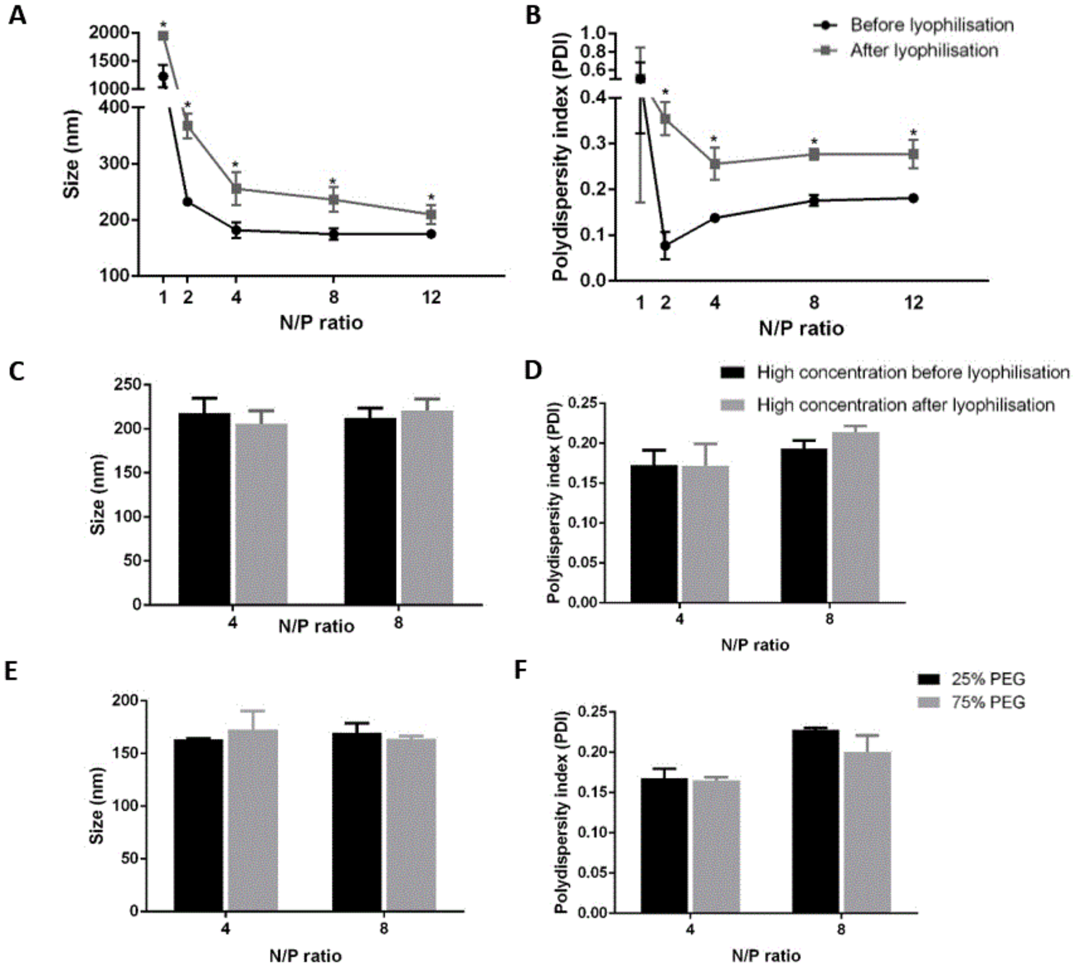

Figure 16 Size and PDI of TMC-siDNA polyplexes. (A) TMC-siDNA complexes size as a function of N/P ratio before and after lyophilisation (n=4 before lyophilisation, n=2 after lyophilisation). (B) TMC-siDNA complexes PDI as a function of N/P ratio before and after lyophilisation (n=4 before lyophilisation, n=2 after lyophilisation). (C) TMC-siDNA "high concentration" complexes size for N/P 4 and 8 before and after lyophilisation (n=2). (D) TMC-siDNA "high concentration" PDI for N/P 4 and 8 before and after lyophilisation (n=2). (E) TMC-PEG-siDNA complexes size for N/P 4 and 8 with 25 and 75% of thiol groups modified with PEG (n=2). (F) TMC-PEG-siDNA complexes size for N/P 4 and 8 with 25 and 75% of thiol groups modified with PEG (n=2). * $p<0.05$, unpaired t-test was employed.

values were slightly higher for N/P 8 complexes, similar to what occurred for the other conditions (Figure 16B and Figure 16D). Nevertheless, the PDI values obtained showed a narrow size distribution for the all the formulations. No significant differences on the mean particles size were noticed in comparison with non-PEGylated formulation, which is in accordance with other report [80]. Nevertheless, PDI values were found to be higher for PEGylated particles, with exception of, TMC-PEG$_{75}$ at N/P 8.

Zeta Potential of TMC-siDNA complexes was also evaluated for the N/P molar ratios 2, 4 and 8 (Table 1). The excess TMC in all formulations resulted in positively charged nanoparticles (between +9 and +10mV), with no differences between the different N/P ratios. The presented zeta potential results emphasize the potential of these complexes as carriers of nucleotide sequences for cellular delivery, as they have the capability to interact with negatively charged membranes. Furthermore, the fact that these values are close to zero can be an advantage regarding complexes cytotoxicity, once excessive positive charge is associated with cellular damage [84]. However, it is important to refer that highly charged nanoparticles may comprise other advantages, such as endosomal escape [70,74,81].

N/P ratio	**2**	**4**	**8**
Zeta Potential (mV)	9.64 ± 1.13	9.98 ± 2.82	9.20 ± 0.91

Table 1 Zeta Potential of TMC-siDNA polyplexes (n=2).

4.2.1.2. Stability

The interaction strength between the siDNA nucleotide sequences and the polymer, at different N/P ratios, was assessed by gel retardation assay. In this assay, the weakly bound or unbound siDNA sequences, will migrate through the gel when subjected to electrophoresis, whereas strongly bound siDNA will remain in the wells together with the polymer, as the size of the complexes does not allow gel migration.

When complexes were analysed in the day of the synthesis (0d), complete retardation of the siDNA was achieved for N/P ratios higher than 1 (Figure 17A). N/P 1 ratio showed low binding affinity, likely caused by the relatively low polymer content, which may have prevented polymer condensation. This is in accordance with what was discussed for lyophilisation of low N/P ratios on the previous section. Gel retardation assay was also performed 1 day (1d) after complexation in order to ascertain the stability of these complexes after storage (Figure 17A). In this gel, siDNA loss from the complexes at N/P 1 was also seen, while a smear band could be noticed for N/P 2. This smear indicates that siDNA is also being released from these nanoparticles, however with a delay due to a stronger binding to TMC than at N/P 1. Thus, at an N/P ratio of 2, complexes start losing stability after 1d. For the other N/P ratios, sequences remained entrapped in the complexes, revealing strong and stable interactions with TMC for at least 1d.

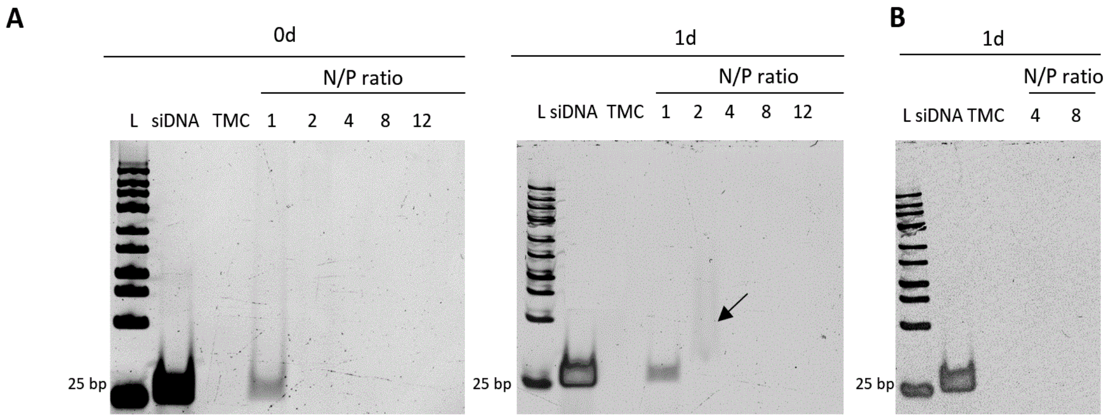

Figure 17 siDNA gel retardation assay. (A) TMC-siDNA complexes at different N/P ratios at 0d and 1d after complexation. Black arrow indicates a smear band showing the existence of delayed siDNA release. (B) TMC-siDNA "high concentration" complexes, 1d after complexation. L=ladder; TMC: TMC was loaded in an amount equal to N/P 8 formulation.

"High concentration" TMC-siDNA complexes were also analysed through gel retardation assay for the N/P ratios already mentioned in the other characterizations. Results, 1d after complexation, show that siDNA is also strongly bound to TMC in these conditions (Figure 17B).

The verified high stability of the particles is in agreement with other reports using TMC polyplexes [77,93,101]. Importantly, TMC complexes have been reported to be more stable than complexes with chitosan, which can account for an improvement on complexes cellular internalization and transfection efficiency [77,87]. Complexes high stability is of foremost importance also for *in vivo* studies, in which complexes are exposed to harsh conditions [74] and, thus, the synthetized complexes present promising features for *in vivo* applications. Moreover, TMC is soluble at neutral pH contrary to chitosan, which requires acidic pH and this leads to a more favourable condition for TMC transfection [77,78].

4.2.2. TMC-siRNA complexes

4.2.2.1. Size, polydispersity index and zeta potential

Complexes formed with Rac1 siRNA sequences were also analysed concerning their size and PDI, on 3 selected N/P ratios (Figure 18). As predicted by the similarities between the sequences, no differences on nanocomplexes size were found between complexes with siDNA or siRNA sequences. However, a slight increase on the PDI values was obtained, suggesting a broader sizes distribution for siRNA nanoparticles. Nevertheless, PDI values were inferior to 0.3 (highest obtained values were 0.273 for N/P 8), meeting the performance criteria of effective non-viral gene delivery system [76]. Zeta potential of siRNA complexes was also evaluated for the same N/P ratios (Table 2) and obtained values were in agreement with the already discussed zeta potential results for siDNA complexes (Table 1).

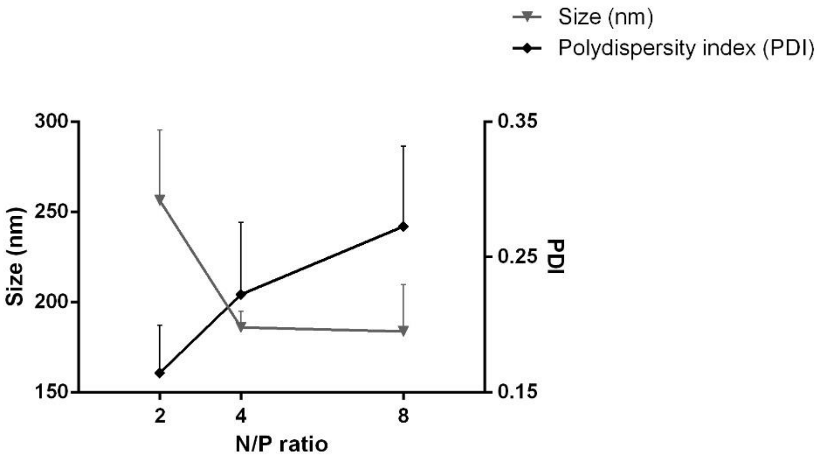

Figure 18 Size and PDI of TMC-siRNA polyplexes (n=3).

N/P ratio	2	4	8
Zeta Potential (mV)	10.38 ± 0.84	7.61± 2.25	9.38 ± 0.85

Table 2 Zeta Potential of TMC-siRNA polyplexes (n=3).

4.2.2.2. Stability and protection from RNase degradation

TMC-siRNA complexes were also studied regarding their stability, at 0 and 1d after complexation (Figure 19). Similarly to siDNA, no siRNA release was observed in N/P ratios 4 and 8. Nevertheless, on the day of complexation (0d), a smearing was already visible for the N/P 2, complexes, which was maintained 1d after complexation. Furthermore, as highlighted by the yellow arrows, it was noticed the existence of siRNA sequences bound to TMC at the bottom of the wells. Apparently these sequences were not so stable within the complex structure and therefore during electrophoresis their migration in the gel was only partially retarded as opposed to N/P 4 and N/P 8, where complete retardation was observed. This pattern in the bottom of the well and the smear band at 0d were not observed for the siDNA sequences, which may be explained by the sequence/structural differences between siDNA and siRNA.

To further perform polyplexes characterization, their capability to protect siRNA sequences from RNases degradation was evaluated. Both siRNA sequences and TMC-siRNA complexes (N/P 8) were incubated in the presence of RNase A for 5 different time periods ranging from 0 to 4h and, after release of the sequences with detergent treatment, these were loaded into a gel (Figure 20). Intact siRNA was maintained after release from TMC nanoparticles in all the conditions, whereas naked RNA was progressively degraded achieving complete degradation after 2h. Nevertheless, it can be noted a reduction of about 30% on complexes siRNA amount after incubation with RNases, independently of the exposure time to the enzymes. This might be justified by the existence of sequences not so well entrapped within the complex structure and, thus, more susceptible to nucleases action. These results suggest that TMC effectively protects at least 70% of the incorporated siRNA sequences, for up to 4h, in high concentration nuclease conditions.

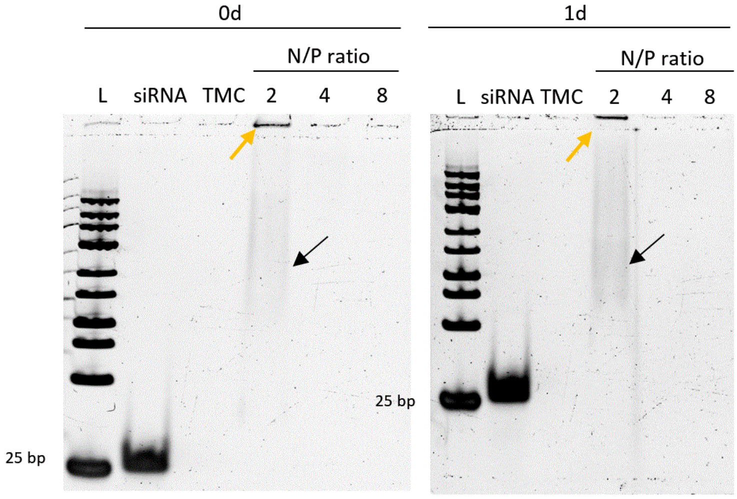
0d
1d
N/P ratio
L siRNA TMC 2 4 8
N/P ratio
L siRNA TMC 2 4 8
25 bp
25 bp

Figure 19 siRNA gel retardation assay with complexes formed at different N/P ratios, 0 and 1d after complexation. Black arrows indicate a smear band showing the existence of delayed siDNA release. Yellow arrow indicates the existence of siRNA sequences in the well. L=ladder; TMC: TMC was loaded in an equal amount to N/P 8 formulation.

Altogether, the presented data, regarding TMC complexes characterization, shows the synthesis of positively-charged nanocomplexes, presenting highly desirable sizes for siRNA delivery, high stability and good capabilities to protect siRNA sequences. These features motivated the subsequent *in vitro* studies to address polyplexes biological activity and *in vivo* studies to address complexes ability to reach the brain.

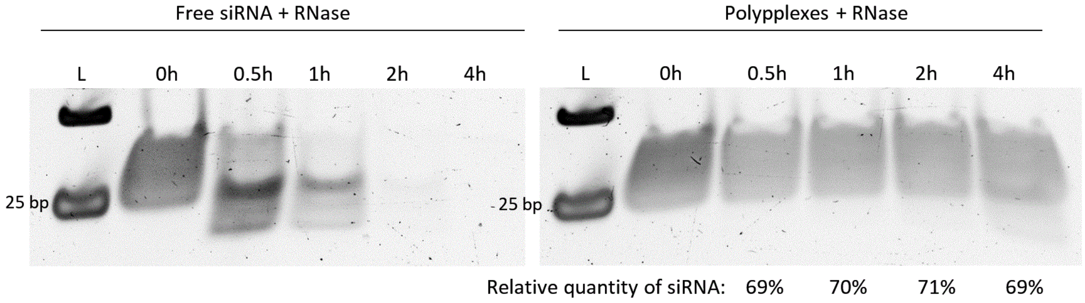
Free siRNA + RNase
Polypplexes + RNase
L 0h 0.5h 1h 2h 4h
L 0h 0.5h 1h 2h 4h
25 bp
25 bp
Relative quantity of siRNA: 69% 70% 71% 69%

Figure 20 RNase protection assay. Gel retardation was performed for free siRNA and for TMC-siRNA complexes prepared at N/P 8, after incubation with RNase A for different time periods. Relative quantity of siRNA is compared to the 0h incubation, for polyplexes + RNase condition. L=ladder.

4.3. TMC polyplexes *in vitro* cell association and internalization

4.3.1. TMC-siDNA complexes

Following TMC polyplexes characterization, studies were performed in order to evaluate their capability to transfect HT22 cells. TMC complexes cellular association and internalization were assessed using TMC-siDNA$_{cy5}$ complexes with different N/P ratios. To find optimal siDNA concentrations for the transfection studies, cells were incubated with 50 and 200nM final concentrations of siDNA. Results were assessed by fluorescence microscopy 24h after incubation with the complexes. This analysis was performed with differentiated HT22 (data not shown), however the cells were not in optimal health status at the experiment endpoint. This may have decreased the transfection efficiency but allowed us to compare the 2 concentrations selected. Using 50 nM siDNA, cy5 fluorescence was only detected in cells transfected with lipofectamine (commercially available transfection reagent used as positive control). On the other hand, when using 200nM siDNA, fluorescence was found on N/P ratios 2, 4 and 8. Also, the quantity of siDNA$_{cy5}$ sequences in cells augmented with the N/P ratio increase (i.e. N/P 8, the highest ratio tested, showed highest siDNA internalization). It is important to highlight, in this context, that a concentration of 200nM means a 4-fold increase on nanoparticles quantity per well and thus the optimization of siDNA concentration implies an optimization of complexes concentration. As 200nM is a relatively high concentration for transfection, in subsequent studies, performed with undifferentiated HT22 cells, 100 nM siDNA concentration was also investigated.

Fluorescent cells were detected by flow cytometry, 24h after incubation with the polyplexes at a siDNA final concentration of 100 or 200nM. As shown in Table 3, siDNA$_{cy5}$ fluorescence was detected in 100% or near 100% of the cells for all the conditions tested. However, evaluation of the cy5 fluorescence intensity (Figure 21A) revealed significant differences between the different siDNA concentrations and N/P ratios tested. Fluorescence intensity of cells incubated with 100 nM siDNA was meaningfully lower for TMC polyplexes than for lipofectamine. Furthermore, no difference on fluorescence intensity was found between the two N/P ratios tested (N/P 4 and N/P 8) for this siDNA concentration. Nonetheless, when cells were incubated with 200nM siDNA, a clear shift on cy5 fluorescence was noted for all the conditions when compared to 100 nM siDNA. At this concentration, fluorescence intensity increased as a function of the N/P ratio and maximum cy5 intensity was achieved for the N/P ratios of 8 and 12. For these two formulations, siDNA$_{cy5}$ association to cells was even higher than for the much used transfection agent, lipofectamine. Despite these very good results, flow cytometry only gives information about the total cell fluorescence, not distinguishing between membrane-associated or internalized complexes. This may justify the fact that cells incubated with N/P 1 TMC had cy5 fluorescence. Having a size on the micrometre scale, N/P 1 polyplexes are more difficult to be internalized by the cells [76,77,93] and thus it is reasonable to assume that some of these sequences are outside the cells. Having in mind the results of N/P 1 and N/P 2 regarding their sizes and stability, it was already expectable a lower performance for these two ratios. Nevertheless, the very high fluorescence intensity for N/P 4, N/P 8 and N/P 12 strongly suggests that there was a cellular uptake of the complexes. Differences found between N/P 4 and N/P 8 and 12 may be justified by a possible optimal stability of the formulations for higher N/P ratios.

Sample	**siDNA concentration (nM)**	**% of positive cells**
Lipofectamine	100	99.9
	200	97.5 ± 1.8
N/P 1	200	94.5 ± 4.5
N/P 2	200	99.3 ± 0.7
N/P 4	100	100
	200	100 ± 0
N/P 8	100	99.9
	200	100 ± 0
N/P 12	200	100 ± 0

Table 3 Percentage of cells with cy5 fluorescence, 24h after incubation with TMC or lipofectamine complexes (n=1 for 100nM, n=2 for 200nM).

Flow cytometry results were confirmed with fluoresce microscopy (Figure 21B). N/P 1 ratio was not evaluated as the results for this formulation were not promising. Concerning N/P 12, as the flow cytometry data was comparable to the N/P 8, it was excluded in order to avoid possible cytotoxicity issues related to the high polymer content of the formulation [75]. Figure 21B shows the internalization of nanoparticles in cells incubated with N/P 4 and N/P 8 formulations at 200nM siDNA concentration. Within these conditions, brighter signal is seen with N/P 8, as predicted. Cy5 signal can also be seen on N/P 2, however siDNA$_{cy5}$ is not present in the cells at an appreciable amount. Also, for this condition red dots are mainly seen in the periphery, which indicates that complexes might be at the cell membrane. Flow cytometry has a higher sensitivity when compared to microscopy, which explains the detection of cy5 fluorescence in almost 100% of cells which is not seen by imaging. In agreement with this, other report with chitosan nanoparticles shows the detection of signal by the flow cytometer that is not detected by microscopy [81]. As 200nM siDNA was the most effective condition, it was selected for subsequent *in vitro* studies. Despite being a high concentration, there are other reports using this [81] or even higher [93] siRNA/oligonucleotides concentrations to achieve good transfections efficiencies with chitosan polyplexes.

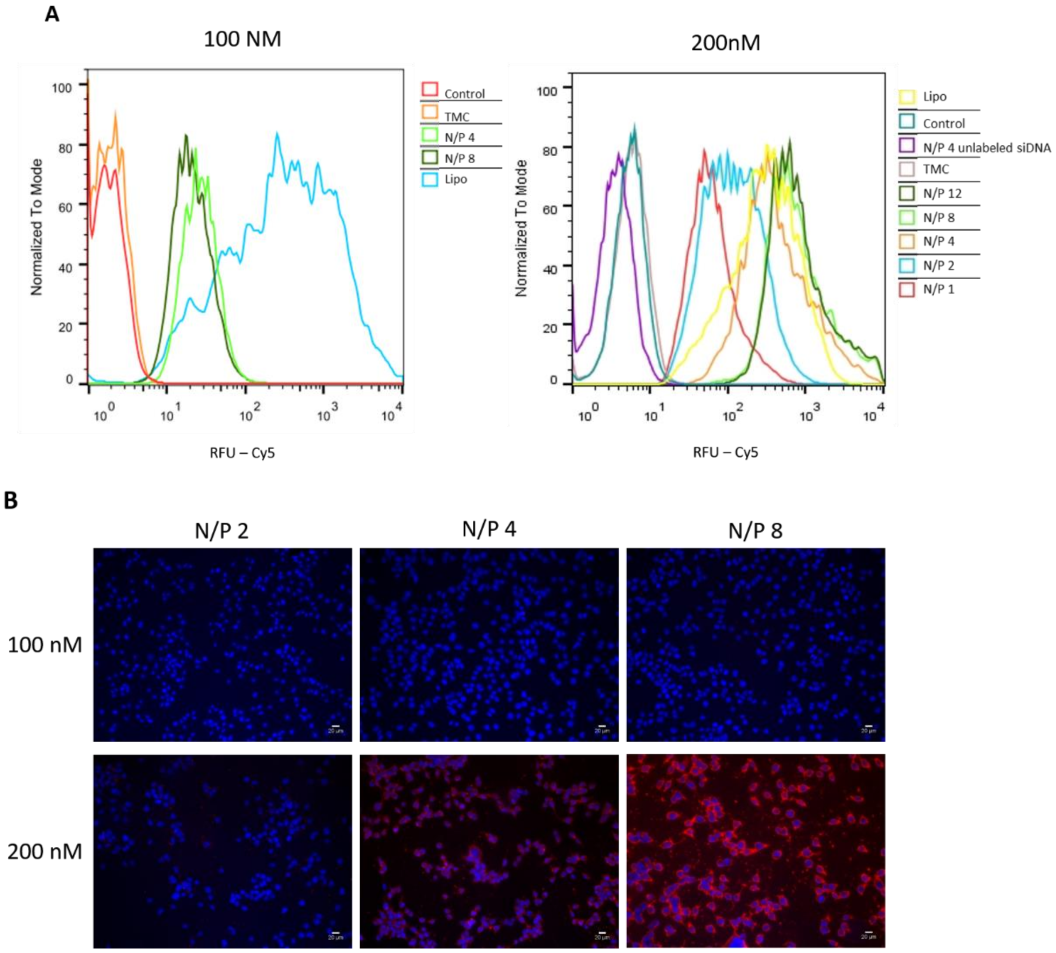

Figure 21 Association of TMC-siDNA complexes to HT22 cells 24h after incubation with 100 and 200nM siDNA$_{cy5}$. (A) Histograms of cy5 fluorescence intensities. Cells with no treatment (control), treated with only TMC (TMC) and/or treated with N/P 4 TMC complexes with unlabelled sequences (N/P 4 unlabelled siDNA) were used as control. RFU=relative fluorescence units. Lipo= lipofectamine. (B) Fluorescence microscopy images of TMC-siDNA$_{cy5}$ polyplexes interaction with cells. Nuclei is stained in blue (DAPI) and siDNAcy5 represented in red. Scale bar is 20µm.

Confocal microscopy was also employed to confirm the internalization of the polyplexes as well as their subcellular distribution (Figure 22). Both N/P 4 and N/P 8 showed a wide distribution of siDNA$_{cy5}$ sequences in the cell cytoplasm, 24h after incubation with the nanocomplexes. From the higher magnification images it is clear that, although the existence of agglomerates suggesting siDNA accumulations in endocytic vesicles [77], a considerable part of the red pattern is diffused through the cells indicating that siDNA$_{cy5}$ sequences were able to escape from the endosomes. This diffuse pattern is consistent with other imaging works with chitosan complexed with double stranded oligonucleotide sequences [76] or with plasmid DNA [105].

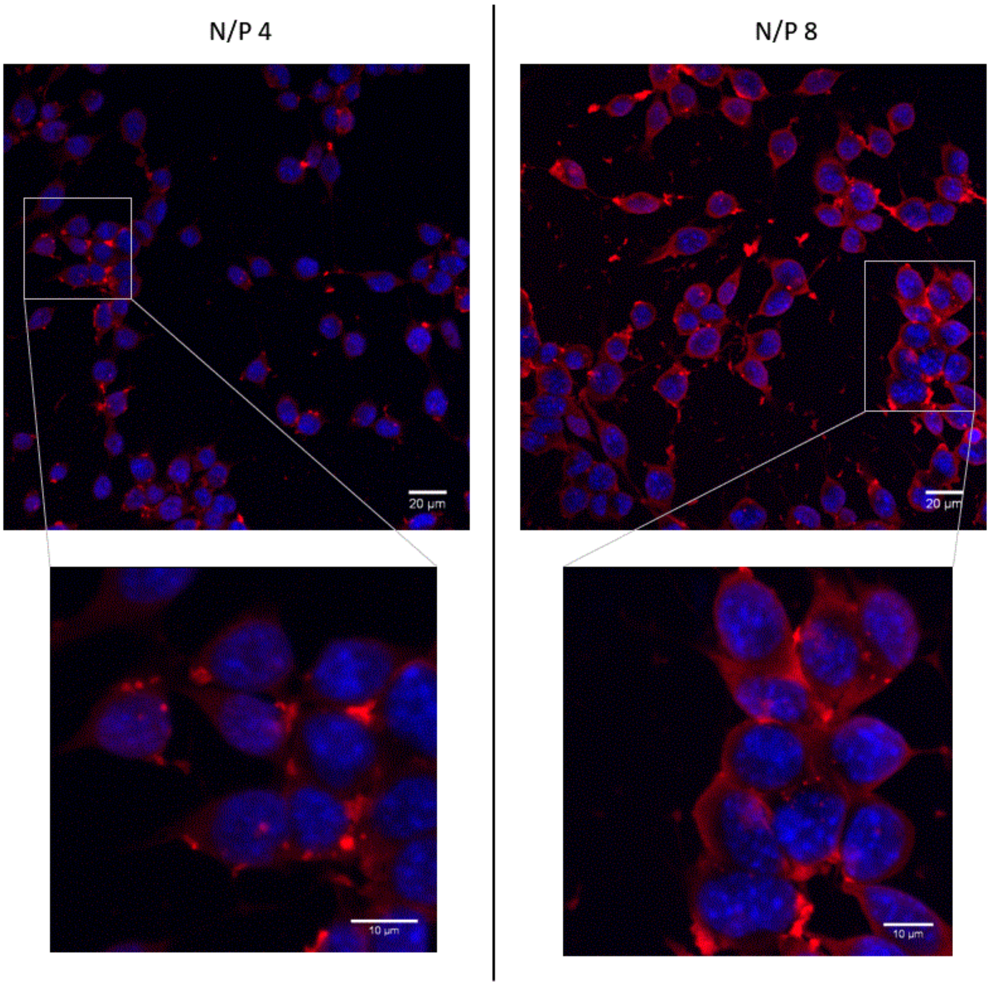

Figure 22 Confocal microscopy images of HT22 cells, 24h after transfection with TMC-siDNA$_{cy5}$ (N/P 4 and 8, 200nM siDNA$_{xy5}$). Rectangular highlighted areas are shown at a higher magnification. Nuclei is stained in blue (DAPI) and siDNA$_{cy5}$ represented in red.

Finally, studies with TMC$_{ROX}$-siDNA complexes were performed to investigate the cellular fate of complexes 4 and 24h after incubation with the cells (Figure 23). From the images it can be noted that after 4h, fluorescence is located on more apical regions of the cells and within compartmentalized areas. However, 24h after transfection, complexes are more dispersed throughout the cells, indicating that polyplexes were, likely, able to escape endosomes. Of notice, polyplexes colocalization with the nucleus and perinuclear regions (white arrows) constitutes another indicator of successful internalization [93]. Furthermore, the increase on polyplexes cellular association and internalization 24h after transfection suggests that complexes are still interacting and entering in the cells after the 4h incubation. Indeed, this continuous binding and uptake of chitosan polyplexes over 24h was already reported [93,105].

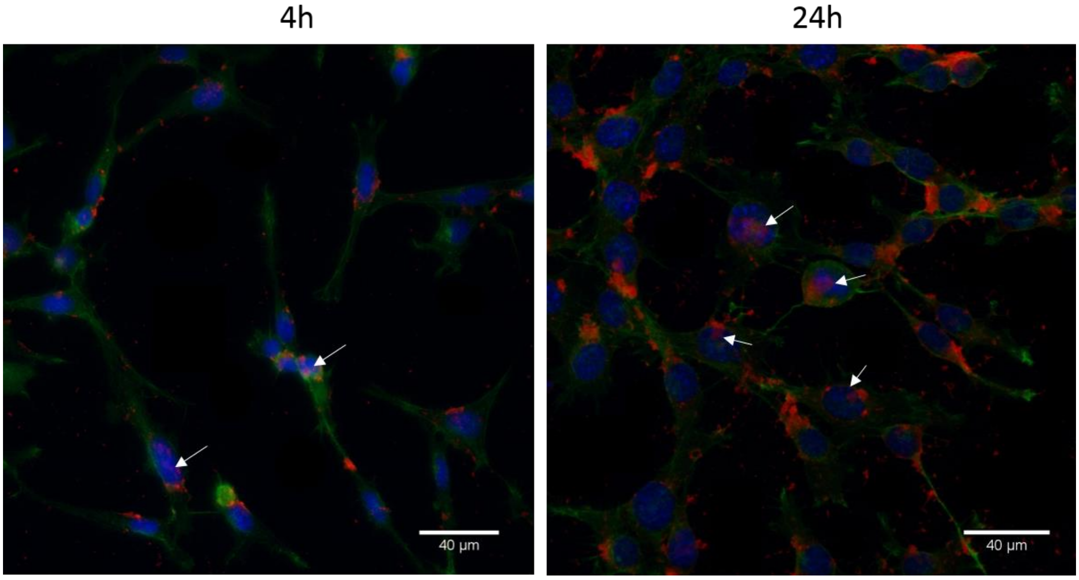

Figure 23 TMC$_{\mathrm{ROX}}$-siDNA (N/P 8) cellular uptake after incubation for 4 and 24h (200nM siDNA). Left picture was taken on a fluorescence microscope and picture on the right was taken on a confocal microscope. Cells cytoskeleton is coloured in green with phalloidin to help on the visualization of nanoparticles interaction with cells. Nuclei is stained in blue with Hoechst. TMC$_{\mathrm{ROX}}$ is represented in red. White arrows indicate TMC$_{\mathrm{ROX}}$ colocalization with the nucleus and perinuclear regions.

4.3.2. TMC-siRNA complexes

After determining the best condition for siDNA transfection, the same studies were performed with siRNA using FAM-labelled siRNA control sequences (siRNA$_{\mathrm{FAM}}$). Flow cytometry was again employed to evaluate sequences cellular association. Surprisingly, low values of siRNA$_{\mathrm{FAM}}$ cellular association and FAM fluorescence intensity were found for TMC complexes (Figure 24A and Figure 24B, respectively) when comparing with the results achieved with siDNA$_{\mathrm{cy5}}$ sequences (Table 3 and Figure 21A). Cellular association obtained with N/P 8 was about 3-fold lower than what was found for lipofectamine (Figure 24A). There was a significant increase on N/P 8 cellular association when comparing with the N/P ratio 4, though the percentage obtained was much lower than the 100% obtained for siDNA. Also, the low levels of cell-associated sequences with the other N/Ps was not expected. Fluorescence microscopy images also supported these results (Figure 24C). A high presence of siRNA sequences in the cells with lipofectamine was observed, while for TMC complexes only N/P 8 shows positive fluorescent signal, even though it is at a low level. siDNA and siRNA have different nucleotide sequences and slightly different sizes (few base pairs of difference), but these minor chemical and structural variances cannot justify the obtained results. Moreover, similar data obtained after complexes characterization emphasize that polyplexes formed with siDNA or siRNA should have similar performances *in vitro*.

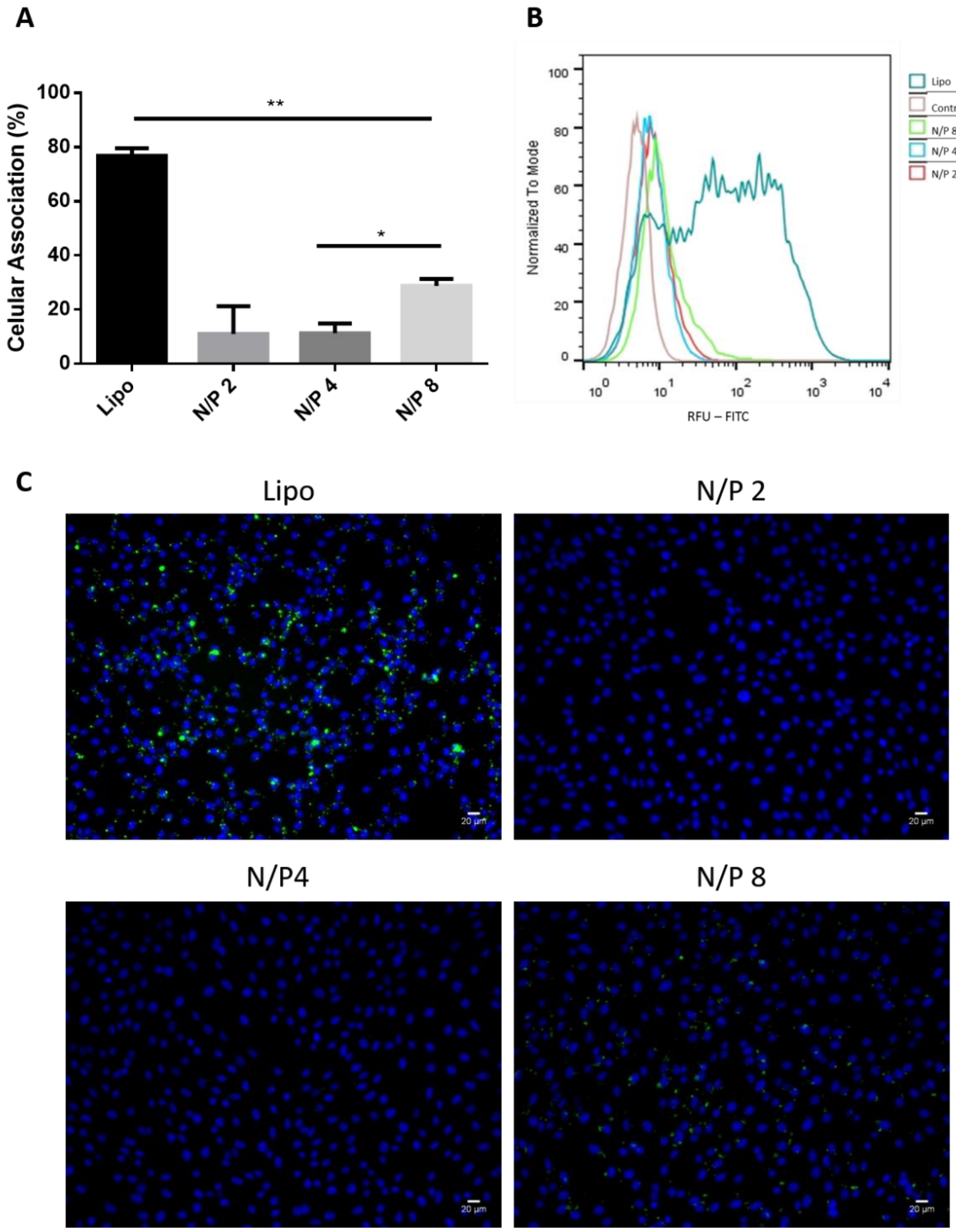

Figure 24 Association of TMC-siRNA complexes to HT22 cells 24h after incubation with 200nM siRNA$_{\mathrm{FAM}}$. (A) Percentage of complexes cellular association (n=3). *$p<0.05$ **$p<0.01$ (B) Histograms of FAM fluorescence intensities. Cells with no treatment were used as control. RFU=relative fluorescence units (C) Fluorescence microscopy images of TMC-siRNA$_{\mathrm{FAM}}$ polyplexes interaction with cells. Nuclei is stained in blue (Hoechst) and siRNA$_{\mathrm{FAM}}$ represented in green. Scale bar is 20µm. Lipo= lipofectamine.

Owing to this unexpected results, we hypothesized that there were problems with the siRNA sequences such as for example degradation. Figure S 4 shows a polyacrylamide gel result in which Rac1 siRNA and siRNA$_{\mathrm{FAM}}$ were compared. It is notorious the existence of nucleotide fragments smaller than 25 base pairs (black brackets) on the siRNA$_{\mathrm{FAM}}$ sequences, indicating that these sequences were in fact degraded. Lack of integrity of the sequences may have interfered with nanoparticles formation and stability and, consequently, with the transfection efficiency.

Regarding lipofectamine, this is a commercial reagent designed to be used with RNA or pDNA, which have different sizes, structures and topologies. Thus, it is probable that this reagent is not so sensitive to sequences integrity. It is therefore reasonable to assume that siRNA$_{FAM}$ sequences were not in perfect conditions and that this was the reason for the obtained results.

In view of the above mentioned findings, another strategy was employed to verify the internalization of the TMC-siRNA complexes. Instead of FAM-labelled siRNA, rhodamine labelled TMC (TMC$_{ROX}$) was complexed with Rac1 unlabelled siRNA (which was not degraded, according to Figure S 4) and complexes cellular uptake was visualized by fluorescence imaging (Figure 25). Complexes internalization was confirmed and the pattern seen was comparable to the verified for TMC$_{ROX}$-siDNA transfection (Figure 23, 24h). Nevertheless, it should be noticed that polyplexes internalization seemed generally lower when comparing with TMC-siDNA polyplexes.

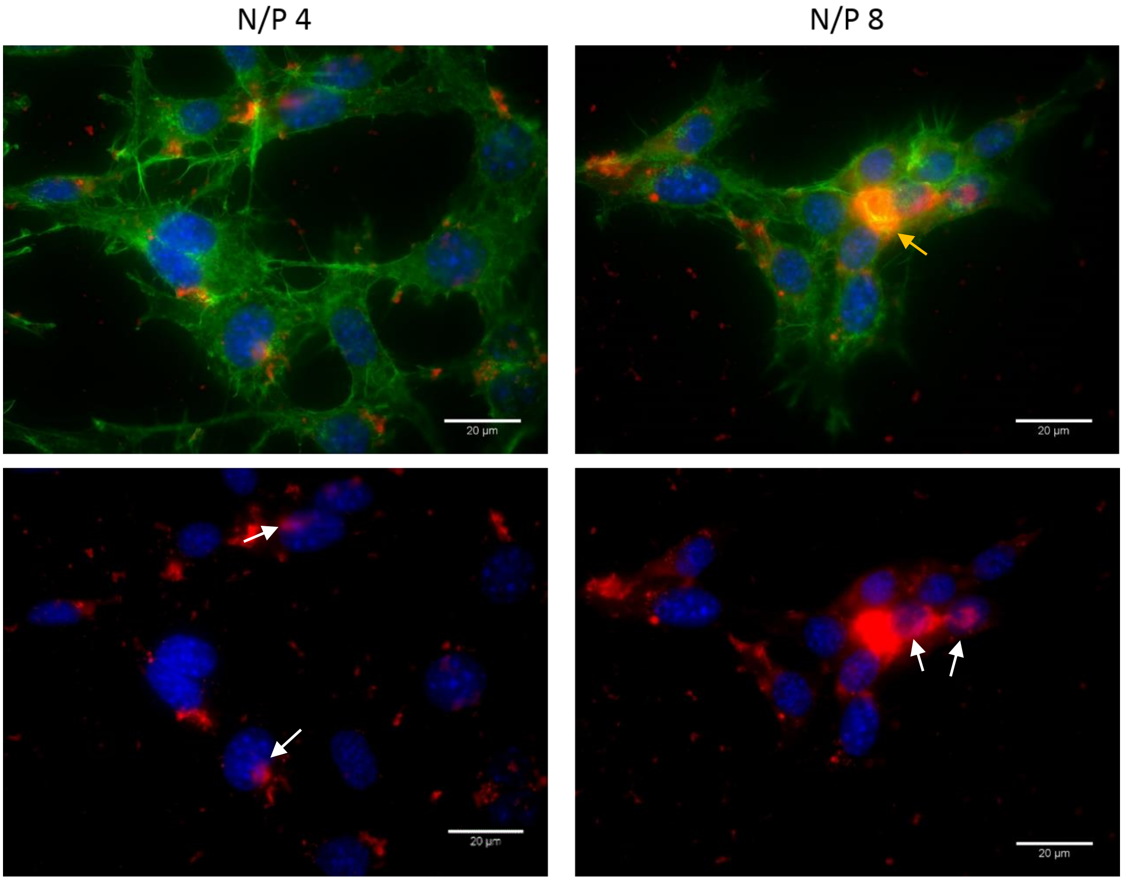

Figure 25 TMC$_{ROX}$-siRNA (N/P 4 and 8) cellular uptake 24h after incubation with 200nM Rac1 siRNA. Cells cytoskeleton is coloured in green with phalloidin. Nuclei is stained in blue with Hoechst. TMC$_{ROX}$ is represented in red. White arrows indicate complexes colocalization with the nucleus. Yellow arrow highlight complexes accumulations.

Once again, N/P 8 showed a higher efficiency and it could also be noted a more diffuse pattern, suggesting endosomal escape. Complexes co-localization with the nucleus can be seen for both ratios confirming that complexes are indeed inside the cells. Moreover, big complexes accumulations were seen with N/P 8 (as highlighted in the picture) that colocalize with actin.

These particles are probably entrapped in endosomes and thus will not contribute for siRNA delivery in the cytoplasm. This approach did not confirm siRNA sequences efficient deliver into the cell cytoplasm but showed that complexes containing Rac1 siRNA sequences are inside the cells.

After assessing the TMC polyplexes performance for siRNA and siDNA intracellular delivery, we next evaluated their cytotoxicity and concomitantly one of the major requirements for their use as carriers of therapeutic siRNA molecules.

4.4. TMC polyplexes *in vitro* cell cytotoxicity

An optimal gene delivery system should, among other requirements, not compromise cell viability [70,74]. Thus, to study cytotoxicity of TMC-siDNA complexes, particles formed at different N/P ratios were incubated with cells for 24h, after which cell viability was measured (Figure 26A). The results obtained were similar to the non-treated control for all the conditions studied, proving the non-toxicity of the complexes.

As a complementary approach to study cell viability in the presence of TMC polyplexes, calcein/PI staining was also employed (Figure 26B). The absence of toxicity for TMCcomplexes was confirmed as there was a minimal percentage of cells stained with PI (white arrows). Nevertheless, a qualitative analysis of cells treated with lipofectamine, showed some toxicity as detected by the presence of some PI stained cells. This staining highlighted a possible cytotoxicity of lipofectamine, though not consistent with the data from cellular viability with resazurin.

Importantly, these cell imaging results show again the high cell association verified for TMC-siDNA$_{cy5}$ complexes, especially for N/P8, which is higher when compared to lipofectamine reagent.

In summary, it was shown herein that TMC polyplexes do not have toxic effects in HT22 cells and it is suggested that these siRNA carriers are less cytotoxic than the commercially available reagent lipofectamine. Of notice, lower cytoxicity of chitosan-based nucleic acid carriers in comparison to lipofectamine have already been reported elsewhere [93]. Having studied the polyplexes ability to be internalized by cells and its toxicity, studies were proceeded in order to evaluate the efficiency of Rac1 silencing after transfection.

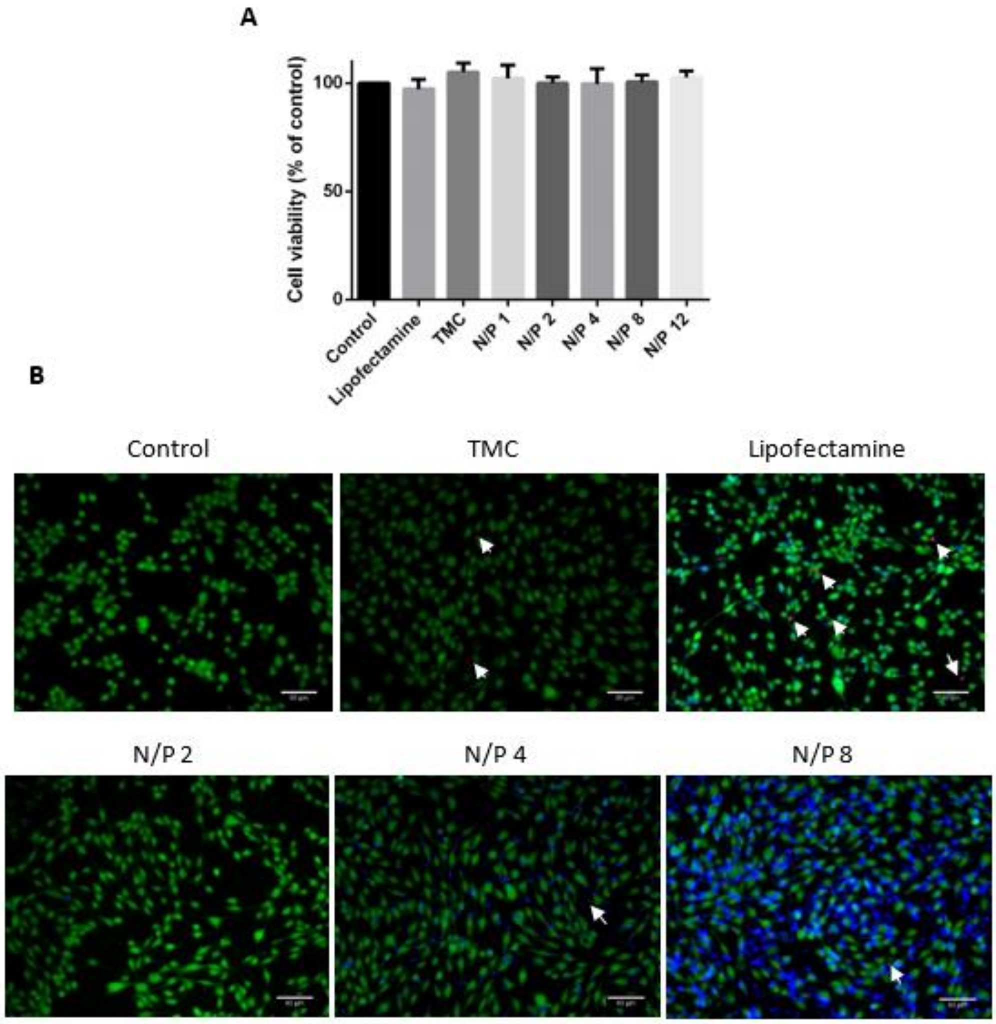

Figure 26 Cytotoxicity of TMC-siDNA complexes (A) Cell viability was measured through resazurin assay. Cells were incubated with TMC-siDNA$_{cy5}$ (at different N/P ratios) or lipofectamine for 24h (200nM siDNA concentration). Results are normalized to the cell viability of control (non-treated) cells (n=3). (B) Calcein/Propidium iodide staining. Representative fluorescence microscopy images of HT22 cells, 24h following incubation with TMC-siDNA$_{cy5}$ complexes or Lipofectamine (200nM siDNA$_{cy5}$). Calcein is represented in green. PI stained nuclei are in red. Cy5 is represented in cyan. White arrows highlight nuclei stained with PI. TMC: cells were incubated with an amount equal to N/P 8 formulation. Scale bar is 40µm.

4.5. Rac1 knockdown in HT22 cell line

4.5.1. Rac1 expression following transfection

The ability of TMC-siRNA polyplexes to efficiently downregulate targeted gene expression was evaluated by measuring Rac1 mRNA levels through qPCR. After RNA extraction from transfected cells, analysis of RNA integrity was performed by electrophoresis using Experion (Bio Rad). All RNA samples demonstrated good RQI (RNA quality indicator) values and an enrichment on 18S and 28S ribosomal units. Importantly, 28S bands were twice as the 18s bands, as it is expected. Samples treated with TMC nanocomplexes were equally good in comparison with the non-treated and lipofectamine transfected, demonstrating that chitosanase treatment had the desired effect, enabling for the obtainment of RNA with high integrity [79] (Figure S 2).

Rac1 gene expression was assessed 24h after Rac1 siRNA transfection and compared with non-targeting siRNA (negative control) (Figure 27). TMC-siRNA polyplexes were used at N/P 4 and N/P 8 ratios and two different mass ratios of lipofectamine/siRNA were employed as positive controls (ratio 1.5 and ratio 3). Notice that the sequences had not been previously validated. Cellular expression levels revealed a decrease of approximately 65% on Rac1 expression in comparison with the negative control transfected with lipofectamine. This enabled the validation of the biological function of the sequences. Nevertheless, TMC polyplexes transfection was unable to efficiently downregulate Rac1 expression. Attending to all the results here presented, there are two main aspects that can be discussed to clarify this non-expected transfection efficiencies: the time point chosen to evaluate gene expression and the high stability of the synthetized complexes.

Despite the demonstrated evidence for polyplexes internalization and probable endosomal escape within 24h, it was also seen that this process is slow (Figure 23) and thus, this time point might not have been the optimal to assess the effect of these sequences. Slow internalization and lysosomal escape of chitosan nanoparticles has also been reported elsewhere [105]. In fact, other reports assessing gene knockdown through sequences delivered by TMC-based polyplexes used a 48h time point to evaluate transfection efficiency [93,101].

The high stability of the complexes is also a possible reason for their ineffectiveness, correlated with the above mentioned time necessary to evaluate transfection results. A study of Thibault *et al.* demonstrated that chitosan decondensation kinetics is a determinant factor to achieve good transfection efficiencies [105]. These authors did not observe a relationship between cellular uptake and transfection efficiency, which was attributed to the overly stability of some of the formulations used that did not allow pDNA release.

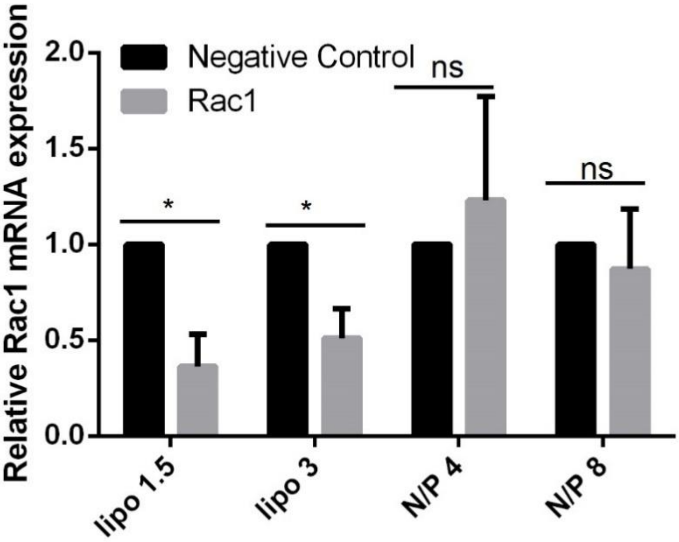

Figure 27 Rac1 mRNA expression on cells transfected with Rac1 or negative control siRNAs, 24h post-transfection (200nM siRNA). Transfection performed with TMC polyplexes (N/P 4 and N/P 8) and with lipofectamine (lipo). The values of Rac1 expression were quantified with real-time PCR and normalized to the housekeeping gene, cyclophilin (n=3). *p<0.05, ns=non-significant.

In another study, discrepancies between cellular uptake and knockdown efficiencies were also found [86], further supporting that cellular uptake is not always correlated with transfection efficiency and therefore other factors must be addressed. Dehousse *et al.* attributed the low transfection efficiency obtained with TMC polyplexes to the high stability, that could result in low or delayed transfection [77]. Accordingly, the incorporation of a negatively charged poly(Y-glutamic acid) in chitosan/siRNA complexes in order to promote complex unpackage in the cellular cytoplasm, facilitating siRNA release, resulted in an accelerated gene knockdown [106].

All these studies emphasize the importance of a balance between protection and release for siRNA biological functionality. Regarding the low molecular weight of TMC used and the relatively low N/P ratios herein tested, it may appear surprising the synthesis of complexes with this high stability [105]. Nevertheless, the formulation method also plays an important role on polyplex stability [74]. The coarcervation method used, aided by sodium sulfate, strengthens interaction between siRNA and polymer, conferring extra stabilization to these TMC complexes [80,93]. Also, the use of TMC, which is a chitosan-derivative with permanent positive charges, is, *per se*, associated with the obtainment of very stable nanoparticles [77,87]. This may justify the absence of efficient mRNA downregulation for both N/P 4 and N/P 8.

Bearing all this in mind, it can be postulated that a later assessment of gene expression or a different method of nanoparticle synthesis could have been beneficial to achieve gene knockdown in the present study. Moreover, the evaluation of endosomal escape through endosome staining would give us more answers regarding the intracellular behavior of these complexes and, therefore, allow for a better understanding of the reasoning behind these results.

4.5.2. Rac1 knockdown effect in a neurotoxic context

In view of the results presented in the previous section, lipofectamine (ratio 1.5) was used to assess the effect of Rac1 knockdown when cells are submitted to a neurotoxic stimulus. Based on the studies of Rac1 expression in HT22 and on the data from the cells response to toxic stimulus, H_2O_2 was used to a final concentration of 600 µM. After a 4h treatment with H_2O_2, PI staining was employed to evaluate cellular death. Stained cells images as well as PI fluorescence quantification are presented in Figure 28A and Figure 28B, respectively. Cells response to H_2O_2 was evaluated 28h after transfection due to relatively short half-life of Rac1 (approximately 4h) [107]. In fact, a pivotal study for the demonstration of Rac1 knockdown therapeutic effect in brain ischemia, assessed Rac1 protein levels 24h after ASOs administration and verified a notorious reduction of protein expression [54]. Results show a significant decrease of cell death on cells transfected with Rac1 siRNA. This data corroborates the hypothesis of the present thesis, showing evidence for a therapeutic effect of Rac1 silencing in the HT22 cell line. The verified neuroprotection occurred likely due to the interference with the three pathways depicted on Figure 3, which include JNK apoptotic pathway activation, dendritic spine growth and Nox activation. Nevertheless, attending to the fact that H_2O_2 mimics the ROS species produced during ischemia [99,100], this effect may have occurred mainly due to the impediment of further ROS production, which exacerbates the damage caused to cells as verified for the negative control. By avoiding Nox activation [23,52,55], Rac1 knockdown may thus circumvent the elevation of ROS levels to values that compromise cells viability. This premise is supported by the increased Rac1 expression following H_2O_2 toxicity (Figure 14). Importantly, protection against oxidative stress through Rac1 knockdown seems also to be correlated with a modulation of antioxidant enzymes activity [54], which can also support these findings.

Further than mimicking ROS production during the ischemic cascade, H_2O_2 represents here a source of oxidative stress. Thus, this compound aims to mimic a step of the ischemic cascade where the lactic acid-induced acidosis upon oxygen deprivation, lead to oxidative stress, as well as the already described reperfusion effect. All these phenomena culminate with the initiation of pathways that ultimately lead to cell death [11]. Interestingly, HT22 cells treatment with endogenous cannabinoid anandamide was found to promote cytoprotection against oxidative stress induced by H_2O_2, through Nox2 inhibition [99]. These results are consistent with the data here presented once the same cell line and stress stimulus were used along with the fact that Nox activation is intimately correlated to Rac1 expression.

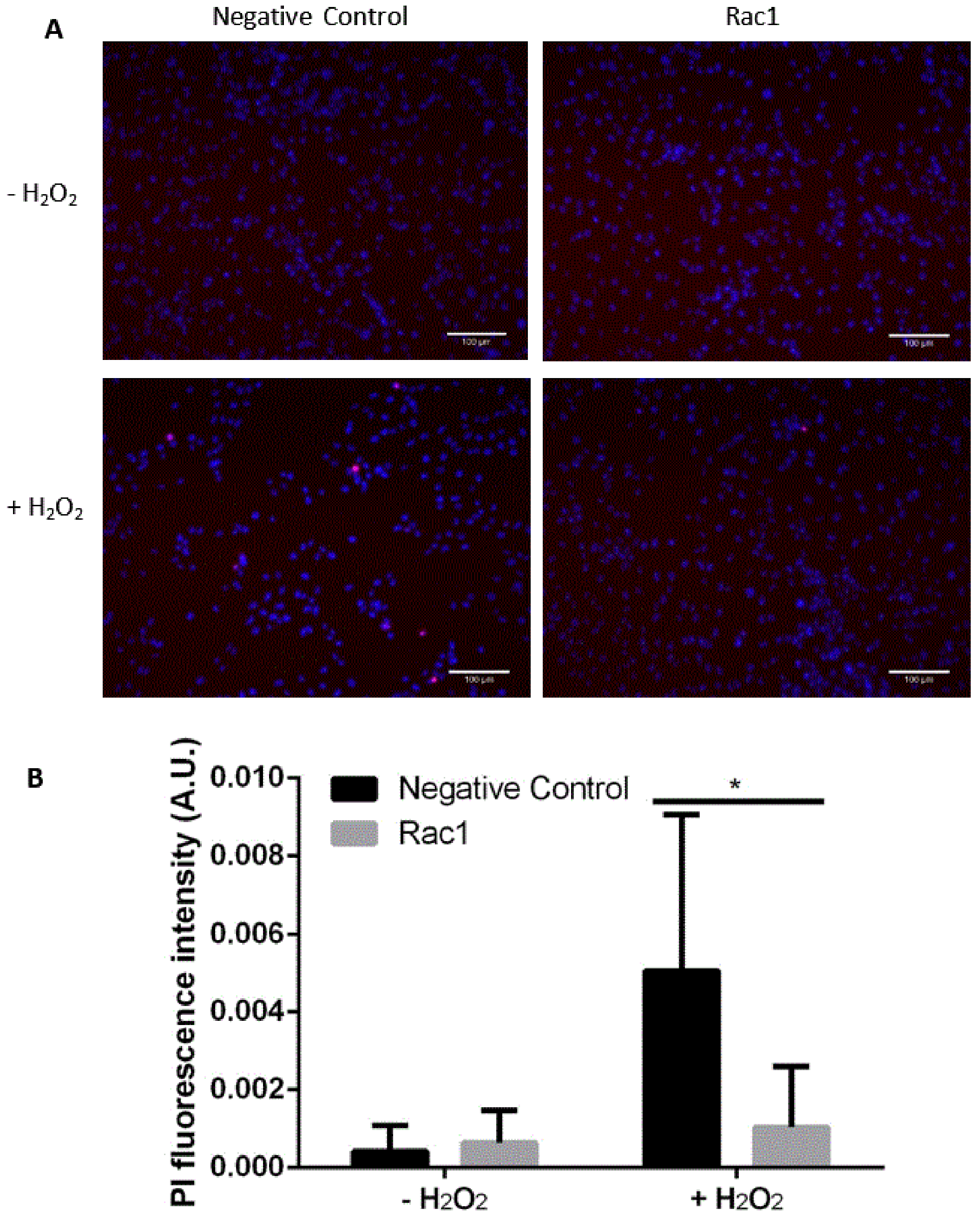

Figure 28 PI and Hoechst staining of cells transfected with Rac1 or negative control siRNAs (200nM), following treatment with H_2O_2. Non-treated cells used as control (-H_2O_2). (A) Representative images of the different conditions. (B) PI fluorescence intensity quantification. Values are normalized to Hoechst fluorescence intensity. Data from single experiment. 6 pictures taken with the 20x objective were analysed per condition. * $p<0.05$, unpaired t-test was employed. A.U.=arbitrary units. Scale bar is 100µm.

It is important to mention that another approaches, such as TUNEL and/or annexin V staining, cleaved caspase 3 protein levels assessment, Nox immunocytochemistry, ROS levels measurements, among other much used methodologies [52,54,55,60], could have been employed to reinforce these data.

Overall, these results confirmed a detrimental role of Rac1 protein following an oxidative stress insult and highlighted the HT22 cell line as a good model to mimic the Rac1 contribution to brain ischemia events *in vivo* [52,54].

4.6. TMC polyplexes *in vivo* administration

In vivo studies with TMC polyplexes were performed in order to verify complexes ability to reach the mice brain. The main aim of these studies was to ascertain the possibility to deliver Rac1 siRNA to an ischemic brain as a neuroprotective therapy, using TMC as siRNA carrier. Intranasal route was chosen for complexes administration due to TMC mucoadhesion and permeation properties [70,72,82,83]. Thus, it was expected that this route could allow for a direct delivery to the brain [83,90], using lower quantities of therapeutic molecules compared to routine delivery and simultaneously avoiding polyplexes delivery to other organs. Intranasal administrations were performed with 15µg of siDNA per mice using TMC_{ROX} at a N/P ratio of 4, since this ratio has a low size after lyophilisation (256 nm) and low PDI, both accetable for this purpose (Figure 16A and Figure 16B). Different organs were collected 4h after administration. As a positive control, commercially available carboxylate modified polystyrene fluospheres (200 nm diameter) were administered (0.1 mg per animal, which corresponds to the TMC mass used for N/P 4 TMC polyplexes). These fluospheres were chosen due to the similar size in comparison to the TMC complexes. Though, it is important to refer the different chemistry of these particles, which contrary to TMC possess a negative charge [108,109]. Consequently, it is predictable a different interaction with the nasal mucosa. Nevertheless, an acceptable mucus penetration was expected according to a report of McGill and Smyth [109].

Freeze-drying (FD) was initially used to concentrate the polyplexes in order to obtain a volume compatible with intranasal administration. In subsequent studies ultrafiltration (UF) was used. Furthermore, as previously explained, a high concentration nanocomplexes formulation (in which complexes synthesis occurred in a 4-fold lower final volume but maintaining the total amount of polyplexes) was also tested. Representative images of tissue sections reveal the presence of complexes agglomerates in different regions of the brain (OB, cortex and meninges), though in low amount (Figure 29A). By FD concentration no nanoparticles were seen in the OB for normal synthesis, while with a high concentration nanocomplexes synthesis, nanoparticles were found in some areas of the glomerular layer (GL) and also on the adjacent layer (external plexiform layer, EPL), indicating that complexes do not remain only in the more external regions of OB. DAPI nuclei staining enabled the distinction of the GL, characterized by round-shaped organizations [82]. UF was performed only in the high concentration synthesis as these polyplexes gave the best results in the FD strategy. By UF, a higher intensity of TMC_{ROX} was found in OB and particles did also migrate to the interior mitral cell layer (MCL) of this brain region, suggesting that this methodology is more efficient than FD. Polystyrene fluoshperes were also

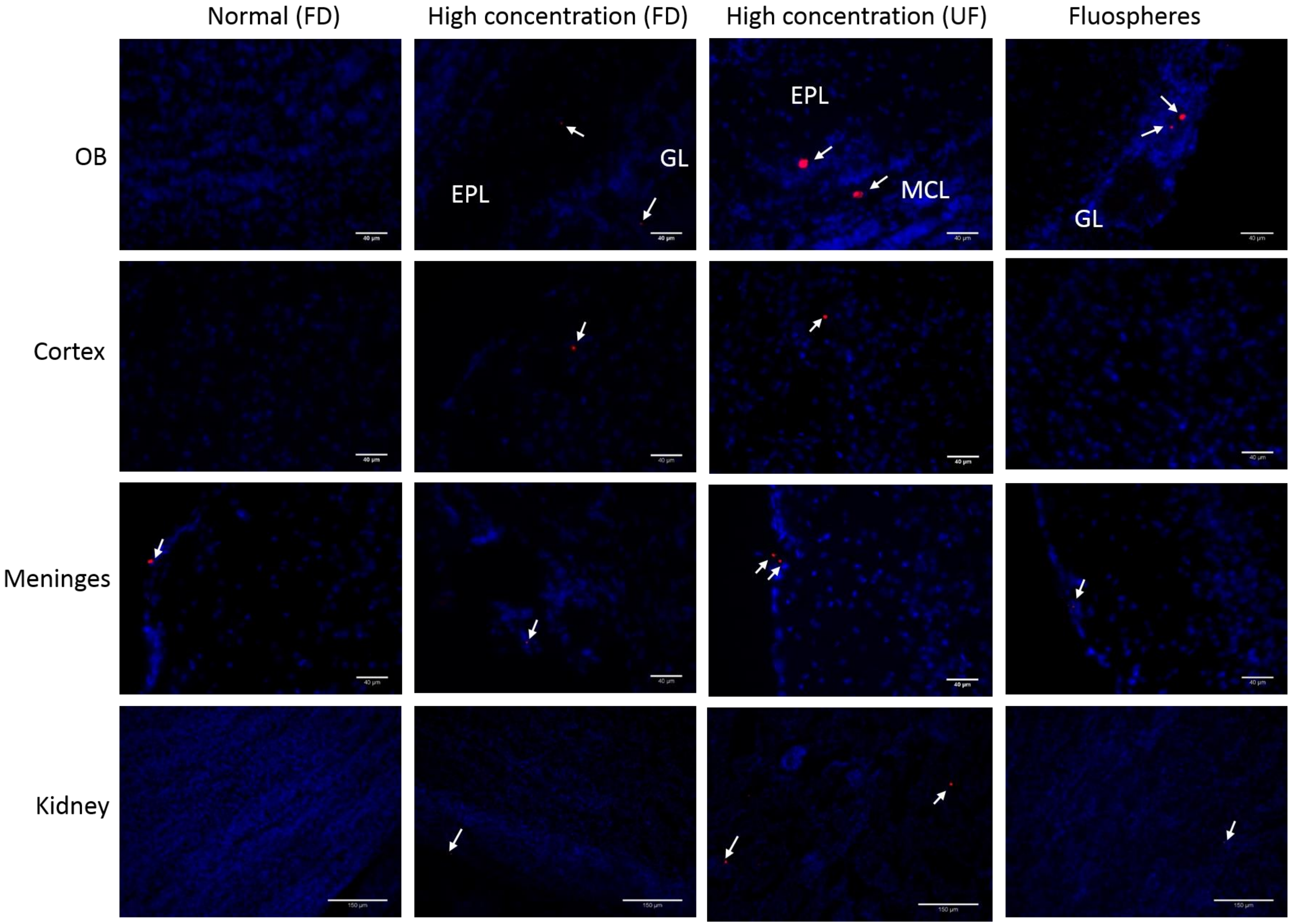
Normal (FD)
High concentration (FD)
High concentration (UF)
Fluospheres
OB
Cortex
Meninges
Kidney
EPL
GL
EPL
MCL
GL
40 µm
150 µm

Figure 29 Fluorescence microscopy images of different brain regions (OB, cortex and meninges) and kidney, 4h after TMC_{ROX} complexes administration. Particles localization is highlighted (white arrows). Nuclei in blue (DAPI). TMC_{ROX} in red. OB= olfactory bulbs; FD=freeze-drying; UF=ultrafiltration; GL=glomerular layer; EPL=external plexiform layer; MCL=mitral cell layer. Scale bar for OB, cortex and meninges is 40µm. Scale bar for kidney is 150µm.

found at similar levels than TMC particles concentrated through UF, in OB, although mainly in the GL. Interestingly, complexes were also visualized in the cortex for FD and UF with UF showing particles in more areas, however still in very few localizations, in general. Moreover, particles were seen in all the conditions at the brain tissue borders (meninges).

Nanoparticles localization in the OB suggests that both TMC complexes and fluospheres are transported via the olfactory pathway. Although fluospheres have a negative charge, these particles can form multiple hydrophobic adhesive interactions with mucin fibers, the principal components of the mucus, which promotes their adherence to mucus [108]. Furthermore, the permeation effect enabled by these particles is reported, being attributed to their capability to disturb the mesh network of the mucus barrier [109]. These features may justify the fact that these fluospheres reached the OB in similar levels to TMC. Differences between the different conditions (normal vs high concentration and FD vs UF) occurred likely due to lower losses of particles during the concentration procedure. Thus, it can be concluded that UF is the best choice for particles concentration. The fact that TMC particles were found at the mice cortex indicates that particles are probably diffused in the brain parenchyma within 4h. Nevertheless, it is important to refer that the amount in the cortex is very low. Yet, control fluospheres do not reach the cortex which may indicate an advantage of TMC over these particles. Finally, the existence of nanoparticles on meninges suggests a paracellular transport, from which particles achieve the CSF circulation and can be deposited in the external brain membrane. Indeed, a report using modified nano-micelles for intranasal delivery of siRNA to brain verified an increase of particles concentration on CSF in the first hour after administration [110], reinforcing that this is a possible route that can be followed by intranasally administered nanoparticles. Also, attending to the well-known permeation properties of chitosan and TMC, which open tight junctions allowing the transport across mucosa, the paracellular transport of TMC was already predicted [78,83]. Caudal parts of the brain were not addressed here and thus images of the cortex and meninges correspond to brain regions anterior to hippocampus.

In order to evaluate whether the administered particles reached systemic circulation, the kidney was also assessed (Figure 29B). Minimal amounts of particles were found in this organ. For the condition of normal synthesis, no nanoparticles were seen, which is consistent with the hypothesis that some particles were lost during the concentration procedure and therefore less complexes were administered to this mouse. Complexes concentrated through UF were found in higher quantities, which is also in line with a possible higher nanoparticles administration in comparison to the complexes concentrated by FD.

To sum up, with this first approach, TMC_{ROX} particles could be found in the brain, but only in very low levels. Possible reasons for this result are: (1) particles clearance from the mucus; (2)

insufficient complexes quantity [90]; (3) nanocomplexes aggregation after concentration, as verified by others [72] or (4) particles strong adherence to the mucus abolishing the polyplexes penetration [108]. In order to evaluate the last hypothesis, the nasal mucosa was analysed after TMC_{ROX} complexes administration (concentrated through UF) (Figure S 5). It was found that particles were indeed deposited along the mucosa surface even 4h after administration, which could be contributing to the low delivery to the brain.

Another approach was thus followed aiming at increasing nanocomplexes capability to migrate further into the brain tissue. The strategy consisted on the linkage of 5kDa PEG chains to the TMC polymer previously modified with thiol groups. PEGylated chitosan has been shown to exhibit a potent tight junction opening effect, which was actually found to be considerably larger than that of unmodified chitosan [111]. One of the possible reasons, pointed by the authors, was that PEG promoted the diffusion of particles, overcoming the pronounced interaction of unmodified chitosan with the mucus. An additional feature that makes PEGylation advantageous is the enhancement of complexes stability, which results in an improved biological function at the target site [108] and the reduction of inter-particle aggregation [70,80], which may minimize complexes aggregation following concentration. Moreover, PEGylated chitosan complexes are reported to be less toxic in comparison with unmodified complexes [111].

For studies with PEGylated TMC, siDNA tagged with the cy5 fluorochrome ($siDNA_{cy5}$) was used to detect the complexes, formed at the N/P ratio 8 and concentrated through UF. This N/P ratio was employed due to its low size (Figure 16E) along with the high level of cellular internalization (Figure 21 and Figure 22). As previously mentioned, two different percentages of the TMC thiolated groups were modified with PEG (25 and 75%) and the performance of both complexes was evaluated *in vivo*. It is important to highlight that in previous studies the TMC was fluorescently labelled, while here siDNA sequences were fluorescently labelled. Moreover, the fluorochromes used were different. Therefore, the fluorescence intensity cannot be compared between experiments.

Analysis of the brain tissue revealed that 75% PEG formulation reached the different brain regions and this occurred in higher amounts than with the 25% PEG formulation (Figure 30A). In OB, TMC-PEG-75 was found in the olfactory nerve layer (ONL), GL (the latter is not shown in the image) and also in the more internal layers (EPL and granule cell layer), although to a lesser extent (not shown). Regarding TMC-PEG-25, this was found mainly in GL. There were very few particles on the brain cortex for TMC-PEG-75, similarly to what occurred for non-PEGylated complexes, whereas with TMC-PEG-25 no particles were found in the cortex.

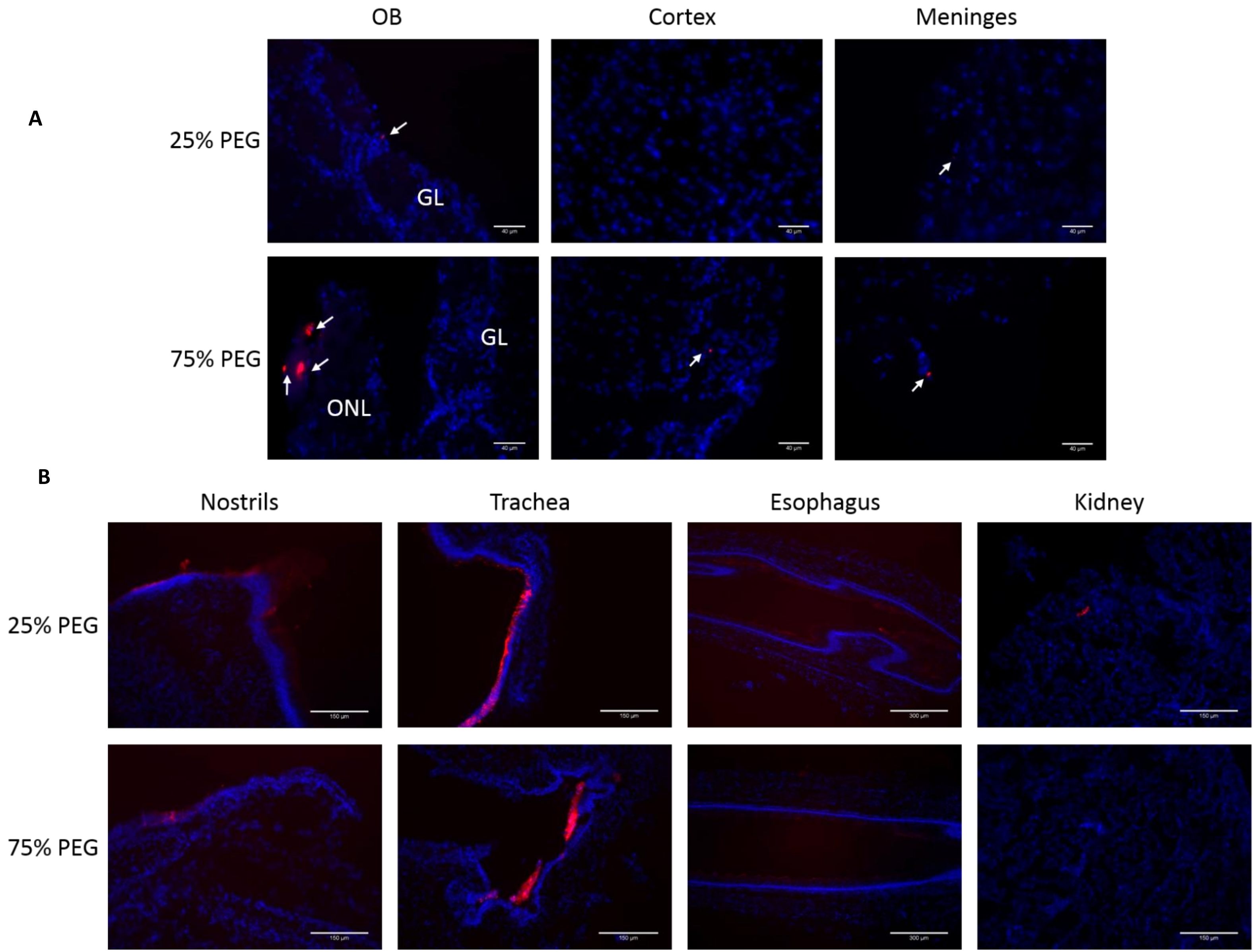
A
OB
Cortex
Meninges
25% PEG
75% PEG
GL
GL
ONL
40 µm
B
Nostrils
Trachea
Esophagus
Kidney
25% PEG
75% PEG
150 µm
300 µm

Figure 30 Fluorescence microscopy images of mice organs 4h after TMC-PEG-siDNA$_{cy5}$ complexes intranasal administration, with two different percentages of TMC$_{SH}$ PEGylation. (A) Different regions of the brain (OB, cortex and meninges) were analysed. White arrows highlight particles localization (B) Nasal mucosa, trachea, esophagus and kindey were also evaluated. Nuclei in blue (DAPI). siDNA$_{cy5}$ is represented in red. OB= olfactory bulbs; ONL=olfactory nerve layer; GL=glomerular layer. Scale bar for OB, cortex and meninges is 40µm. Scale bar for nostrils, trachea and kidney is 150µm. Scaler bar for esophagus is 300µm.

In the meninges, analysis of different tissue sections clearly demonstrated a higher amount of particles for TMC-PEG-75. These results suggest a higher transport of TMC-PEG-75 complexes through the olfactory pathway. When comparing with non-PEGylated TMC, a general increase on particles reaching the brain was observed for PEGylated nanoparticles. Nevertheless, we consider that the quantity of PEGylated complexes reaching the brain was still below the desired levels.

To ascertain whether these PEGylated particles were actually promoting an improvement on complexes penetration through nasal mucosa, this tissue was also assessed (Figure 30B, nostrills). In fact, it was evident the existence of lower quantities of particles attached to the nasal mucosa of mice in which TMC-PEG-75 was administered, in accordance with the finding that higher quantities of this particles formulation reach the brain OB and meninges. These results are in agreement with the work of Wang *et al.* that showed a big improvement on nanoparticles diffusion through the mucus when a low molecular weight PEG and high density of PEG molecules were used. The authors attributed their observations to the mucoinert characteristics of these particles. Using short PEG chains, intermolecular interactions with mucins were avoided while the high PEG coverage prevented hydrophobic interactions between the polystyrene core and the mucins [112]. Transposing this finding to the results presented herein, the better results achieved with 75% PEG might be attributed to the fact that covering a bigger area of the TMC nanocomplex conferred a weaker adherence of TMC to the mucus, enabling the transport of complexes across this barrier towards the olfactory nerves.

Although an improvement over the previous results was seen, the amount of particles reaching the brain was far from the desirable quantities to use for the delivery of a therapeutic agent. In order to evaluate if particles were lost to the respiratory and digestive system, trachea and esophagus were also evaluated (Figure 30B). High amounts of nanocomplexes were seen on the trachea of both types of PEGylated TMC, which may justify the low quantities found in the brain. On the other hand, low intensity cy5 was found in the esophagus with the lowest amount for TMC-PEG-75 in comparison with TMC-PEG-25.

Finally, nanoparticles leakage to the circulatory system was again evaluated in kidney (Figure 30B). Nanoparticles with the highest PEGylation degree did not accumulate in the kidney whereas particles with 25% PEG appeared in some few areas of the tissue. These results suggest a higher renal clearance and/or a lower leakage to the circulatory system of particles with higher PEG content. It is reasonable to accept that the higher PEG percentage promoted a more effective avoidance of protein adsorption, which is beneficial for renal clearance.

To verify whereas intravenous administration could confer an advantage on the transport to brain, fluospheres were administered to mice (0.1 mg intrnasally plus 0.4 mg intravenously).

Additionally, the capability of particles with 200 nm to bypass the BBB could also be addressed in this experiment. A general analysis of the brain tissue showed that this approach led to the appearance of more particles in the different brain regions analysed when comparing with results from particles only administered intranasally. This trend can be observed in Figure 31A. Furthermore, it could be noted that fluospheres were likely reaching the cortex through blood capillaries, which is supported by the linear track followed by particles to more internal parts of the cortex (Figure 31B). Nevertheless, an endothelial immunostaining would be needed to confirm this hypothesis. Regarding particles accumulations in the kidney (Figure 31C), a greater extent of particles was found when compared with particles solely administered through nose (Figure 29). Thus, it can be concluded that intravenous administration together with the intranasal administration can actually allow for the transport of higher particles quantities to the brain, 4h after administration. However, much higher particles quantities seem to be needed to reach this organ. Although the intravenous administration of lower amounts of particles was not tested, it is known from the literature that hepatic removal, glomerular filtration, serum degradation and the BBB account for a big reduction on particles transport to the brain [72,75,90].

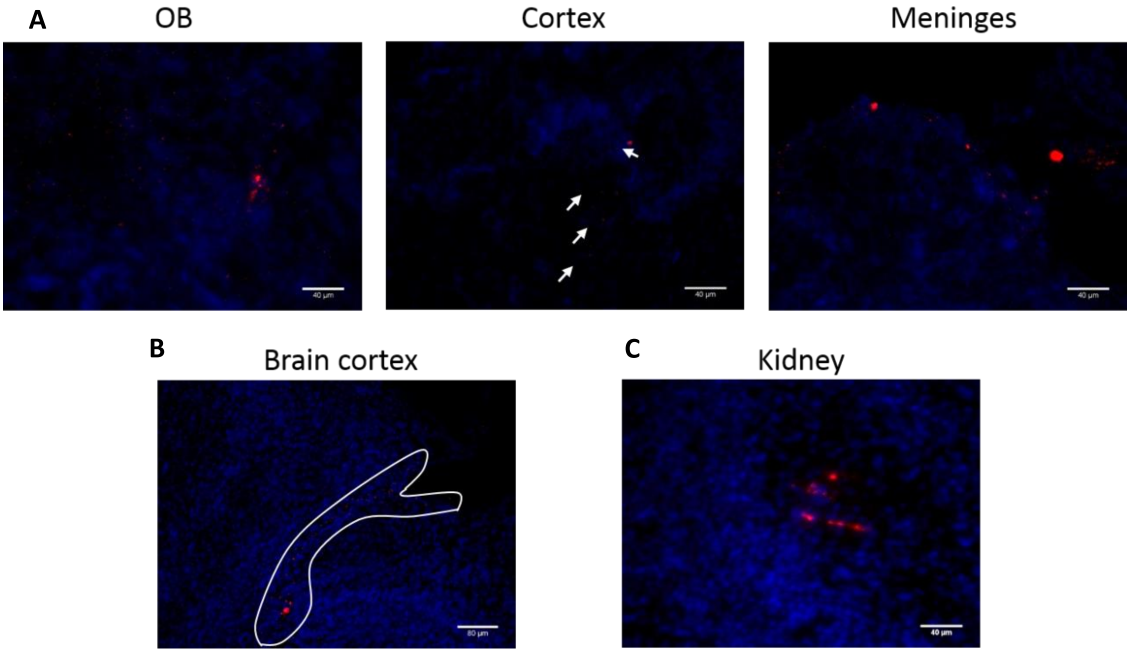

Figure 31 Fluorescence microscopy images of mice organs 4h after fluospheres simultaneous intranasal and intravenous administration. (A) Different regions of the brain (OB, cortex and meninges) were analysed. OB= olfactory bulbs (B) Particles linear track in the brain cortex. White surrounding line highlights the path followed by fluospheres. (C) Kidney accumulation of fluospheres. Nuclei in blue (DAPI). Fluospheres are represented in red.

Furthermore, it has to be taken into consideration that the data obtained here results from a conjugation between particles arrival through intravenous and intranasal routes.

In order to quantify the particles distribution through the different organs and brain regions, a method based on fluorimeter analysis of tissue homogenates was employed. After intranasal administration of 0.2 µm fluospheres, fluorescence was measured in organ homogenates (Figure 32). The only organ in which fluorescence was detected was the nose. The other analyzed organs showed negligible fluorescence, i.e., values that were very close to the blank, which highlights the insufficient sensitivity of the method to detect the low quantities of fluospheres seen by imaging. Additionally, it can be noticed that the amount of particles found in the nose, 4h after administration, is higher than what was verified after 1h. Although this was not expected, it may have occurred due to possible higher losses of the particles to outside of the nose caused by mucociliary clearance, on 1h condition. Nevertheless, a larger number of animals should be analyzed in order to take further conclusions regarding the two time points. Also, it should be noted that only a percentage inferior to 1% of the administered complexes was detected in the mice nose, which seems a very low value even attending to possible losses and to the fact that particles can be distributed in other organs, such as the liver. Owing to the very low levels of particles detected through this methodology, no further efforts were made using this approach. In this regard, it is important to notice that a similar method had been successfully employed by other authors [110], however their study used nanoparticles complexed to alexa-dextran, which likely enabled the emission of a brighter signal, increasing the sensitivity of the method.

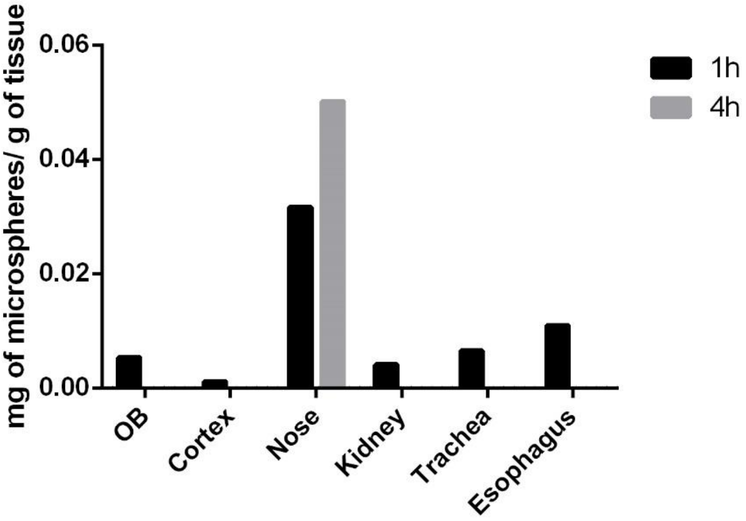

Figure 32 Fluospheres distribution in different tissues 1 and 4h after intranasal administration (0.2mg). OB= olfactory bulbs

In sum, the data presented in this section provided evidence for a direct brain transport of TMC nanocomplexes after nasal administration. Even though an improvement on brain targeting was achieved with PEGylation, there is still a clear need for an enhancement on the complexes features in order to deliver enough quantities of Rac1 siRNA to promote a therapeutic effect after stroke. Future studies should address an optimization of the particles features, the administration of higher amounts of polyplexes and, also, the evaluation of particles tropism to the lesion site after stroke. In later stages of these studies, other important issues must be evaluated, such as the inclusion of specific targeting ligands for neurons and the evaluation of the mice recovery from brain ischemia after therapy application.

Finally, it is worth mentioning that this TMC complexes were able to transfect cells, but unable to deliver siRNA after internalization likely due to their high intracellular stability. However, the polyplexes stability is highly desirable for the *in vivo* experiments. Thus, after accomplishing successful ways to achieve gene silencing with these complexes, a conjugation of their biological function with the stability properties is highly desirable to achieve gene knockdown in neurons. With this in mind, these studies can represent the first steps towards a potential translation of the *in vitro* findings with Rac1 knockdown to an *in vivo* study, in which Rac1 siRNA sequences could be delivered to an ischemic brain as a neuroprotective therapy, using TMC as a carrier.

Chapter 5

Concluding Remarks and Future Perspectives

Our initial analysis in HT22 neuronal cell line showed an increased expression of Rac1 after a cytotoxic treatment with glutamate or H_2O_2, with a maximal increase obtained with H_2O_2. This last treatment mimicked the oxidative stress experienced by neuronal cells in ischemic conditions. Future studies should also address the levels of the active protein (Rac1-GTP) in order to ascertain whether this increased expression is correlated with an altered activity of the protein. These results confirmed the appropriate use of these cells to further perform Rac1 loss-of-function analysis.

TMC nanoparticles synthetized with siDNA or siRNA sequences presented sizes compatible with cell transfection, low PDI, positive values of zeta potential and high stability. These complexes were also able to efficiently protect sequences against nucleases degradation. Furthermore, no toxicity was found in HT22 cells after incubation with these particles. Regarding complexes cellular internalization, successful nanoparticles uptake was verified for siDNA and siRNA for the N/P ratios 4 and 8, while N/P 8 showed better results.

Although TMC-siRNA nanoparticles were found in neuronal cells *in vitro*, gene expression analysis revealed no reduction on Rac1 expression, while lipofectamine significantly reduced the gene expression. This may be attributed to the very high stability of TMC complexes, which did not allow siRNA intracellular release. Furthermore, endosomal escape of these nanoparticles was not proved, which can also explain the obtained results. Thus, further modifications of the particles could improve the transfection outcomes. In this regard, the incorporation of negatively charged components, such as hyaluronic acid, which help on the structural unpackaging of the complexes enabling siRNA dissociation from the complex, may be an advantage. Also, TMC combination with endosome-disrupting agents could allow for better outcomes.

Rac1 silencing in HT22 cell line, with lipofectamine, promoted a significant decrease on neuronal death, after H_2O_2 treatment. Thus, evidence was provided for the injurious role of Rac1 following the oxidative stress that is patent during the ischemic cascade. Nevertheless, further studies should be performed to corroborate these results. Furthermore, different methods could be used to evaluate earlier stages of cell death, such as TUNEL or annexin V staining.

Finally, it was shown that intranasally administered TMC complexes could reach the mice brain, however this occurred in very low amounts. PEGylation of the TMC enhanced the transport to the brain but there is still a need for improvements in order to proceed to RNAi therapy application in a mice stroke model. Future studies should ascertain these findings using a higher number of animals per condition. A suitable method for particles quantification should also be established. Additionally, as PEGylation was shown to be beneficial for the transport to the brain, further increasing PEG density on TMC surface (which would imply the use of polymers with higher thiol modification), or even studying the effect of different PEG M_w, can be potential strategies to employ in upcoming studies.

In summary, in the present work, TMC nanoparticles with appropriate physicochemical properties were obtained and delivered to neuronal cells. However further improvements on nanoparticles features are required to enhance their performance *in vitro* and *in vivo*. In addition, Rac1 gene silencing as a potential therapeutic target for neuroprotection, in oxidative stress conditions characteristic of brain ischemia, was highlighted.

References

1. Doyle KP, Simon RP, Stenzel-Poore MP. Mechanisms of ischemic brain damage. *Neuropharmacology* 2008; 55: 310-318.
2. Majid A. Neuroprotection in stroke: past, present, and future. *ISRN neurology* 2014; 2014.
3. Onwuekwe IO, Ezeala-Adikaibe B. Ischemic stroke and neuroprotection. *Annals of medical and health sciences research* 2013; 2: 186-190.
4. Posada-Duque RA, Barreto GE, Cardona-Gomez GP. Protection after stroke: cellular effectors of neurovascular unit integrity. *Frontiers in cellular neuroscience* 2014; 8.
5. Cipriani R, Domercq M, Matute C. Ischemia and Stroke. Microglia in Health and Disease: Springer; 2014. p. 413-435.
6. Uchino H, Chijiiwa M, Ogihara Y, Elmer E. Molecular Mechanisms of Brain Ischemia and Its Protection. Neuroanesthesia and Cerebrospinal Protection: Springer; 2015. p. 39-51.
7. Candelario-Jalil E. Injury and repair mechanisms in ischemic stroke: considerations for the development of novel neurotherapeutics. *Curr Opin Investig Drugs* 2009; 10: 644-654.
8. Mozaffarian D, Benjamin EJ, Go AS, Arnett DK, Blaha MJ, Cushman M, de Ferranti S, Despres J-P, Fullerton HJ, Howard VJ. Heart disease and stroke statistics-2015 update: a report from the american heart association. *Circulation* 2015; 131: e29.
9. Edvinsson L, Krause DN. Cerebral Blood Flow and Metabolism. Lippincott Williams & Wilkins; 2002.
10. Kleikers PW, Wingler K, Hermans J, Diebold I, Altenhöfer S, Radermacher K, Janssen B, Görlach A, Schmidt H. NADPH oxidases as a source of oxidative stress and molecular target in ischemia/reperfusion injury. *Journal of molecular medicine* 2012; 90: 1391-1406.
11. Manzanero S, Santro T, Arumugam TV. Neuronal oxidative stress in acute ischemic stroke: sources and contribution to cell injury. *Neurochemistry international* 2013; 62: 712-718.
12. Lo EH. A new penumbra: transitioning from injury into repair after stroke. *Nature medicine* 2008; 14: 497-500.
13. Moretti A, Ferrari F, Villa RF. Neuroprotection for ischaemic stroke: Current status and challenges. *Pharmacology & therapeutics* 2015; 146: 23-34.
14. Minnerup J, Sutherland BA, Buchan AM, Kleinschnitz C. Neuroprotection for stroke: current status and future perspectives. *International journal of molecular sciences* 2012; 13: 11753-11772.
15. ElAli A, Doeppner TR, Zechariah A, Hermann DM. Increased Blood–Brain Barrier Permeability and Brain Edema After Focal Cerebral Ischemia Induced by Hyperlipidemia Role of Lipid Peroxidation and Calpain-1/2, Matrix Metalloproteinase-2/9, and RhoA Overactivation. *Stroke* 2011; 42: 3238-3244.
16. Jaffe AB, Hall A. Rho GTPases: biochemistry and biology. *Annu Rev Cell Dev Biol* 2005; 21: 247-269.
17. Garcia-Mata R, Boulter E, Burridge K. The'invisible hand': regulation of RHO GTPases by RHOGDIs. *Nature reviews Molecular cell biology* 2011; 12: 493-504.
18. Heasman SJ, Ridley AJ. Mammalian Rho GTPases: new insights into their functions from in vivo studies. *Nature reviews Molecular cell biology* 2008; 9: 690-701.
19. Hall A. Rho family GTPases. *Biochemical Society Transactions* 2012; 40: 1378.
20. Rossman KL, Der CJ, Sondek J. GEF means go: turning on RHO GTPases with guanine nucleotide-exchange factors. *Nature reviews Molecular cell biology* 2005; 6: 167-180.
21. Tcherkezian J, Lamarche-Vane N. Current knowledge of the large RhoGAP family of proteins. *Biology of the Cell* 2007; 99: 67-86.

22. Hajdo-Milašinović A, Ellenbroek SI, van Es S, van der Vaart B, Collard JG. Rac1 and Rac3 have opposing functions in cell adhesion and differentiation of neuronal cells. *Journal of Cell Science* 2007; 120: 555-566.
23. Haruta M, Bush RA, Kjellstrom S, Vijayasarathy C, Zeng Y, Le Y-Z, Sieving PA. Depleting Rac1 in mouse rod photoreceptors protects them from photo-oxidative stress without affecting their structure or function. *Proceedings of the National Academy of Sciences* 2009; 106: 9397-9402.
24. Sandrock K, Bielek H, Schradi K, Schmidt G, Klugbauer N. The Nuclear Import of the Small GTPase Rac1 is Mediated by the Direct Interaction with Karyopherin α2. *Traffic* 2010; 11: 198-209.
25. Michaelson D, Abidi W, Guardavaccaro D, Zhou M, Ahearn I, Pagano M, Philips MR. Rac1 accumulates in the nucleus during the G2 phase of the cell cycle and promotes cell division. *The Journal of cell biology* 2008; 181: 485-496.
26. Linseman DA, Loucks FA. Diverse roles of Rho family GTPases in neuronal development, survival, and death. *Frontiers in bioscience: a journal and virtual library* 2008; 13: 657-676.
27. Hall A, Lalli G. Rho and Ras GTPases in axon growth, guidance, and branching. *Cold Spring Harbor perspectives in biology* 2010; 2: a001818.
28. Stankiewicz TR, Linseman DA. Rho family GTPases: key players in neuronal development, neuronal survival, and neurodegeneration. *Frontiers in cellular neuroscience* 2014; 8.
29. Govek E-E, Newey SE, Van Aelst L. The role of the Rho GTPases in neuronal development. *Genes & development* 2005; 19: 1-49.
30. McNair K, Spike R, Guilding C, Prendergast GC, Stone TW, Cobb SR, Morris BJ. A role for RhoB in synaptic plasticity and the regulation of neuronal morphology. *The Journal of Neuroscience* 2010; 30: 3508-3517.
31. Lamprecht R, LeDoux J. Structural plasticity and memory. *Nature Reviews Neuroscience* 2004; 5: 45-54.
32. Nimchinsky EA, Sabatini BL, Svoboda K. Structure and function of dendritic spines. *Annual review of physiology* 2002; 64: 313-353.
33. Carlisle HJ, Kennedy MB. Spine architecture and synaptic plasticity. *Trends in neurosciences* 2005; 28: 182-187.
34. Tejada-Simon MV, Villasana LE, Serrano F, Klann E. NMDA receptor activation induces translocation and activation of Rac in mouse hippocampal area CA1. *Biochemical and biophysical research communications* 2006; 343: 504-512.
35. Nakayama AY, Harms MB, Luo L. Small GTPases Rac and Rho in the maintenance of dendritic spines and branches in hippocampal pyramidal neurons. *The Journal of Neuroscience* 2000; 20: 5329-5338.
36. Brown CE, Li P, Boyd JD, Delaney KR, Murphy TH. Extensive turnover of dendritic spines and vascular remodeling in cortical tissues recovering from stroke. *The Journal of neuroscience* 2007; 27: 4101-4109.
37. Haditsch U, Anderson MP, Freewoman J, Cord B, Babu H, Brakebusch C, Palmer TD. Neuronal Rac1 is required for learning-evoked neurogenesis. *The Journal of Neuroscience* 2013; 33: 12229-12241.
38. Haditsch U, Leone DP, Farinelli M, Chrostek-Grashoff A, Brakebusch C, Mansuy IM, McConnell SK, Palmer TD. A central role for the small GTPase Rac1 in hippocampal plasticity and spatial learning and memory. *Molecular and Cellular Neuroscience* 2009; 41: 409-419.
39. Dietz DM, Sun H, Lobo MK, Cahill ME, Chadwick B, Gao V, Koo JW, Mazei-Robison MS, Dias C, Maze I. Rac1 is essential in cocaine-induced structural plasticity of nucleus accumbens neurons. *Nature neuroscience* 2012; 15: 891-896.

40. Lorenzetto E, Ettorre M, Pontelli V, Bolomini-Vittori M, Bolognin S, Zorzan S, Laudanna C, Buffelli M. Rac1 selective activation improves retina ganglion cell survival and regeneration. *PloS one* 2013; 8: e64350.
41. Li Q, Huang X-J, He W, Ding J, Jia J-T, Fu G, Wang H-X, Guo L-J. Neuroprotective Potential of Fasudil Mesylate in Brain Ischemia-Reperfusion Injury of Rats. *Cell Mol Neurobiol* 2009; 29: 169-180.
42. Rikitake Y, Kim H-H, Huang Z, Seto M, Yano K, Asano T, Moskowitz MA, Liao JK. Inhibition of Rho kinase (ROCK) leads to increased cerebral blood flow and stroke protection. *Stroke* 2005; 36: 2251-2257.
43. Wei X-E, Zhang F-Y, Wang K, Zhang Q-X, Rong L-Q. Fasudil Hydrochloride Protects Neurons in Rat Hippocampal CA1 Region through Inhibiting GluR6–MLK3–JNKs Signal Pathway. *Cell Biochem Biophys* 2014; 70: 415-421.
44. Semenova MM, Mäki-Hokkonen AM, Cao J, Komarovski V, Forsberg KM, Koistinaho M, Coffey ET, Courtney MJ. Rho mediates calcium-dependent activation of p38α and subsequent excitotoxic cell death. *Nature neuroscience* 2007; 10: 436-443.
45. Brabeck C, Mittelbronn M, Bekure K, Meyermann R, Schluesener HJ, Schwab JM. Effect of focal cerebral infarctions on lesional RhoA and RhoB expression. *Archives of neurology* 2003; 60: 1245-1249.
46. Allen C, Srivastava K, Bayraktutan U. Small GTPase RhoA and its effector rho kinase mediate oxygen glucose deprivation-evoked in vitro cerebral barrier dysfunction. *Stroke* 2010; 41: 2056-2063.
47. Kawasaki K, Yano K, Sasaki K, Tawara S, Ikegaki I, Satoh S-i, Ohtsuka Y, Yoshino Y, Kuriyama H, Asano T, Seto M. Correspondence Between Neurological Deficit, Cerebral Infarct Size, and Rho-Kinase Activity in a Rat Cerebral Thrombosis Model. *J Mol Neurosci* 2009; 39: 59-68.
48. Vesterinen HM, Currie GL, Carter S, Mee S, Watzlawick R, Egan KJ, Macleod MR, Sena ES. Systematic review and stratified meta-analysis of the efficacy of RhoA and Rho kinase inhibitors in animal models of ischaemic stroke. *Syst Rev* 2013; 2: 33.
49. Barberan S, McNair K, Iqbal K, Smith NC, Prendergast GC, Stone TW, Cobb SR, Morris BJ. Altered apoptotic responses in neurons lacking RhoB GTPase. *European Journal of Neuroscience* 2011; 34: 1737-1746.
50. Zhao J, Pei D-S, Zhang Q-G, Zhang G-Y. Down-regulation Cdc42 attenuates neuronal apoptosis through inhibiting MLK3/JNK3 cascade during ischemic reperfusion in rat hippocampus. *Cellular Signalling* 2007; 19: 831-843.
51. Marei H, Malliri A. Rac1 in human diseases: the therapeutic potential of targeting Rac1 signaling regulatory mechanisms. *Small GTPases* 2016: 1-25.
52. Raz L, Zhang Q-G, Zhou C, Han D, Gulati P, Yang L, Yang F, Wang R, Brann DW. Role of Rac1 GTPase in NADPH oxidase activation and cognitive impairment following cerebral ischemia in the rat. *PLoS One* 2010; 5: e12606.
53. Kahles T, Luedike P, Endres M, Galla H-J, Steinmetz H, Busse R, Neumann-Haefelin T, Brandes RP. NADPH Oxidase Plays a Central Role in Blood-Brain Barrier Damage in Experimental Stroke. *Stroke* 2007; 38: 3000-3006.
54. Meng S, Su Z, Liu Z, Wang N, Wang Z. Rac1 contributes to cerebral ischemia reperfusion-induced injury in mice by regulation of Notch2. *Neuroscience* 2015; 306: 100-114.
55. Nikolova S, Lee YS, Lee Y-S, Kim J-a. Rac1-NADPH oxidase-regulated generation of reactive oxygen species mediates glutamate-induced apoptosis in SH-SY5Y human neuroblastoma cells. *Free Radical Research* 2005; 39: 1295-1304.
56. Ozaki M, Deshpand SS, Angekow P, Bellan J, Lowenstein CJ, Dinauer MC, Goldschmidt-Clermont PJ, Irani K. Inhibition of the Rac1 GTPase protects against nonlethal ischemia/reperfusion-induced necrosis and apoptosis in vivo. *The FASEB Journal* 2000; 14: 418-429.

57. Zhang Q-G, Wang R, Han D, Dong Y, Brann DW. Role of Rac1 GTPase in JNK signaling and delayed neuronal cell death following global cerebral ischemia. *Brain Research* 2009; 1265: 138-147.
58. Gutiérrez-Vargas J, Castro-Álvarez JF, Velásquez-Carvajal D, Montañez-Velásquez MN, Céspedes-Rubio Á, Cardona-Gómez GP. Rac1 activity changes are associated with neuronal pathology and spatial memory long-term recovery after global cerebral ischemia. *Neurochemistry international* 2010; 57: 762-773.
59. Khan AA, Mao XO, Banwait S, DerMardirossian CM, Bokoch GM, Jin K, Greenberg DA. Regulation of hypoxic neuronal death signaling by neuroglobin. *The FASEB Journal* 2008; 22: 1737-1747.
60. Sawada N, Kim H-H, Moskowitz MA, Liao JK. Rac1 Is a Critical Mediator of Endothelium-Derived Neurotrophic Activity. *Science signaling* 2009; 2: ra10-ra10.
61. Gorlach A, Berchner-Pfannschmidt U, Wotzlaw C, Cool RH, Fandrey J, Acker H, Jungermann K, Kietzmann T. Reactive oxygen species modulate HIF-1 mediated PAI-1 expression: involvement of the GTPase Rac1. *THROMBOSIS AND HAEMOSTASIS-STUTTGART-* 2003; 89: 926-935.
62. Görlach A, Diebold I, Schini-Kerth VB, Berchner-Pfannschmidt U, Roth U, Brandes RP, Kietzmann T, Busse R. Thrombin Activates the Hypoxia-Inducible Factor-1 Signaling Pathway in Vascular Smooth Muscle Cells: Role of the p22phox-Containing NADPH Oxidase. *Circulation Research* 2001; 89: 47-54.
63. Hirota K, Semenza GL. Rac1 Activity Is Required for the Activation of Hypoxia-inducible Factor 1. *Journal of Biological Chemistry* 2001; 276: 21166-21172.
64. Zhang Q-G, Wang X-T, Han D, Yin X-H, Zhang G-Y, Xu T-L. Akt inhibits MLK3/JNK3 signaling by inactivating Rac1: a protective mechanism against ischemic brain injury. *Journal of Neurochemistry* 2006; 98: 1886-1898.
65. Blanco-Suarez E, Fiuza M, Liu X, Chakkarapani E, Hanley JG. Differential Tiam1/Rac1 activation in hippocampal and cortical neurons mediates differential spine shrinkage in response to oxygen/glucose deprivation. *J Cereb Blood Flow Metab* 2014; 34: 1898-1906.
66. Meller R, Thompson SJ, Lusardi TA, Ordonez AN, Ashley MD, Jessick V, Wang W, Torrey DJ, Henshall DC, Gafken PR. Ubiquitin–proteasome-mediated synaptic reorganization: a novel mechanism underlying rapid ischemic tolerance. *The Journal of Neuroscience* 2008; 28: 50-59.
67. Gisselsson L, Toresson H, Ruscher K, Wieloch T. Rho kinase inhibition protects CA1 cells in organotypic hippocampal slices during in vitro ischemia. *Brain research* 2010; 1316: 92-100.
68. Ruan Y-W, Lei Z, Fan Y, Zou B, Xu ZC. Diversity and fluctuation of spine morphology in CA1 pyramidal neurons after transient global ischemia. *Journal of Neuroscience Research* 2009; 87: 61-68.
69. Brown CE, Wong C, Murphy TH. Rapid Morphologic Plasticity of Peri-Infarct Dendritic Spines After Focal Ischemic Stroke. *Stroke* 2008; 39: 1286-1291.
70. Mao S, Sun W, Kissel T. Chitosan-based formulations for delivery of DNA and siRNA. *Advanced Drug Delivery Reviews* 2010; 62: 12-27.
71. Lai W-F, Lin MC-M. Nucleic acid delivery with chitosan and its derivatives. *Journal of Controlled Release* 2009; 134: 158-168.
72. Malhotra M, Tomaro-Duchesneau C, Saha S, Prakash S. Intranasal, siRNA Delivery to the Brain by TAT/MGF Tagged PEGylated Chitosan Nanoparticles. *Journal of Pharmaceutics* 2013; 2013: 10.
73. Raemdonck K, Vandenbroucke RE, Demeester J, Sanders NN, De Smedt SC. Maintaining the silence: reflections on long-term RNAi. *Drug discovery today* 2008; 13: 917-931.
74. Ragelle H, Vandermeulen G, Préat V. Chitosan-based siRNA delivery systems. *Journal of Controlled Release* 2013; 172: 207-218.

75. Howard KA, Rahbek UL, Liu X, Damgaard CK, Glud SZ, Andersen MO, Hovgaard MB, Schmitz A, Nyengaard JR, Besenbacher F, Kjems J. RNA Interference in Vitro and in Vivo Using a Chitosan/siRNA Nanoparticle System. *Mol Ther* 2006; 14: 476-484.
76. Alameh M, DeJesus D, Jean M, Darras V, Thibault M, Lavertu M, Buschmann MD, Merzouki A. Low molecular weight chitosan nanoparticulate system at low N: P ratio for nontoxic polynucleotide delivery. *Int J Nanomedicine* 2012; 7: 1399-1414.
77. Dehousse V, Garbacki N, Jaspart S, Castagne D, Piel G, Colige A, Evrard B. Comparison of chitosan/siRNA and trimethylchitosan/siRNA complexes behaviour in vitro. *International journal of biological macromolecules* 2010; 46: 342-349.
78. Mourya V, Inamdar NN. Trimethyl chitosan and its applications in drug delivery. *Journal of Materials Science: Materials in Medicine* 2009; 20: 1057-1079.
79. Alameh M, Jean M, DeJesus D, Buschmann MD, Merzouki A. Chitosanase-based method for RNA isolation from cells transfected with chitosan/siRNA nanocomplexes for real-time RT-PCR in gene silencing. *Int J Nanomedicine* 2010; 5: 473-481.
80. Mao H-Q, Roy K, Troung-Le VL, Janes KA, Lin KY, Wang Y, August JT, Leong KW. Chitosan-DNA nanoparticles as gene carriers: synthesis, characterization and transfection efficiency. *Journal of Controlled Release* 2001; 70: 399-421.
81. Ragelle H, Riva R, Vandermeulen G, Naeye B, Pourcelle V, Le Duff CS, D'Haese C, Nysten B, Braeckmans K, De Smedt SC. Chitosan nanoparticles for siRNA delivery: optimizing formulation to increase stability and efficiency. *Journal of Controlled Release* 2014; 176: 54-63.
82. Van Woensel M, Wauthoz N, Rosière R, Mathieu V, Kiss R, Lefranc F, Steelant B, Dilissen E, Van Gool SW, Mathivet T. Development of siRNA-loaded chitosan nanoparticles targeting Galectin-1 for the treatment of glioblastoma multiforme via intranasal administration. *Journal of Controlled Release* 2016; 227: 71-81.
83. Luppi B, Bigucci F, Cerchiara T, Zecchi V. Chitosan-based hydrogels for nasal drug delivery: from inserts to nanoparticles. *Expert opinion on drug delivery* 2010; 7: 811-828.
84. Fröhlich E. The role of surface charge in cellular uptake and cytotoxicity of medical nanoparticles. *Int J Nanomedicine* 2012; 7: 5577-5591.
85. Oh N, Park J-H. Endocytosis and exocytosis of nanoparticles in mammalian cells. *Int J Nanomedicine* 2014; 9: 51-63.
86. Malmo J, Sørgård H, Vårum KM, Strand SP. siRNA delivery with chitosan nanoparticles: Molecular properties favoring efficient gene silencing. *Journal of controlled release* 2012; 158: 261-268.
87. Thanou M, Florea B, Geldof M, Junginger H, Borchard G. Quaternized chitosan oligomers as novel gene delivery vectors in epithelial cell lines. *Biomaterials* 2002; 23: 153-159.
88. De Boer A, Gaillard P. Drug targeting to the brain. *Annu Rev Pharmacol Toxicol* 2007; 47: 323-355.
89. Rajadhyaksha M, Boyden T, Liras J, El-Kattan A, Brodfuehrer J. Current advances in delivery of biotherapeutics across the blood-brain barrier. *Current drug discovery technologies* 2011; 8: 87-101.
90. Wu H, Hu K, Jiang X. From nose to brain: understanding transport capacity and transport rate of drugs. *Expert opinion on drug delivery* 2008; 5: 1159-1168.
91. Lochhead JJ, Thorne RG. Intranasal delivery of biologics to the central nervous system. *Advanced drug delivery reviews* 2012; 64: 614-628.
92. Sittampalam G, Neely G, Arkin M, Auld D, Austin C. Assay Guidance Manual. Eli Lilly & Company and the National Center for Advancing Translational Sciences. 2004.
93. Moreno PM, Santos JC, Gomes CP, Varela-Moreira A, Costa A, Leiro V, Mansur H, Pêgo AP. Delivery of Splice Switching Oligonucleotides by Amphiphilic Chitosan-Based Nanoparticles. *Molecular pharmaceutics* 2016; 13: 344-356.

94. Curti E, Campana-Filho SP. Viscosity Behavior of Chitosan and N, N, N-Trimethylchitosan Chloride Salts in Acid-Free Aqueous Solution. *Journal of Macromolecular Science Part A: Pure and Applied Chemistry* 2006; 43: 555-572.
95. Muzzarelli RA. Colorimetric determination of chitosan. *Analytical biochemistry* 1998; 260: 255-257.
96. He M, Liu J, Cheng S, Xing Y, Suo WZ. Differentiation renders susceptibility to excitotoxicity in HT22 neurons. *Neural regeneration research* 2013; 8: 1297.
97. Sanderson TH, Raghunayakula S, Kumar R. Release of mitochondrial Opa1 following oxidative stress in HT22 cells. *Molecular and Cellular Neuroscience* 2015; 64: 116-122.
98. Kritis AA, Stamoula EG, Paniskaki KA, Vavilis TD. Researching glutamate–induced cytotoxicity in different cell lines: a comparative/collective analysis/study. *Frontiers in cellular neuroscience* 2015; 9: 91.
99. Jia J, Ma L, Wu M, Zhang L, Zhang X, Zhai Q, Jiang T, Wang Q, Xiong L. Anandamide protects HT22 cells exposed to hydrogen peroxide by inhibiting CB1 receptor-mediated type 2 NADPH oxidase. *Oxidative medicine and cellular longevity* 2014; 2014.
100. Xu H, Luo P, Zhao Y, Zhao M, Yang Y, Chen T, Huo K, Han H, Fei Z. Iduna protects HT22 cells from hydrogen peroxide-induced oxidative stress through interfering poly (ADP-ribose) polymerase-1-induced cell death (parthanatos). *Cellular signalling* 2013; 25: 1018-1026.
101. Sadio A, Gustafsson JK, Pereira B, Gomes CP, Hansson GC, David L, Pêgo AP, Almeida R. Modified-chitosan/siRNA nanoparticles downregulate cellular CDX2 expression and cross the gastric mucus barrier. *PloS one* 2014; 9: e99449.
102. Lee D-W, Powers K, Baney R. Physicochemical properties and blood compatibility of acylated chitosan nanoparticles. *Carbohydrate polymers* 2004; 58: 371-377.
103. De Jaeghere F, Allémann E, Feijen J, Kissel T, Doelker E, Gurny R. Freeze-drying and lyopreservation of diblock and triblock poly (lactic acid)–poly (ethylene oxide)(PLA–PEO) copolymer nanoparticles. *Pharmaceutical development and technology* 2000; 5: 473-483.
104. Carpenter JF, Pikal MJ, Chang BS, Randolph TW. Rational design of stable lyophilized protein formulations: some practical advice. *Pharmaceutical research* 1997; 14: 969-975.
105. Thibault M, Nimesh S, Lavertu M, Buschmann MD. Intracellular trafficking and decondensation kinetics of chitosan–pDNA polyplexes. *Molecular Therapy* 2010; 18: 1787-1795.
106. Liao Z-X, Ho Y-C, Chen H-L, Peng S-F, Hsiao C-W, Sung H-W. Enhancement of efficiencies of the cellular uptake and gene silencing of chitosan/siRNA complexes via the inclusion of a negatively charged poly (γ-glutamic acid). *Biomaterials* 2010; 31: 8780-8788.
107. Doye A, Mettouchi A, Bossis G, Clément R, Buisson-Touati C, Flatau G, Gagnoux L, Piechaczyk M, Boquet P, Lemichez E. CNF1 exploits the ubiquitin-proteasome machinery to restrict Rho GTPase activation for bacterial host cell invasion. *Cell* 2002; 111: 553-564.
108. Lai SK, Wang Y-Y, Hanes J. Mucus-penetrating nanoparticles for drug and gene delivery to mucosal tissues. *Advanced drug delivery reviews* 2009; 61: 158-171.
109. McGill SL, Smyth HD. Disruption of the mucus barrier by topically applied exogenous particles. *Molecular pharmaceutics* 2010; 7: 2280-2288.
110. Kanazawa T, Akiyama F, Kakizaki S, Takashima Y, Seta Y. Delivery of siRNA to the brain using a combination of nose-to-brain delivery and cell-penetrating peptide-modified nano-micelles. *Biomaterials* 2013; 34: 9220-9226.
111. Casettari L, Vllasaliu D, Mantovani G, Howdle SM, Stolnik S, Illum L. Effect of PEGylation on the toxicity and permeability enhancement of chitosan. *Biomacromolecules* 2010; 11: 2854-2865.
112. Wang YY, Lai SK, Suk JS, Pace A, Cone R, Hanes J. Addressing the PEG mucoadhesivity paradox to engineer nanoparticles that “slip” through the human mucus barrier. *Angewandte Chemie International Edition* 2008; 47: 9726-9729.

Supplementary information

Sequence type	Sequence 5’-3’
siDNA	S: GCT GAC CCT GAA GTT CAT CTG CAC C AS: GGT GCA GAT GAA CTT CAG GGT CAG CTT
Rac1 siRNA	S: CGC ACC UGU AAC UUA UCA GTT AS: CUG AUA AGU UAC AGG UGC GTT

Table S 1 Sequences of siDNA and Rac1 siRNA.

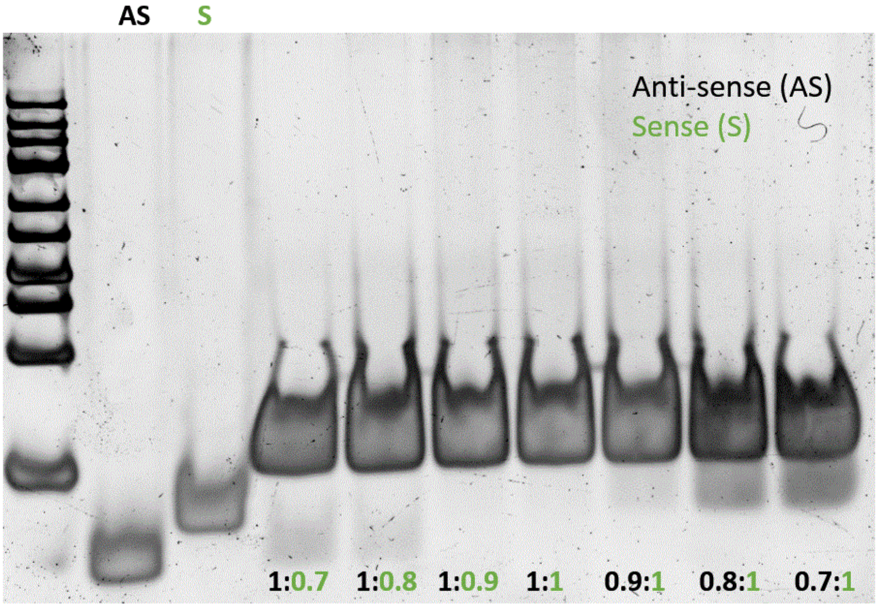

Figure S 1 siDNA sense (S) and anti-sense (AS) sequences were annealed at different AS/S molar ratios. DNA was stained with SYBRGold and gel visualized in a GelDoc XR imaging system. Results showed the conditions in which there are no free sequences and thus, that allows for a maximized annealing efficiency.

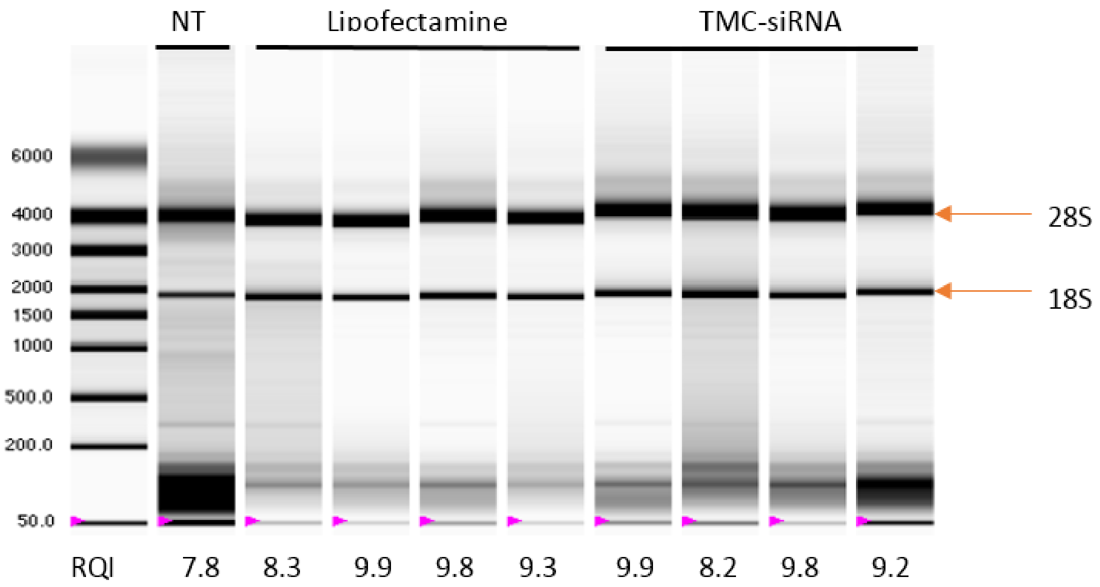

Figure S 2 Representative experion analysis of RNA samples from transfected cells showing high RNA recovery levels and good integrity indexes for all the samples. 18S and 28S rRNAs are indicated. RQI = RNA quality indicator, algorithm that allows the standardization and quantification of RNA integrity with 10 meaning fully intact RNA and 1 meaning fully degraded RNA. NT= non-transfected.

Gene	Genebank Acession no.	Primer sequence 5'-3'	Product Length (bp)	T_m (ºc)
RAS-related C3 botulinum substrate 1 (Rac1)	NM_009007.2	S: ATGCAGGCCATCAAGTGTG AS: TAGGAGAGGGGACGCAATCT	215	58.42 59.74
Cyclophilin A (CypA)	NM_008907.1	S: TGGTCAACCCCACCGTGTTC AS: TAGATGGACCTGCCGCCAGT	235	62.61 63.18
Hypoxanthine-guanine phosphoribosyltransferase (HPRT)	NM_013556.2	S: GTAATGATCAGTCAACGGGGGAC AS: CCAGCAAGCTTGCAACCTTAACCA	177	52.17 50.00
Glyceraldehyde 3-phosphate dehydrogenase (GAPDH)	NM_008084.3	S: GCCTTCCGTGTTCCTACC AS: AGATGGGAGTTGCTGTTG	182	57.39 54.46
Phosphoglycerate kinase 1 (PGK1)	NM_008828.2	S: GGGAAGCGGGTCGTGATGAG AS: TGGGTTGGCACAGGCATTCTC	288	62.91 63.22

Table S 2 Primer sequences used in qPCR. T_m=melting temperature. bp=base pairs

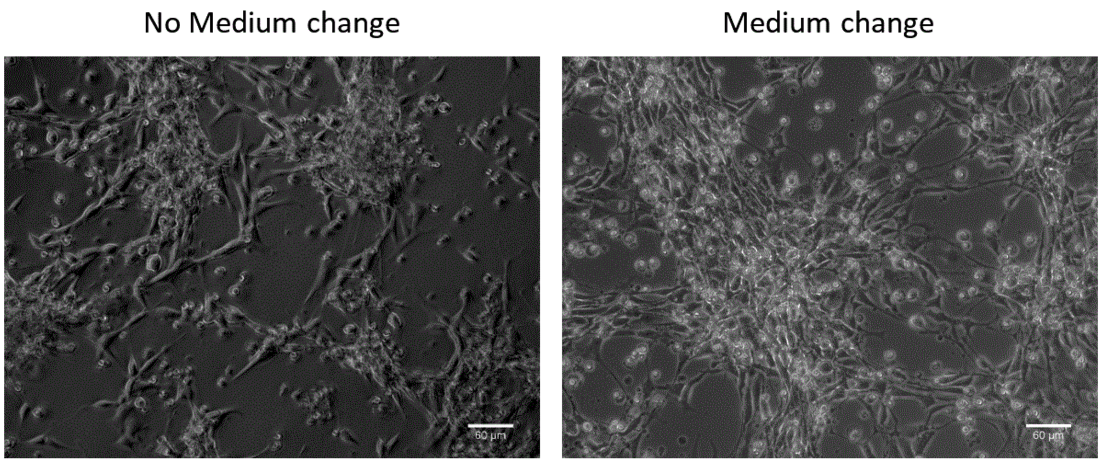
No Medium change
Medium change
60 µm
60 µm

Figure S 3 Phase contrast images of differentiated HT22 cells after four days of culture, with or without culture medium change.

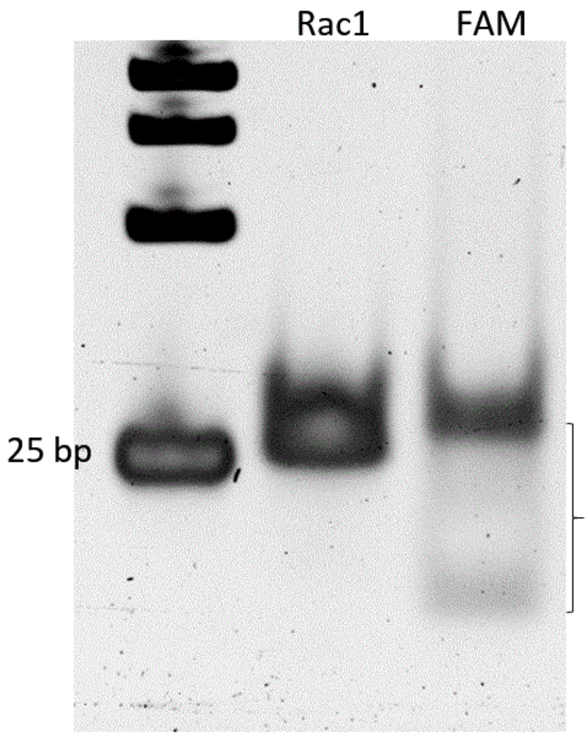
Rac1
FAM
25 bp

Figure S 4 siRNA electrophoresis. Brackets indicating sequences degradation. bp=base pairs

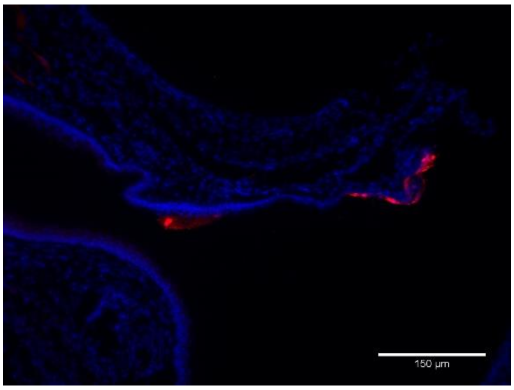

Figure S 5 Fluorescence microscopy image of the nasal mucosa of mice 4h after TMC_{ROX} complexes intranasal administration. Nuclei in blue (DAPI). TMC_{ROX} in red.